Computationally-aided design of aluminum alloys for high electrical conductivity power grids

Mehran Afshar

Computationally-aided design of aluminum alloys for high electrical conductivity power grids

Von der Fakultät für Georessourcen und Materialtechnik der
Rheinisch -Westfälischen Technischen Hochschule Aachen

zur Erlangung des akademischen Grades eines

Doktors der Ingenieurwissenschaften

genehmigte Dissertation

vorgelegt von

M.Sc. Mehran Afshar

aus Teheran, Iran

Berichter: PD Dr. rer. nat. Volker Mohles
Univ.-Prof. Dr. Sandra Korte-Kerzel
Prof. Dr.-Ing. Luis A. Barrales-Mora

Tag der mündlichen Prüfung: 14. Mai 2019

Acknowledgements

I would like to be grateful to Prof. Dr. Sandra Korte-Kerzel for giving me this opportunity to continue my education at the Institut für Metallkunde und Metallphysik of the RWTH-Aachen University.

Additionally, I would like to appreciate Dr. habil. Volker Mohles, the leader of the Simulation research group of the IMM, for his supports and encouragement during the project in the last three years. I am also thankful to Dr. Luis Antonio Barrales Mora for his fruitful discussions, helps and supports during the project, which made the target more accessible. I wish that I could express my gratitude to Dr. Mohles and Dr. Barrales for their support in words; however, the words could not always convey the true feelings.

It is also necessary to appreciate my colleagues, Sabine Lakrasche, Ziemons Arndt, Sergej Laiko, Fabrice Wagner, Simon Arnoldi, Christoffer Zehnder, Fengxin Mao, Haichun Jiang, Frederike Berrenberg, Marcel Schreiber, Dr. Stefanie Sandlöbes, Dr. Talal Al-Samman and Prof. Lazar Shvindlerman for making the working atmosphere more pleasant.

Finally, I would like to appreciate my sympathetic wife with her affectionate behavior which has filled my heart full of love and energy and also my lovely parents, which have grown me up and my siblings which help me to go forward.

I gratefully acknowledge Hydro Aluminium Rolled Products GmbH, for providing the materials and also the German Federal Ministry of Education and Research (BMBF) for the financial support of the project.

Contents

List of figures

List of tables

List of symbols

$\dot{\varepsilon}$	Strain rate / steady-state creep rate
σ	Stress
D_l	Lattice diffusion coefficient
D_b	Grain boundary diffusion coefficient
D_{pd}	Dislocation pipe diffusion coefficient
Ω	Vacancy volume
GS	Grain diameter
T	Temperature
k	Boltzmann's constant
A_{HD} , A_0	Constant
σ_{Th}	Threshold Stress (MPa)
N	Creep exponent
Q_0	Self-diffusion activation energy
B	Burgers vector
R	Universal gas constant
G	Shear modulus
P	Pressure
μ	Chemical potential
V	Volume
V^m	Molar volume
N	Number of individual phases
N_0	Nucleation sites
γ	Interfacial energy
ϕ	Heat flow
C_p	Specific heat capacity
H	Specific enthalpy
G_{sys}	Gibbs energy per unit volume of the system
Δg_p	Difference of Gibbs molar energy
σ_y	Yield stress
σ_0	Resistance to dislocation glide

1 Motivation

Copper alloys have an excellent electrical conductivity and, for this reason, have been used widely for many years in power grids. However, the price of the copper alloys has increased over time and a demand for new non-copper based conductive alloys has risen. The new alloys should satisfy the required mechanical and electrical properties. The new alloys must have high or comparable creep resistance, because the working temperature of the power grids remains normally at 140 °C but can increase for short periods to 200 °C. Additionally, new alloys should have high electrical conductivity and a reasonable price. Aluminum alloys are among the most promising candidates.

Aluminum has a high electrical conductivity (2.65×10^{-8} Ω.m), which satisfies this requirement for power grids. On the other hand, creep mechanisms in aluminum alloys are active at temperatures of more than approximately 0.5 of the homologous temperature, which is equal to 193.65 °C for pure aluminum, which is in the range of the working condition of the power grids. In order to use aluminum alloys in the power grids, it is necessary to develop alloys with an improved strength and creep resistance through different strengthening mechanisms. There are different strengthening mechanisms such as work hardening, solid solution hardening, precipitation hardening and dispersion hardening. Work hardening cannot in practice be considered, because the material recovers at operation temperatures. Solid solution hardening shows detrimental effects because high amount of substitutional or interstitial atoms decreases electrical conductivity. Therefore, solid solution hardening (dilute alloys), dispersion and precipitation hardening are the only possible useful mechanisms that can be applied. Nevertheless, the typical age hardening aluminum alloys are not useful in power grids, because the precipitates must be highly stable at the relatively high operation temperatures. To meet these requirements only a handful of elements can be considered. These elements are Cr, Cu, Fe, Mg, Mn, Ni, Si and Zr. Based on the mentioned elements, new aluminum alloys were produced and investigated in the frame of ALLEE project. The produced aluminum alloys were AA1070 (as a reference for the best electrical conductivity in aluminum alloys), AA6101A, AA8076A, AA3105, AA6101 + Zr, AA6101 + Ni and different alloys in AlNi, AlNiFe, AlZr and AlZrFe systems.

In order to achieve our goal and have a well-directed structure, the following questions are going to be examined in this dissertation in three chapters.

1.1 Scientific questions

1- How can precipitation be simulated and which classical nucleation and growth models can simulate the growth and dissolution kinetics of metastable phases? Can DSC curves be used to calibrate these models and is this kind of calibration preferable to microscopy imaging techniques? If so, is DSC sufficient? How far can this method substitute other experimentally expensive techniques?

In order to predict the correct sequence of metastable phases, a model is needed which should contain nucleation, growth and incubations models. The usual Zener growth law is not able to simulate the dissolution of the particles at lower temperatures compared to the phase diagram. In order to solve this problem, another growth law has to be implemented in the code. Furthermore, the model needs calibration. Calibration used to be based on TEM investigation which was time consuming. However, DSC curves could be useful tools to validate the precipitation sequence. DSC experiments show the precipitation sequence and the nucleation, growth and dissolution of the precipitates. Increasing the heating rate increases nucleation, growth and dissolution temperatures and shifts the DSC curves to higher temperatures.

A common method to calibrate this kind of models is TEM investigations, in which the phases, the size of the precipitates, are determined. But it is time consuming and costly. The DSC measurement can be a useful method to calibrate a model and reduce the TEM measurements.

2- Can a simulation model help to tune alloys, old or newly designed for preselected properties, in particular creep resistance and conductivity?

In order to obtain the maximum precipitation hardening, the precipitates should have a certain size (r_0), which corresponds to the particle radius at which the Orowan and the cutting stresses for dislocations to cut particles are equal.

Models for the prediction of the yield stress and the hardness were also implemented in the code to calculate the yield stress and consequently the hardness of the materials. Therefore, the maximum yields stress during a heat treatment can be calculated and the results are helpful to tune the strength of the simulated alloys. There are also functions to simulate the electrical conductivity of the alloys based on the chemical composition of the materials.

3- **Which creep mechanisms are active at the application temperature and under different stresses? How can we optimize the creep resistance of aluminum alloys without compromising the electrical conductivity?**

To address this question, the creep mechanisms which are active at the application temperature should be determined through creep tests at different temperatures and stresses. TEM investigations should prove if the defined creep mechanisms through the creep tests are valid. If dislocation glide is the dominant creep mechanism, solid solution hardening (dilute alloys), dispersion hardening and precipitation hardening could be helpful strengthening mechanisms to produce new aluminum alloys, which are creep resistant and have a comparable electrical conductivity with the copper alloys.

2 Literature review

2.1 Precipitation hardening in aluminum alloys

2.1.1 Precipitation hardening

One of the most important processes for strengthening materials is age hardening. Through age hardening the strength/density ratio increases, which is an important parameter in the aerospace industry. Age hardened aluminum alloys are also the base materials used in automotive applications. Precipitation hardening is the principle of age hardening, in which second phase particles precipitate from a supersaturated solid solution. Precipitates and matrix interface can be coherent, partially coherent or incoherent. The type of interface can determine decisively how a dislocation interacts with a precipitate (e.g. [1]–[5]).

If a quenched super saturated solid solution is tempered at low temperatures, metastable phases can appear. These particles usually have coherent or partially coherent phase boundaries. In such cases, dislocations commonly cut the particles (see Figure 2.1.a). This process will produce new interfaces, which increases the free energy of the crystal. This energy must be compensated by the applied stress causing the dislocation motion[1]. The strengthening contribution of the particles when cut depends on the particle radius and their volume fraction (Eq. 1) (e.g. [1]):

$$\Delta\tau_c = \frac{\tilde{\gamma}^{3/2}}{b}\sqrt{f}\frac{\sqrt{r}}{\sqrt{6E_v}} \qquad \text{Eq. 1}$$

where f is volume fraction, $\tilde{\gamma}$ is an effective interface energy, r is the particle radius and E_v is the energy of an edge dislocation. If the heat treatment is conducted for a long time, the metastable particles grow and transform into stable phases that form incoherent boundaries with the matrix. In this case, the dislocations can only bypass the particles (see Figure 2.1.b) [1]. The stress which is necessary for dislocations to bypass particles, can be calculated according to Orowan mechanism (Eq. 2) as [1]:

$$\tau_{OR} = \frac{Gb}{r}\sqrt{f} \qquad \text{Eq. 2}$$

Figure 2.2.a shows the theoretical dependence of strengthening on particle size. There is always an optimum radius (Eq. 3) which delivers the maximum strength [1].

$$r_c = \frac{Gb^2}{\bar{\gamma}}\sqrt[3]{3} \qquad \text{Eq. 3}$$

If the precipitates are smaller than r_c, dislocations pass them by cutting and if their radius is bigger than r_c, they will be by passed by the Orowan mechanism[1]. Figure 2.2.b shows the effect of particles' volume fraction on the Hardness [6].

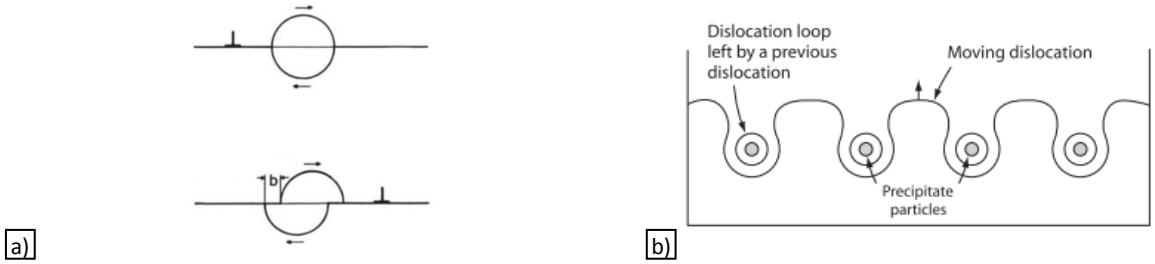

Figure 2.1. A dislocation-particle interaction (a) by the cutting mechanism (b) by Orowan's mechanism [1], [2].

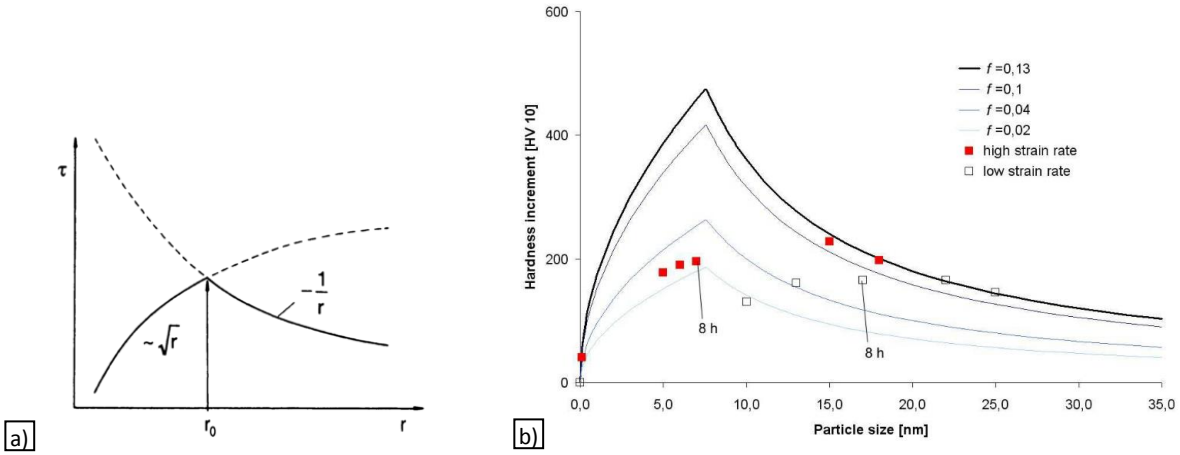

Figure 2.2. The dependence of strengthening on particle size. (a) Schematic from theories; (b) effect of particles' volume fraction on the Hardness [6].

2.1.1.1 2xxx, 6xxx and 7xxx series aluminum alloys

Typical examples of age hardenable aluminum alloys are the 2xxx series aluminum alloys containing Cu and Mg with copper as the major alloying element. Additionally, 6xxx series aluminum alloys containing Mg and Si have been considered as the most promising age-hardenable materials for automotive applications as well as the 7xxx series aluminum alloys containing Zn, Mg and Cu with zinc as the major alloying elements [1], [7]–[10].

The 2xxx series aluminum alloys become hardenable mainly by the addition of Cu [11]–[14]. The maximum solubility of Cu in Al is 5.56% at 548 °C and it decreases to less than 1% at room temperature. In order to observe the age hardening effect, the chemical composition of the

alloy must be in a composition range that at high temperatures allows all the elements to be in a solid solution whereas at lower temperatures the solid solution decomposes into two phases. Figure 2.3.a shows the Al-Cu phase diagram on the Al-rich side. If a sample with a composition close to the a-b-c line in Figure 2.3 is quenched after homogenization at 548 °C, it will result in a super saturated solid solution. Afterward, if the sample is heat treated at temperatures higher than room temperature but substantially lower than the solvus temperature, the hardness of the sample will increase due to the nucleation and growth of particles of a secondary phase (see Figure 2.3.b). The first hardening stage can be attributed to the GP zones formation. By increasing time or temperature, a second peak is observed. This is caused by the formation of θ' phase. If the heat treatment continues further, the precipitates grow further and the hardness decreases due to the Ostwald ripening [15]. The sequence of formation of precipitates in 2xxx series aluminum alloys was described by GPI+GPII zones → θ′ → θ (Al_2Cu) or GPII zones → S′′ → S′ → S1 and S2 (Al_2CuMg)[1], [16]. The formation of the S or θ phase depends on the chemical composition of the alloy. Artificial ageing can be done at the range of 130-170 °C for 2xxx series aluminum alloys [17]–[20].

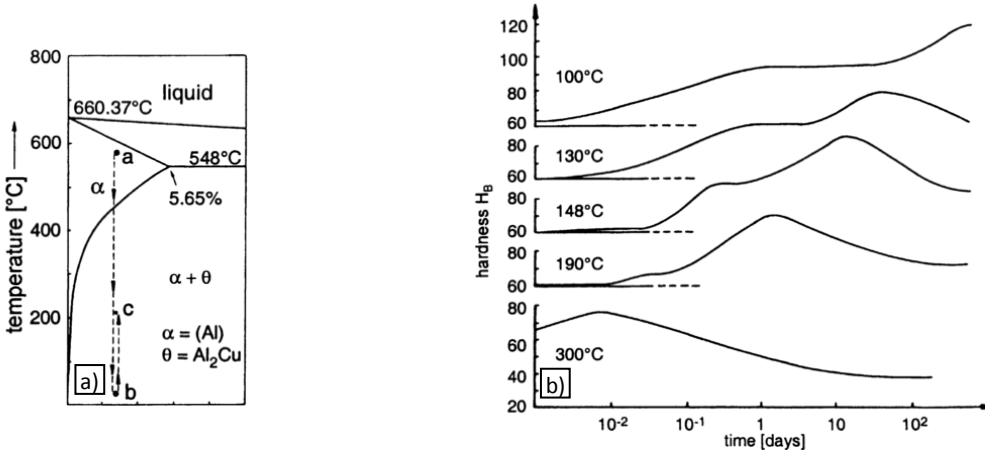

Figure 2.3. (a) The AI-Cu phase diagram o the AI-rich side, (b) age hardening curves of AI-4%Cu-l%Mg [1], [21].

The 6xxx series aluminum alloys have been also the subject of several studies in recent years. In particular, Al-Si-Mg alloys have displayed excellent mechanical properties owing to substantial age-hardening upon heat treatment [3], [22]–[28]. These alloys are used widely for automotive and aircraft applications. In commercial 6xxx series aluminum alloys, the amount of magnesium and silicon content are set in such a way that allows forming a quasi-

binary Al–Mg_2Si alloy (Mg:Si 1.73:1). It is also possible to permit an excess of silicon, which is needed to form Mg_2Si. To tailor the mechanical properties in these alloys, it is essential to know the exact precipitation sequence and their corresponding kinetics of precipitation and growth. In this regard, there have been experimental investigations that have showed that the precipitation hardening response is related to the Mg-Si phases [9], [29]–[31]. The sequence of precipitation formation from the solid solution condition in Al-Mg-Si alloys can be described as cluster → GP zones → β'' → β' → β (Mg_2Si), whereas the precipitation sequence of Al-Mg-Si alloys with a high silicon content is believed to be GP zones → small precipitates with an unknown structure → β'' → β' → Si → β (Mg_2Si) [32]–[38].

The metastable precipitates are in nano-scale, therefore TEM is used to characterize them. Figure 2.4 shows the bright field image of an AA6022 aluminum alloy, which is heat-treated to 260 and 300 °C at 10 °C/min after solutionizing and quenching [39]. TEM images have shown that at 260 °C the precipitates are needle-like, between 20-40 nm long and with a diameter between 2-5 nm. The overlap of diffraction patterns of the precipitates on the matrix diffraction pattern can be observed along [010]Al zone axis due to the needle-like morphology of the precipitates. The cross section of the precipitates of the quenched sample at 300 °C is rectangular. This shape has been attributed to the β' lath-like precipitates [28], [30], [39], [40].

In the as-cast condition, there are two types β precipitates. They are shown in Figure 2.5. One type is shown to precipitate on the boundaries of the primary solidified α-Al(Mn,Fe)Si particles. The mentioned precipitates are spherical and generally bigger than 2µm. The second ones are observed to appear in the matrix. These particles precipitate from the super saturated solid solution. These latter precipitates are plate-like or needle-like and usually smaller than 0.5 µm. It is also stressed that higher content of the Fe leads to a lower volume fraction of the Mg-Si phases. This is attributed to the absorption of the Si by α-Al(Mn,Fe)Si phase and consequently lower Si content available in the matrix for the formation of the particles Mg-Si particles [41].

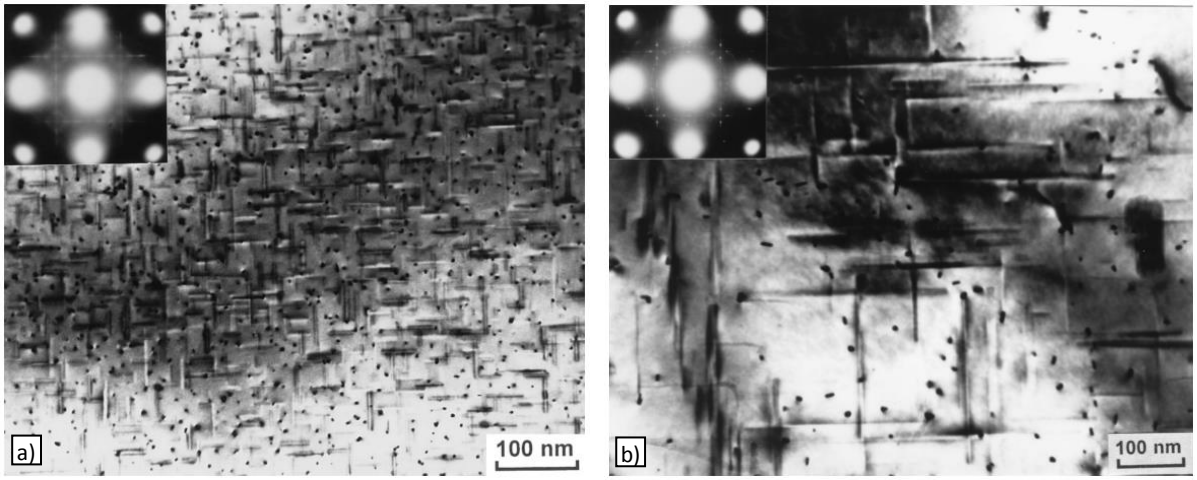

Figure 2.4. Bright-field TEM micrographs ([001]Al zone axis) of a AA6022 aluminum alloy heated to (a) 260 °C and (b) 300 °C at 10 °C/min immediately after solutionizing and quenching [39].

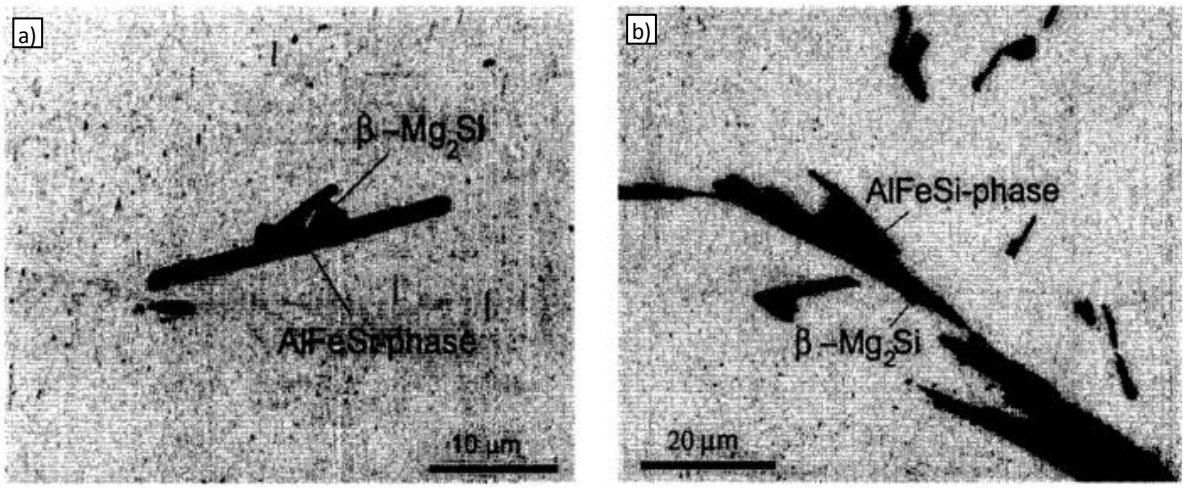

Figure 2.5. Optical micrographs of an Al-Mg-Si alloy [41].

In order to determine the precipitated phase in the matrix, a selected area electron diffraction (SAED) pattern of the precipitates must be compared with known structures. Figure 2.6 shows the predicted diffracted pattern of a [001] Al zone axis which contains needle-like precipitates along the [010] and [100] zone axis of matrix. This pattern should be compared with the experimental SAED patterns from the precipitates [30]. The structure of metastable and stable Mg-Si phases are discussed in [28], [42].

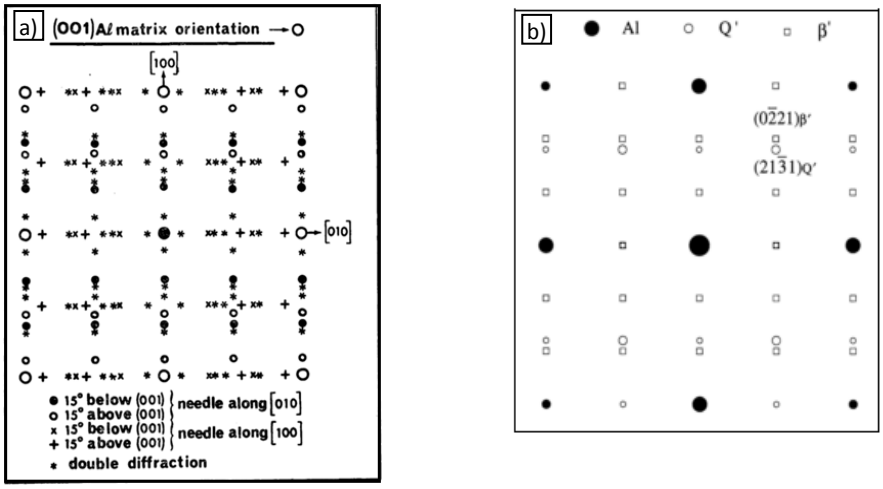

Figure 2.6. Predicted diffracted patterns of (a) a [001]Al zone axis which contains needle-like precipitates β'' along [010] and [100] zone axis of matrix [30] (b) β' and Q' with a same orientation relation[28].

The 7xxx series aluminum alloys deliver the highest precipitation hardening contribution among all aluminum alloys. 7xxx series aluminum alloys contain Zn and Mg. The sequence of precipitation formation from the solid solution in Al-Zn-Mg alloys is described as: solid solution → GP-zones → η' → η -$MgZn_2$ [43]–[47]. Studies have shown that the highest contribution of the particles on the strengthening of the 7xxx series aluminum alloys is observed after a single ageing at temperatures in the range 120–135 °C. At higher temperatures of 160-170 °C, the strength of the material decreases drastically due to the formation of η or η' phases [9].

The 3xxx series aluminum alloys have been used widely in packaging. The 3xxx series aluminum alloys are denoted as non-heat treatable alloys. The diffusion of Fe and Mn, which are the main alloying elements in the 3xxx series aluminum alloys, are rather low in the aluminum matrix. Therefore, the usual strengthening mechanism in these alloys is work hardening [48]–[50]. However recent reports have shown that a precipitation process occurs in an as-cast AA3004 alloy and improves the mechanical properties and electrical conductivity [51]–[57]. The partially coherent α-Al(Mn,Fe)Si dispersoids precipitated during heat treatment and simultaneously primary Al_6(Mn,Fe) particles dissolved [58]–[60]. Figure 2.7 shows a 3D representation of the diffraction pattern. It indicates the dissolution and precipitation of different phases during heating at 50°C/h up to 550°C for a 3003 aluminum alloy [59].

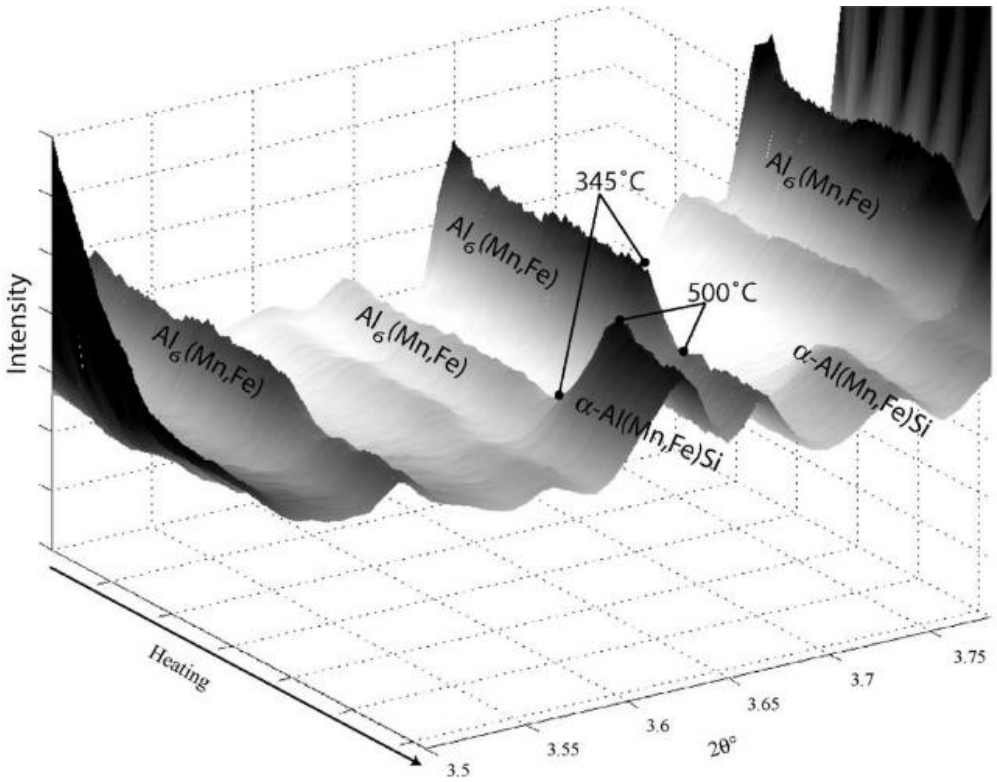

Figure 2.7. 3D representation of the diffraction pattern of a 3003 aluminum alloy during continuous heating at 50°C/h up to 550°C [59].

2.2 Differential scanning calorimetry

Owing to the difficulty of directly observing the precipitation sequence, differential scanning calorimetry has been used to determine the temperatures associated with precipitation and thus capture the precipitation behavior indirectly [28], [35], [39], [61]–[67]. The method was developed in 1962 by E. Watson [68]. In this method, a sample and a reference material are heated simultaneously. During the heating of the sample, different physical transformations can occur. These transformations release or absorb energy and thus influence the temperature. Simultaneously, the differences between the sample's temperature and the temperature of the reference material are recorded. The recorded data can be converted to energy changes, which occur in the samples during heating or cooling. During a DSC measurement, the temperature is increased with a constant rate with respect to the time. As long as no reaction happens in the sample, the temperature difference of the sample and the reference material is zero. If an endothermic transformation occurs, the sample absorbs energy and causes a delay in the temperature rise. When the transformation is completed,

the system goes back to a dynamic equilibrium condition, meaning that the sample temperature change approaches that of the reference material. If the transformation is exothermic, the sample temperature rises and for a while, the temperature of the sample is higher than the reference material [68]. The result of the DSC measurement is a curve of heat flow with respect to temperature. An advantage of DSC measurements is that the recorded curves shows clearly the precipitation and dissolution of precipitates [63], [69]. As an example, Figure 2.8 shows the DSC curve of an Al-Mg-Si alloy at different heating rates. The first exothermic peak A is attributed to the formation of solute atom clusters. Peak B shows the dissolution of them. Peak C is due to the β'' precipitates which are needle-like. The next peak D is interpreted as the growth process of β'' needles into β' rods. The reaction E is probably from the β-Mg_2Si precipitation. It is also known that the excess Si accelerates formation of cluster or β''. Figure 2.8 shows that increasing the heating rate shifts the peaks to higher temperatures [34], [36].

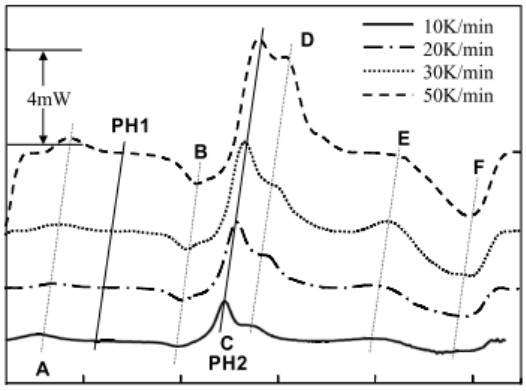

Figure 2.8. DSC curves of an Al-Mg-Si alloy at different heating rates [34].

Osten et al. [70] investigated the effect of different heating rates on the precipitation sequence and dissolution of particles in different 6xxx series aluminum alloys. They reported that the initial microstructure affected strongly the dissolution and precipitation behavior of the materials. Figure 2.9 shows the DSC curves of AA6005A and AA6016 with different heating rates for the same initial conditions. The peaks shifted to higher temperatures by increasing the heating rate. It has been claimed that the area under the peaks decreases by increasing the heating rates [70]. This is attributed to the suppression of the diffusion process. When the heating rate is higher, the precipitation sequence cannot be completed. Additionally, the

precipitation and dissolution processes are diffusion controlled processes and their dependency on heating rate is observable by following the evolution of peak *H* at different heating rates in Figure 2.9. When the heating rate is higher, there is not enough time for diffusion and the peaks are smaller and are shifted to higher temperatures. The different height of the peaks *c* and *d* is related to the overlap of exothermic and endothermic reactions, in which a faster dissolution kinetic and slower precipitation reaction are superimposed[67], [70]. The kinetic and precipitation sequence of the T6 (artificially aged conditions) and the T4 (naturally aged) conditions are similar. Specifically, there are no peaks *a* and c. This is because of precipitation of GP zones and β'', which formed previously during the T6 process. These particles are dissolved at T4. The further sequence correlates with the development of the T4 natural aged condition. In order to show the different initial conditions, different aluminum alloys were used. For a higher content of Mg and Si, formation of clusters (peak *a*) is observed in the EN-AW6016 specimens in T4 condition. This peak followed the endothermic peak *B*, which is attributed to the dissolution of the clusters. The peaks *c* and *d* were reported frequently as formation of β"and β' precipitates. Consequently, peaks *F* and *H* are endothermic reactions of the dissolution of these precipitates and *g* is the exothermic peak of β formation. According to the EN-AW6016 samples, by overlapping of the dissolution and precipitations, the peak formation of β was not observed.

This analysis shows that DSC is a powerful method to observe the precipitation kinetic in materials, however it is necessary to use alternative methods to determine the phases which are precipitated at certain temperatures.

2.3 Modelling of precipitation

Formation of new particles from a super saturated solid solution is termed precipitation and can be considered as a reaction in a closed region in space and described in a thermodynamic system. The free energy of the thermodynamic system, which is described by Gibbs free energy G, can be considered as the driving force of the phase transformation[71]:

$$G = U + PV - TS \qquad \text{Eq. 4}$$

where U internal energy, P and V are pressure and volume. T is temperature and S is entropy. The partial derivatives of the Gibbs free energy with respect to the states parameter are[71]:

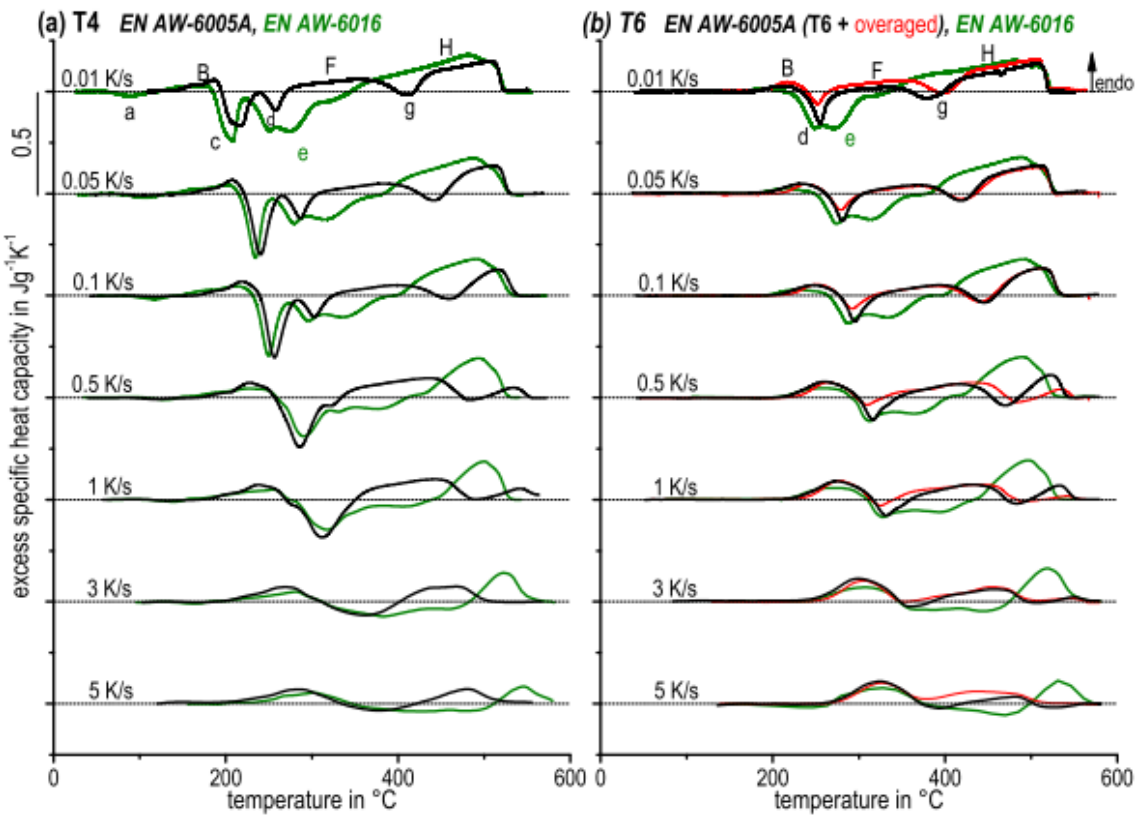

Figure 2.9. DSC curves of AA6005A and AA6016 with different heating rates for the initial conditions (a) T4. (b) T6 [70].

$$\left(\frac{\partial G}{\partial T}\right)_{P,N_i} = -S \qquad \text{Eq. 5}$$

$$\left(\frac{\partial G}{\partial P}\right)_{T,N_i} = V \qquad \text{Eq. 6}$$

$$\left(\frac{\partial G}{\partial N_i}\right)_{T,P,N_{j\neq i}} = \mu_i \qquad \text{Eq. 7}$$

Here μ_i is chemical potential of component i and N_i is the number of moles of component i. The precipitation process is considered in an isothermal and isobaric system. Therefore, the chemical potential in the Eq. 7 is more important for the precipitation process. The Gibbs energy of a system is described by the summation of the chemical potential of all the components[71].

$$G = \sum_i \mu_i N_i \qquad \text{Eq. 8}$$

Figure 2.10 shows a typical sketch of Gibbs energy vs composition. The driving force for the precipitation of the β phase (d^{β}_{chem}) from a super saturated solid solution is described by Eq. 9 [71]:

$$d^{\beta}_{chem} = -\sum_i X_i^{\beta}\left(\mu_i^{\beta} - \mu_i^{\alpha}\right) \quad \text{Eq. 9}$$

where X_i^{β} is molfe fraction of phase β.

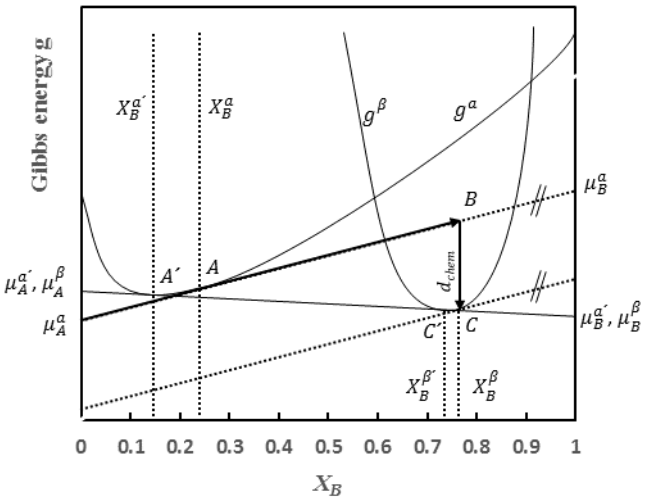

Figure 2.10. A typical Gibbs energy vs composition with an evaluation procedure for driving force calculation [71].

Beside the chemical driving force, the capillary force and the elastic misfit stress (ΔG^{el}_{vol}) reduce the driving force for precipitation. The capillary force stems from the pressure exerted by the curvature of the interface on its surface. The second back driving force is the volumetric lattice mismatch between matrix and precipitate that causes an elastic distortion and thus, an increase of the free energy in the system[71].

2.3.1 Nucleation of precipitates

In 1935 Becker and Döring [72], [73] introduced a kinetic equation for the nucleation of droplets from a super saturated vapor. This equation has been proven to be valid as long as the amount of the phases are not comparable to each other. It is necessary to know the total formation energy of a spherical nucleus to calculate the energy barrier at critical radius ΔG^*

$$\Delta G^*(r) = \Delta g_T \cdot \frac{4\pi}{3} r^3 + \gamma \cdot 4\pi r^2 \quad \text{Eq. 10}$$

where γ and Δg_T are the interfacial energy and chemical driving force per volume. r is the radius of the particle. The total formation energy has a maximum value, which can be calculated according to the Eq. 12. The critical radius is the radius of nucleus at the maximum value which can be calculated using Eq. 10.

$$r^* = \frac{2.\gamma}{\frac{d^{\beta}_{chem}}{v^{\alpha}} - \Delta G^{el}_{vol}} \quad \text{Eq. 11}$$

$$\Delta G^* = \frac{16\pi.\gamma^3}{3.\left(-\frac{d^{\beta}_{chem}}{v^{\alpha}} + \Delta G^{el}_{vol}\right)^2} \quad \text{Eq. 12}$$

Here $v^{\alpha}$and ΔG^{el}_{vol} are the molar volume of a phase and the elastic energy per volume, respectively. The probability of a thermal fluctuation to be sufficient for nucleation is calculated by an Arrhenius term, hence the nucleation rate (J) can be written as:

$$J = \dot{N} \quad \exp\left(-\frac{\Delta G^*}{K_B T}\right) \quad \text{Eq. 13}$$

where $\dot{N}$ describes the density and frequency of nucleation attempts, which will be discussed in detail for the ClaNG model [71].

2.3.2 Growth and coarsening of precipitates

2.3.2.1 Zener growth model

The first theory of coarsening was proposed by Lifshitz and Slyozov [74]. Almost simultaneously, Wagner described the coarsening with another model [15]. The Lifshitz model was based on Zener's growth law. Zener's growth law is valid for spherical precipitates in a binary alloy and is described by [75], [76]:

$$\frac{dr}{dt} = \frac{D_i}{r}\frac{C_i^{\alpha} - C_i^{\alpha/\beta}(r)}{C_i^{\beta} - C_i^{\alpha/\beta}(r)} \quad \text{Eq. 14}$$

Here D_i is diffusion coefficient of element i in matrix. $C_i^{\beta}(r)$ and $C_i^{\alpha}(r)$ are the concentration of element i in the particle and in the matrix. $C_i^{\alpha/\beta}(r)$ is the concentration of element i at the particle interface in the matrix and can be calculated by the Gibbs-Thomson equation. The Gibbs-Thomson equation describes the effect of the curvature at the interface. According to Zener's law, the equilibrium concentration is only valid for a planar interface. The Gibbs-Thomson equation can be described by [75]–[78]:

$$C_i^{\alpha/\beta}(r) = C_i^{\alpha}(r).exp\left(\frac{2\gamma.V^m}{RT.r}\right) \quad \text{Eq. 15}$$

2.3.2.2 SFFK growth model

In 2004, Svoboda, Fischer, Fratzl and Kozeschnik developed a new growth model based on the mean chemical composition of the matrix. This model is valid for all stages of the evolution of the particles in a multi component system. It applies the extremum principle on the Gibbs function and has proven to be in good agreement with other established simulation techniques [79], [80]. Eq. 16 gives the growth rate of the precipitates in the SFFK model.

$$\dot{r} = \frac{\Delta g_T - (\frac{2\gamma}{r})}{RTr}\left[\sum_{i=1}^{n}\frac{\left(C_i^{\beta}-C_i^{\alpha}\right)^2}{C_i^{\alpha}D_i}\right]^{-1} \quad \text{Eq. 16}$$

2.3.3 Data representation

The first implemented nucleation and growth model was reported by Langer and Schwartz. They considered the processes of nucleation, growth and coarsening to proceed simultaneously. Their model describes droplet formation and growth in near critical fluids [81]. The model delivers a time evolution of droplet density and mean radius. Later, the Langer and Schwartz model was improved by Kampmann and Wagner [82] using a model for a supersaturated solid solution. In the mentioned models, a single radius was used instead of a precipitation size distribution. Later on, Wagner and Kampmann introduced a size distribution to their model. The model can predict the evolution of the precipitation size distribution [83]. The evolution of the precipitation size distribution can be implemented with different approaches. For instance, the mean radius approach, Lagrange-like approach and Euler-like approach are three methods for the implementation of the radius of the precipitates in the model. In simple cases, they deliver the same results but in more complex situations multi-class approaches are necessary [84]. In the following two multi-class approaches will be explained.

2.3.3.1 Euler-like approach

In this method, the precipitation size distribution is discretized in several size classes, and there is a flux of the particles occurring at the boundaries of the fixed classes as particles change their size. This is the method which Kampmann and Wagner used. Later on, Myhr et al. proposed to keep the volume constant in the growth stage [85]. In this method, the time increments must be calculated in a way that the highest change in a precipitation radius is

equal to half of the class width. A new population of a class is calculated from the number density and growth rate of the neighbor classes. The shifted amount of precipitates at the boundaries is added to the neighboring classes. Figure 2.11 shows the growth of the particles in the Euler-like approach. The flux between neighbor classes is calculated at each time step [84].

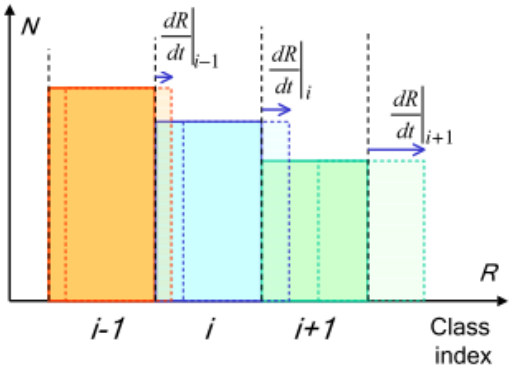

Figure 2.11. The growth of the particles in the Euler-like approach[84].

2.3.3.2 Lagrange-like approach

Maugis et al. proposed the Lagrange-like approach [86]. In this approach, the population of the classes is unaffected by growth; only nucleation and dissolution affect the populations. Growth is considered by altering the size corresponding to each class. As usual, too short time steps lead to slow simulations, and too large time steps lead to numerical instabilities. Figure 2.12 shows the nucleation and growth steps within a Lagrange-like approach [84].

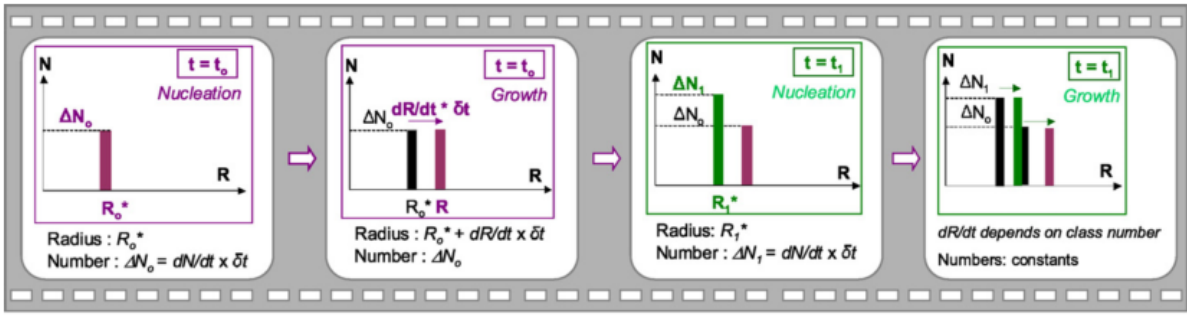

Figure 2.12. Nucleation and growth steps within a Lagrange-like approach [84].

2.3.4 DSC modeling

DSC measurements are an excellent tool to validate simulation models. Understanding the precipitation kinetics during the isothermal and non-isothermal heat treatment is essential to predict microstructure evolution and tailor the alloy to specific applications. For this purpose, in recent years, the simulation of isothermal heat treatments has been investigated widely [75], [85], [87], [88]. However, simulations of non-isothermal heat treatments, which are more relevant for technical applications, have been less frequent, in particular, in conjunction with a comprehensive validation. This last point is very relevant because in most cases the validation of the models have relied on observations with poor statistics such as particle size or volume fraction, which are performed by TEM microscopy, owing to the very small size of the particles[88]. Evidently, dissolution and precipitation of phases are difficult to characterize accurately by this method. An alternative to this method is the use of DSC measurements that can capture such events depending on the type of the reaction. In fact, DSC curves have been frequently utilized to characterize phase transformations, and in the specific case of Al alloys, these curves have been even recently simulated. For instance, Khan et al. introduced a first model for the simulation of DSC curves [89], [90] that was used by Falahati et al. [91]–[93] to simulate DSC curves in two aluminum alloys, 6xxx and 2xxx. Khan et al. defined the heat flow ϕ as:

$$\phi = \left(c_p^{sys} - c_p^{Al}\right) \times \frac{\Delta T}{\Delta t} = \frac{d(h^{sys} - h^{Al})}{dT} \times \frac{\Delta T}{\Delta t} \qquad \text{Eq. 17}$$

where c_p^{sys} and c_p^{Al} are the alloy and pure reference aluminum specific heat capacities, respectively; h^{sys} and h^{Al} are the alloy and pure Al specific enthalpies, respectively and ΔT/Δt is the heating rate. It is noted that in this model the effect of interfacial energy on the heat flow had not been considered.

Hersent et al. calculated the released and/or absorbed energy by using the classical Gibbs model [94]:

$$G_{sys}^{w} = \frac{1}{\rho}\left(\frac{g_{ss}^{m}}{V_{ss}^{m}} + \frac{\Delta g_p^m}{V_p^m}.f_v + \gamma.\frac{A}{V_{sys}}\right) \qquad \text{Eq. 18}$$

where G_{sys}^{w} is the total Gibbs energy per unit volume of the system, g_{ss}^{m} is the Gibbs molar enthalpy, Δg_p^m is the difference of the Gibbs molar energy between the precipitates and the solid solution, and V_{ss}^{m} and V_p^m are the molar volumes of the solid solution and the

precipitates, respectively. f_v is the volume fraction of the precipitates and A is the total interface area developed by the precipitates. These models or slight variations of them have been used to predict DSC curves. For instance, Starink et al. [89], [95] simulated the DSC curves of a 2024-T351 Al–Cu–Mg alloy using basically Khan's model (Eq. 1). They studied also the effect of the heating rate, which shifts the peaks, in a 2024-T351 alloy. In their approach, they implemented a time delay which depends on the interfacial energy, which in turn varies with the temperature [89]. These models have simulated the DSC curves with good accuracy. However, it must be stressed that some improvements can still be done by considering the effect on the energy of nucleation at preexisting lattice defects and explicit incubation time models. In the present study, a new model to describe endothermic und exothermic reactions during heat treatment of Al-Mg-Si alloys was developed and DSC curves used for calibration.

2.4 Creep mechanisms in aluminum alloys

High creep resistance is important for the conductor metals in power grids, because of the high working temperatures and stresses, which leads to activation of the creep mechanisms. Creep is a deformation mechanism which occurs in metals at high temperatures under a constant load or stress[1], [96]. Creep is a thermally activated process. According to established understanding, it needs a high vacancy concentration and thermal movement of atoms. Figure 2.13.a shows a typical creep curve, which shows the strain with respect to time and Figure 2.13.b shows the strain rate as a function of time. Increasing the stress at a constant temperature or increasing the temperature at a constant stress decreases the steady-state creep region [1].

The creep deformation is divided into three areas:

1. Primary creep: The strain increases with decreasing strain rate
2. Secondary creep: The strain increases linearly with a constant strain rate
3. Tertiary creep: The strain increases exponentially with increasing strain rate until fracture

The secondary stage of creep (steady-state creep) is the most important stage. It depends on temperature and the applied stress[96]. Steady-state creep refers to the region in the creep curves in which essentially, the substructure is quasi-static as dislocation multiplication and dynamic recovery are in balance. Whereas, the substructure formation depends on the

formation of a dislocation network. The secondary creep refers to the same region in the curve and is a region between tertiary and primary creep [97]. If a second and tertiary creep stage is not clearly observed, the minimum creep rate is used instead. The steady-state creep rate $\dot{\epsilon}_s$ can be described as a function of stress σ (known as "power-Law") and temperature T:

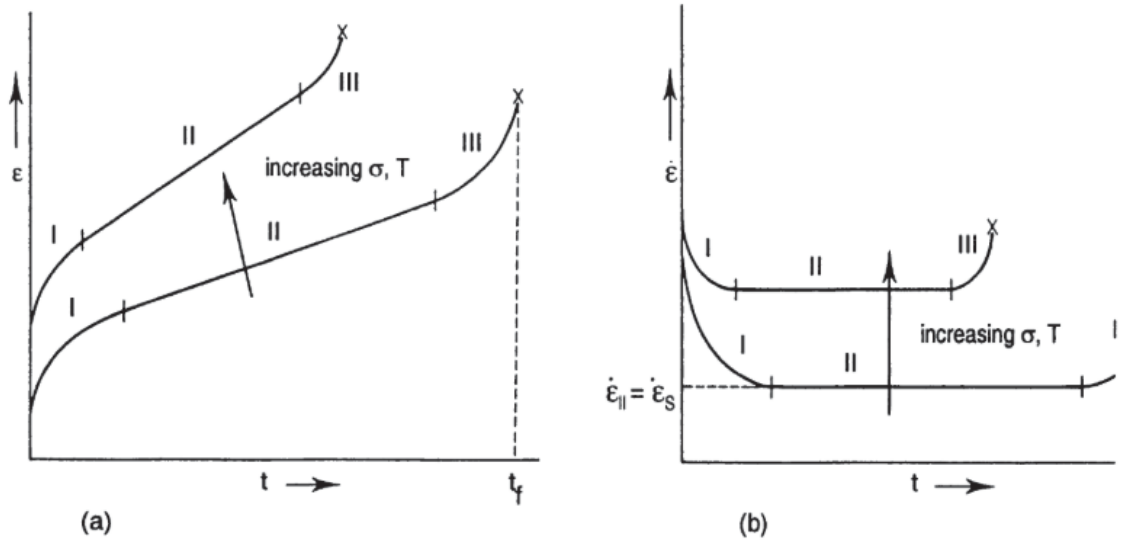

Figure 2.13. (a) A typical creep curve: strain as a function of time. (b) schematic curve of strain rate as a function of time [1].

$$\dot{\epsilon_S} = A\,\sigma^n \exp\left(-\frac{Q}{kT}\right) \qquad \text{Eq. 19}$$

where A is material and Temperature dependent [1]. The n-value is the creep stress exponent, Q is the activation energy and K is the Boltzmann constant.

There are different mechanisms which may contribute to creep. A common classification is dividing the creep mechanisms into: Dislocation creep, Grain boundary sliding and Diffusion flow caused by vacancies[98].

2.4.1 Dislocation creep

Dislocation motion is separated to two different types: slip and climb. Slip means dislocation motion in their slip planes. Whereas in climb, the motion is normal to the slip plane. If the stress is above the yield stress (on the order of a tenth of the theoretical shear strength (G/10), dislocation glide is the active deformation mechanism. If the stress is lower, as is usually the case in creep, continued slip of dislocations is only possible in combination with climb of the dislocations. In any case, whether the slip is accompanied with climb or not, dislocation

multiplication takes place with increasing strain. This leads to an increased critical stress, i.e. work hardening. In a creep experiment, the external stress is kept constant. This means that the creep rate decreases with increasing strain. However, there are also recovery processes, i.e. a reduction of dislocation density. When the dislocation multiplication and the recovery processes reach a balance, a quasi-steady state condition is reached. This is one possible explanation of the secondary creep stage.

Recovery is governed by the slip and climb of the dislocations, which also depends on the vacancies diffusion. It is common to consider the same activation energies for self-diffusion and for creep [98].

2.4.2 Grain boundary sliding

Grain boundary sliding (GBS) is known as a process in which the grains slide along their common boundaries (see Figure 2.14) [99]–[101]. Surface marker lines were used by Moore et al [102], [103] to observe the developed step at the intersection of the line with the grain boundaries. GBS was observed in different materials [104]–[106]. Grain boundary sliding is divided into Rachinger sliding [107] and Lifshitz [74] sliding. In Rachinger sliding, the grains keep their original shape, but they are displaced with respect to each other. This occurs under creep condition in polycrystalline samples when the number of grains increases along the tensile direction within the gauge length. The second one occurs in Nabarro-Herring and Coble diffusion creep and develops an offset between the markers as a direct consequence of the stress-directed diffusion of vacancies [108]. GBS may be responsible for 10—65% of the total creep strain. The contribution of the GBS to the creep strain increases with increasing the temperature and decreasing grain diameter[101]. The latter means that in order to minimize grain boundary sliding, the grains should be large. Unfortunately, this also means that any strengthening effect related to grain boundaries is not a good option to minimize creep. For instance, the Hall Petch stress increases the strength of the material at low grain diameters [109], [110], but at the same time low grain diameters promote higher creep rates due to grain boundary sliding. Additionally, grain boundaries are sources of vacancy formation, such that a higher amount of grain boundaries leads to higher vacancies presence, which will increase the dislocation climb[98]. Eq. 20 [111]–[113] and Eq. 21 [114] are models to calculate the steady-state creep rate in GBS.

$$\dot{\varepsilon}_{(d_g<subgrains\ size)} = A'\left(b/d_g\right)^2(\sigma/G)^2\ (D_{gb}\mathrm{Gb}\ /kT) \qquad \text{Eq. 20}$$

$$\dot{\varepsilon}_{(d_g > subgrains\ size)} = A' \left(b/d_g\right)^1 (\sigma/G)^3 \left(D_{gb}\mathrm{Gb}\ /kT\right) \qquad \text{Eq. 21}$$

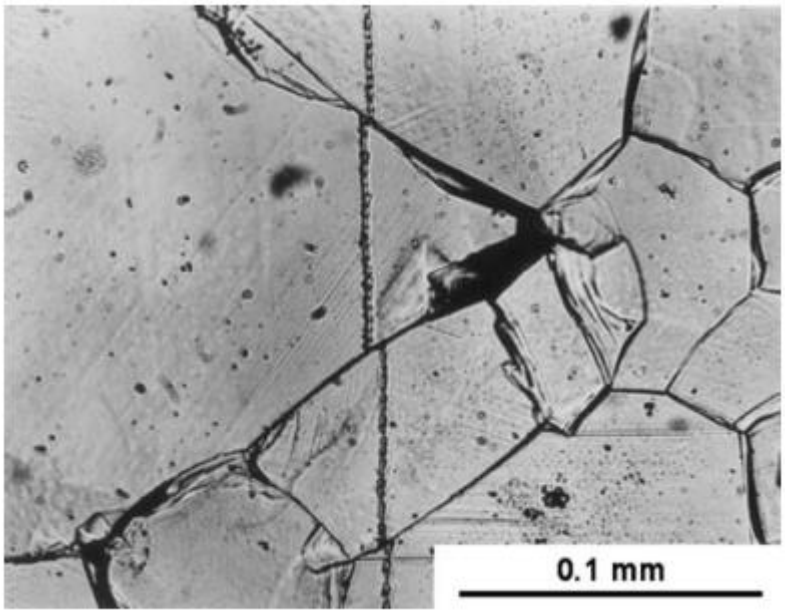

Figure 2.14. The occurrence of GBS revealed by the boundary offsets in a transverse marker line for an Mg-0.78%Al alloy tested under creep condition at 200 °C. The tensile axis is horizontal [101].

2.4.3 Diffusion flow caused by vacancies:

The diffusion creep mechanisms can be divided in three regimes, which are characterized by their stress exponents (see Figure 2.15). One for low stress exponent (n = 1-2), one for intermediate stress exponent (n = 4-5/3-6) and one for high stress exponent.

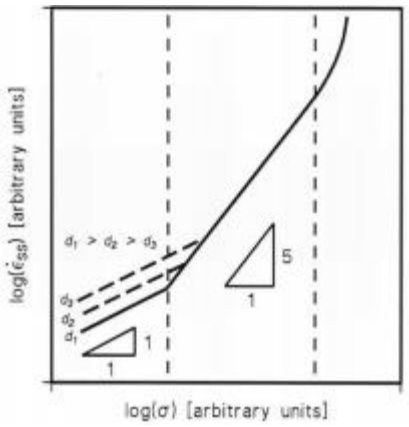

Figure 2.15. Creep regimes in dependence on stress. [96]

2.4.3.1 Nabarro-Herring creep

Nabarro reported that in polycrystalline materials, self-diffusion within the grains causes yielding. Nabarro claimed that the effective viscosity is proportional to the square of the grain diameter (d_g). Figure 2.16 shows the self-diffusion path of the elements in this creep mechanism. This phenomenon leads to creep at very high temperatures and very low stresses. Afterward Herring has explained that the presence of a pressure gradient leads to a diffusion flux of atoms in a direction which will relieve the inequality of pressure. This pressure gradient is energetically advantageous to move the lattice defects. In absence of a pressure gradient, diffusion flux of atoms is proportional to the gradient of the concentration of these lattice defects. Herring has proposed a model to calculate the steady-state creep rate Eq. 22 [115].

$$\dot{\varepsilon} = 10\ \sigma\ D_l \Omega\ /\left(d_g\right)^2\ kT \qquad \text{Eq. 22}$$

where Ω is the atomic volume and $D_l$is lattice diffusion coefficient.

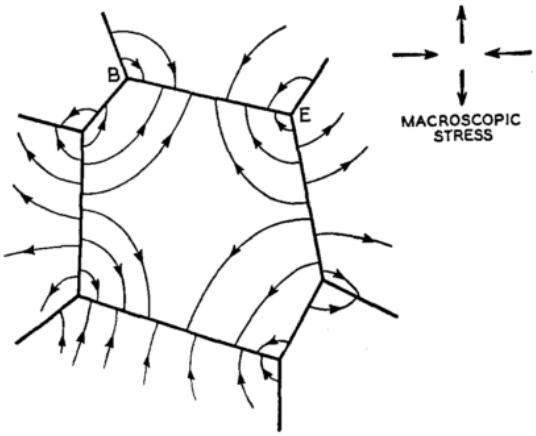

Figure 2.16. The self-diffusion within grains which causes creep in polycrystalline materials [115].

2.4.3.2 Coble creep

In 1963 Coble has developed a model for grain boundary diffusion controlled creep in polycrystalline materials. Coble found that the diffusion coefficients calculated via the Nabarro-Herring model from experimental creep rates were much larger than the self-diffusion coefficients. He explained the discrepancy by the diffusion through the grain boundaries [116]. He found that the stress exponent for both the lattice and grain boundary diffusion is the same. Thus, the only method to distinguish between the models is the grain

diameter dependency. Coble proposed that the exponent p in $\sigma/(d_g)^p$ is equal to 2 in the lattice diffusion model, and equal to 3 for boundary diffusion (see Eq. 23).

$$\dot{\varepsilon} = 148\,\sigma\,(D_{gb}\mathrm{W})\,\Omega\ /(d_g)^3\,kT \qquad \text{Eq. 23}$$

Here W is the effective boundary width and D_{gb} is the boundary diffusion coefficient.

2.4.3.3 Harper-Dorn creep

The Harper-Dorn creep mechanism is active at extremely high temperatures and at very low stresses, which explains the dislocation-climb theory. The Harper-Dorn mechanism is dominant in stress range up to 2.0 MPa [117]. Figure 2.17 shows the Harper-Dorn regime and Nabarro-Herring for different grain diameters for a pure Al [118]. The activation energy at high temperatures is equal to the activation energy for the self-diffusion mechanism, which is also the same as for the Nabarro-Herring creep mechanism, but the subgrain boundary formation shows that dislocation climb does occur. At high temperatures, the dislocations, which are piled up at the barrier, can escape the traps by climb. The observed steady-state creep is about 1400 times more than the Nabarro-Herring creep mechanism[117]. Yavari et al. [118] proposed the steady-state creep rate:

$$\dot{\varepsilon} = A_{HD}\,(\sigma/G)^1\,(D_l\mathrm{Gb}\,/kT) \qquad \text{Eq. 24}$$

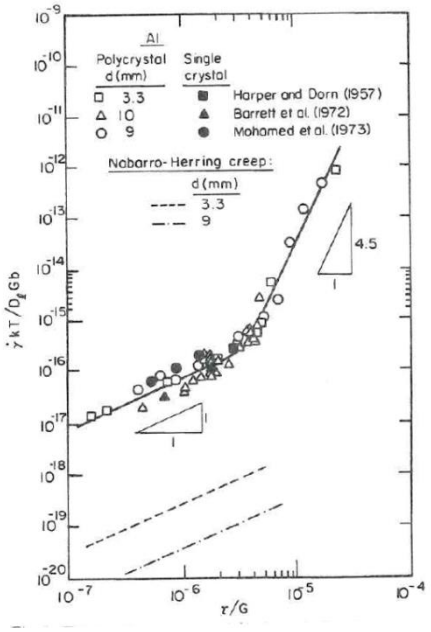

Figure 2.17. The temperature compensated shear strain rate vs. normalized shear stress (τ/G) for pure Al [118].

2.4.4 Low-temperature creep

In 2013, Matsunaga et al. reported that at low temperatures (Less than 0.4 melting temperature) a new creep mechanism can be active. This new creep mechanism was added to the deformation mechanism maps. Figure 2.18 shows the new deformation mechanism map[119]. The grain diameter exponent (p value) is equal to zero, which means that the new creep mechanism is independent of the grain diameter. The creep exponent is 4 and increases to 6 when the temperature increases and the activation energy is 30 kJ/mole. 30 kJ/mole is less than the self-diffusion activation energy and implies that the self-diffusion processes are not dominant [119]. The rate controlling process is dislocation annihilation by cross slip at cell walls (see Figure 2.19). Table 2.1 shows the exponents n and p and the activation energy for different regimes [119].

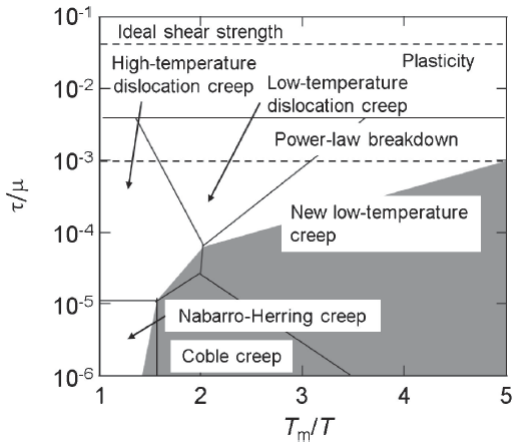

Figure 2.18. The re-drawn maps for 5N Al with d = 140 µm [119].

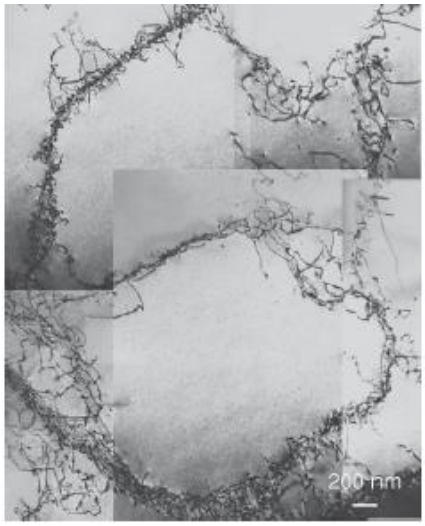

Figure 2.19. TEM images of cell walls taken after 8.6 × 10^5s creep under 30MPa at 300K for 5N Al [119].

Table 2.1. Creep parameters n, p and Q for different creep regimes [119].

Creep region	*n*	*p*	*Q*
New low-temperature creep	4	0	30 kJ/mol
Low-temperature dislocation creep	6	0	82 kJ/mol
High-temperature dislocation creep	4	0	142 kJ/mol
Coble creep	2	3	84 kJ/mol
N–H creep	1	2	142 kJ/mol

2.4.5 Methods to improve creep resistance

Dislocation motion and diffusion are two main creep mechanisms that control the creep rate. Retarding the dislocation motion and diffusion are important to improve the creep resistance of alloys.

In order to reduce the dislocation motion under a certain stress, the metals with higher melting temperature are preferred. Additionally, introducing obstacles which increase the needed stress to move the dislocations through a lattice by the Orowan mechanism, is useful. Additionally, metals with bigger grain diameters contain less grain boundaries, which are considered as fast diffusion paths. A larger grain diameter reduces the amount of grain boundaries and is used to reduce the fast diffusion paths. Therefore, Coble creep takes place through longer diffusion paths, and the steady-state creep rate decreases. In addition, the impact of grain boundary sliding decreases. Additionally, it is important to note that a grain refinement as a strengthening mechanism for low temperature applications of a material will have negative effects on the creep resistance [120]. On the other hand, solid solution hardening and precipitation hardening are the most useful methods. Solute atoms reduce the electrical conductivity, therefore solid solution hardening is not a useful method for power grids. In the following, the effect of precipitation of the secondary phases on the strain rate and creep behavior will be explained in detail.

Precipitates restrict the mobility of dislocations and reduce the steady-state creep rate which is controlled by dislocation climb. Precipitates can also reduce the grain boundary sliding, if the precipitations are placed at grain boundaries. An optimum increase of creep resistance can be achieved by forming equally dispersed fine particles which are also thermally stable. The precipitations should not dissolve or coarsen during the application at high temperatures. Coarsening causes a decrease of strength, because the dislocations need lower stress to bypass the precipitates [120], [121], and dissolution would remove their strength contribution entirely. This holds for normal deformation (including work hardening) as well as creep. Therefore, a small diffusion coefficient of particle elements is ideal to prevent any change of particles. A low solid solubility is preferable because of low resistivity, and because all material tends to be consumed by the particles. Both properties are important factors for the precipitations to remain stable at high temperature applications and keep a constant effectiveness in hindering the dislocations from moving through the crystal [121].

Figure 2.20 shows the decrease of the Orowan stress with increasing precipitation radius for different precipitate volume fractions. Unlike the nickel base super-alloys for example, the dislocations in aluminum are also able to bypass precipitations by climbing out of their glide plane, which reduces the creep resistance compared to nickel base alloys.

An elongation of the dislocation length results during the bypass of the precipitations and leads to an increase of the needed stress to keep the dislocation movement, which results in the occurrence of a threshold stress, called the Orowan stress. As long as the precipitations are not sheared, a smaller size of the precipitates is accompanied with a higher creep resistance and also a higher threshold stress. Therefore, it can be assumed that smaller particles are always preferred. In the climbing mechanism, which is different from Orowan by-passing, the elongation during this climb leads to a threshold stress, which is also proportional to the Orowan stress [121]–[124].

If the precipitations are coherent, elastic interactions can also increase the threshold stress. The elastic interaction energy depends on the size of the particles and their shear modulus. If the shear modulus is higher, the interaction energy is higher [125]. In addition, the surface energy between the precipitation and the matrix decreases with higher coherency. Therefore, the driving force for precipitation coarsening is reduced when the precipitations are coherent and the stability of the precipitations at higher temperatures is increased. This is why coherent precipitations are preferred over incoherent particles [121]. However, they should be large enough in order not to be sheared by dislocations.

If too many precipitates are formed, they can also act as crack nucleation points, when the precipitates appear as a chain through the crystal. The large interface area will act as a predetermined breaking point [120].

In the 2xxx series aluminum alloys, the maximum allowable working temperature is less than 120 °C, above this temperature coarsening occurs. In order to improve the creep resistance of 2xxx series aluminum alloys, new elements were added to form dispersoids [9]. One of the aluminum alloys which poses a creep resistance up to 50 000 hours at moderate temperatures is AA2618 (RR85). Even in this case, the maximum temperature does not exceed 120 °C [9].

Figure 2.21 shows the creep rate dependence on the applied stress for a particle reinforced alloy. At low stress regime, the creep exponent is 1, which implies that the precipitates have

stopped the dislocation motion, therefore either the diffusion creep mechanism is the predominant creep mechanism or the dislocations pass the particles via climb [96]. The active creep mechanism in the low stress regime could be either Coble, Harper-Dorn or Nabarro-Herring creep. At higher stresses the precipitates can be bypassed. The minimum necessary stress to observe dislocation creep is the threshold stress σ_{Th}. The most widely used approach to describe the effect of stable precipitates on the steady-state creep rate is:

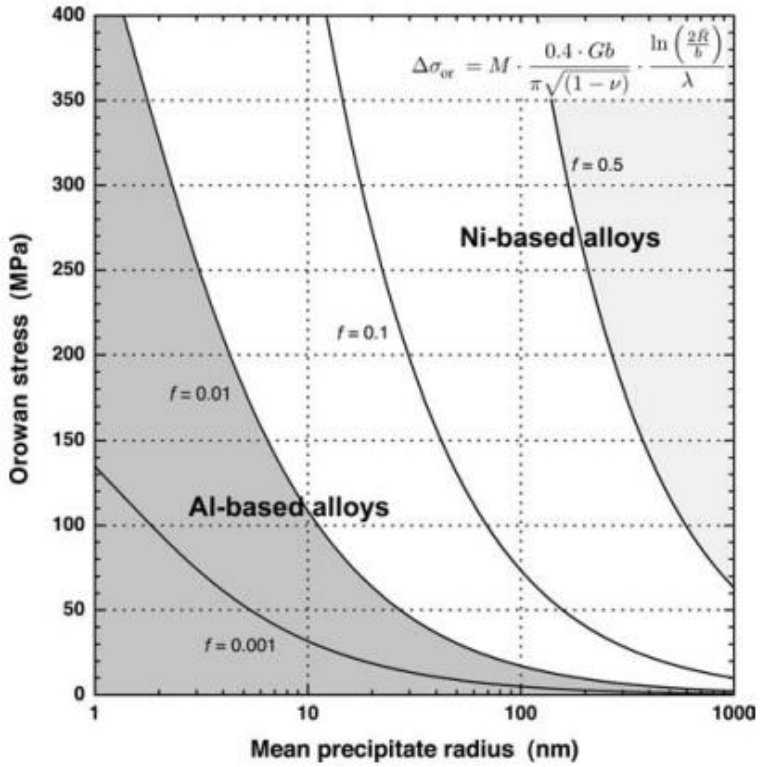

Figure 2.20. The Orowan stress as a function of mean precipitate radius [121].

$$\dot{\varepsilon} = A_0\ ((\sigma - \sigma_{Th})/G)^n\ exp(-Q_0\ /kT) \qquad \text{Eq. 25}$$

Where $\sigma - \sigma_{Th}$ is the effective stress [96], [126]–[129] ,Q is the activation energy, T is the absolute temperature, and K is Boltzmann constant.

Figure 2.22 shows the effect of precipitation hardening and solid solution hardening on shifting the creep rate vs. stress curves to higher stresses. It should be mentioned that solid solution hardening shifts the curve roughly uniformly. The Al-Mg alloy is an example of solid solution hardening. In the Al-Mn alloy, which is an example of precipitation hardening, the

shifting of the curve is not uniform. In other words, at low stress and high temperatures the effect of precipitates are more dominant than at lower temperatures and high stresses [126].

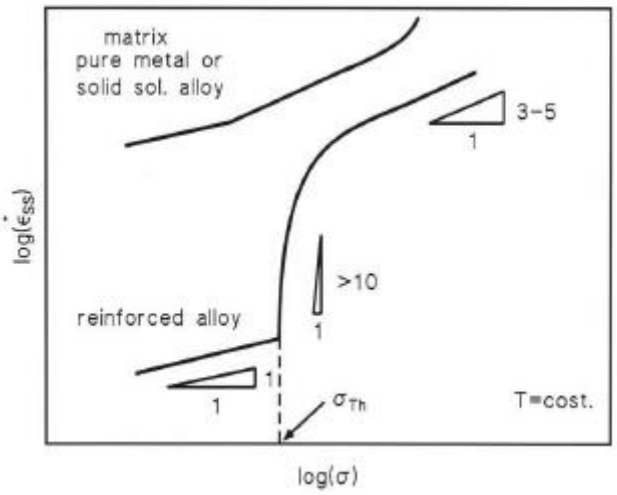

Figure 2.21. Schematic creep rate dependence on the applied stress for a particle reinforced alloy [96].

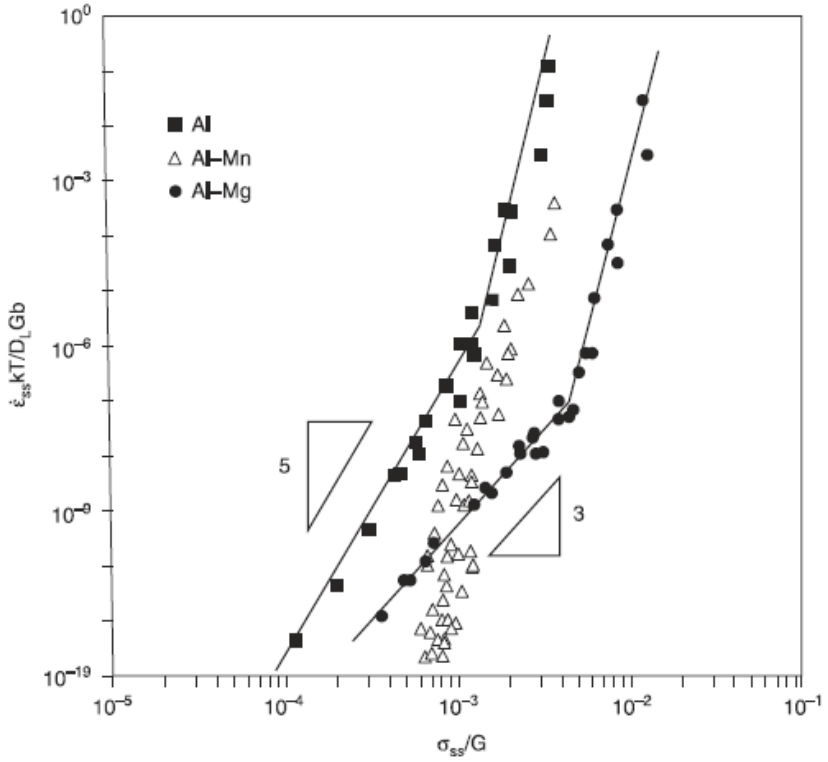

Figure 2.22. The creep rate vs. applied stress for different aluminum alloys [126].

Aluminum has a low melting temperature and hence, at relatively low temperatures the creep mechanisms are active in aluminum alloys. For this reason aluminum is one of the few metals which has been subjected to deeper creep investigations. Therefore, more accurate equations are available to evaluate the creep process, as well as, already investigated n and Q values of different alloys, which can be used as a reference. Eq. 26 shows the dependency of the steady creep rate on stress and temperature. It is a more accurate form of Eq. 19 for most aluminum alloys. [120]

$$\dot{\varepsilon_S} = A_0 * \frac{D_0 G b}{kT}\left(\frac{b}{D_g}\right)^p \left(\frac{\sigma}{G}\right)^n \exp\left(-\frac{Q}{kT}\right) \qquad \text{Eq. 26}$$

It has to be noted that the form of the formula may change in different publications and for different alloys, so a comparison of values and results has to be done carefully. In pure aluminum, the active creep mechanisms are the same as mentioned in all other pure metals.

Determination of the dominant creep mechanism becomes more complicated in alloys compared to the pure metals. The influence of precipitations, intermetallic compounds and impurity atoms have to be considered. The first regime (purely diffusion creep, Nabarro-Herring, Coble and Harper-Dorn Creep) and third regime (power law breakdown) remain mostly unchanged. The second regime (creep controlled by dislocation motion), can now be divided into three sub-regimes (see Figure 2.23) [120].

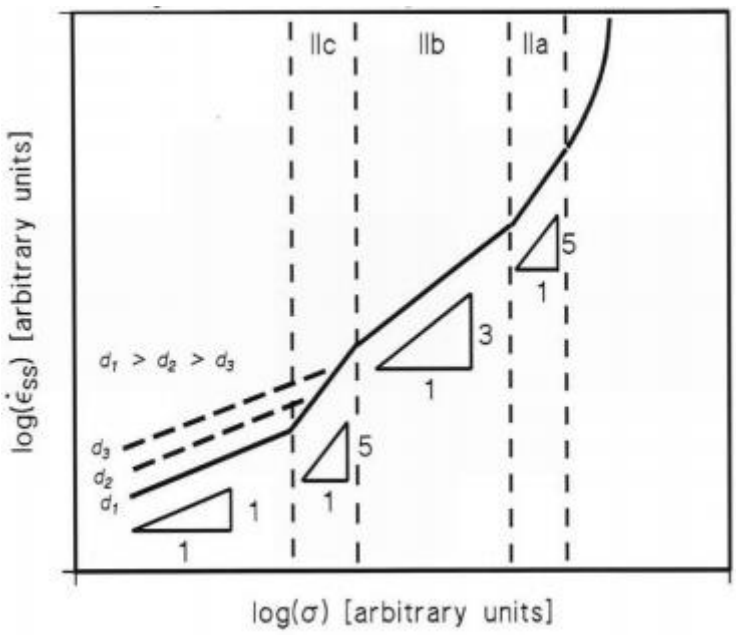

Figure 2.23. An example for n-values of alloys and solid solutions [120].

The first and third part in the second regime (IIa, IIc) are similar to the second regime in pure metals. The creep velocity is controlled by climb as it is the slowest mechanism. The reason for the sub-regime in the second regime is the attraction between dislocations and solute atoms. For lower stresses the velocity of the dislocation climb mechanism is lower than the diffusion rate of the solute atoms and the stress exponent is equal to pure metals with dislocation controlled creep. If the stress rises the dislocation climb velocity surpasses the diffusion velocity of the solute atoms. In this regime, the climb of the dislocations is restricted by the solute atoms, because the solute atoms are attached to the dislocation, so the dislocation movement is restricted and the slower mechanism controls the creep velocity (IIb) ("viscous drag"). If the stress rises more, the dislocations can break free from the solute atoms and dislocation climb is the controlling mechanism again [120], [130], [131].

The influences of alloying on the dominant creep mechanism depends strongly on the alloying elements and their concentration and it is not possible to give a general statement. [120]

In order to investigate the creep behavior of the materials, it is important to know that a high n-value may not always be accompanied by a low creep resistant alloy. A high n-value can also follow on a region, in which an increased creep resistance is present. This low creep rates are caused by inhibiting of the dislocation movement, for example by precipitations. These precipitations form a border, which the dislocations cannot surpass until a certain stress is reached. If this threshold stress is surpassed, the steady creep rate increases rapidly, until it is in the range of the steady-state creep rate of pure metal, or matrix. The steady-state creep rate will then proceed parallel to the curve of the matrix element. The upper line in Figure 2.21 shows a pure metal, while the lower one represents a reinforced alloy [120], [121].

The threshold stress often marks a border at which a change in the creep mechanism takes place. Dislocation motion can be suppressed up to a certain stress by the precipitations. By exceeding that stress the precipitations can be surpassed by different mechanisms, like cutting, Orowan by-pass and climb. In most cases, the Orowan mechanism, or in general bypassing mechanisms are the most common assumption, over cutting mechanisms [120]. If a threshold stress is determined, Equation Eq. 26 is reformulated as:

$$\dot{\epsilon_S} = A'_0 \times \frac{D_0 G b}{kT} \left(\frac{b}{d}\right)^p \left(\frac{\sigma - \sigma_{Th}}{G}\right)^n \exp\left(-\frac{Q}{RT}\right) \qquad \text{Eq.27}$$

An investigation by Deshmukh, Mishra, & Kendig showed that most of the used models to calculate the threshold stress in aluminum alloys are not able to represent the actual threshold stress, which was measured in experiments (see Figure 2.24). The experiments with the Al-6Mg-2Sc-1Zr alloy showed a strong decrease of the threshold stress with temperature. It drops from 97 MPa at 150 °C down to 8 MPa at 260 °C [132], [133].

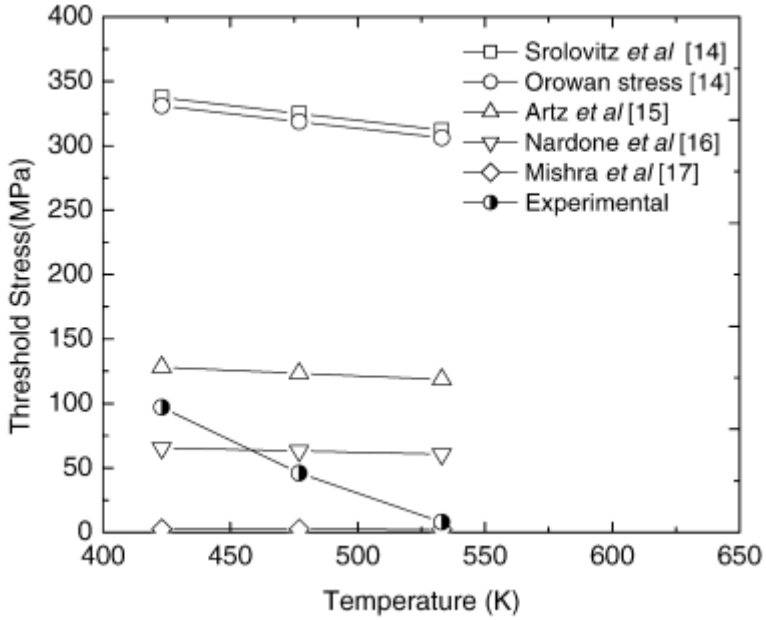

Figure 2.24. A comparison between calculated and measured threshold stresses [133].

To determine the threshold stress, the stress is plotted against the creep rate to the power of 1/n on a double linear scale, for different stress exponents (*n*). If the points are fitted to a straight line at constant temperature, according to the Eq.27 an extrapolation to zero strain rate gives the value of σ_{Th}. This method is not related to the double logarithmic methode, which used to calculate the n-value. An example is shown in Figure 2.25. The left picture shows a stress exponent equal to 3, while the right picture shows a stress exponent equal to 8. The middle picture represents the fitting stress exponent equal to 5. The intersection with the x-axis shows the point where the creep rate is zero, even though the applied stress is not zero. This value is considered as the threshold stress for the respective temperature [134]. The stress exponent equal to 3 is for creep dislocation glide [135], [136] , equal to 5 is related to dislocation climb (lattice diffusion) [135], [137], [138] and equal to 8 is for lattice diffusion-controlled creep with a constant structure [139].

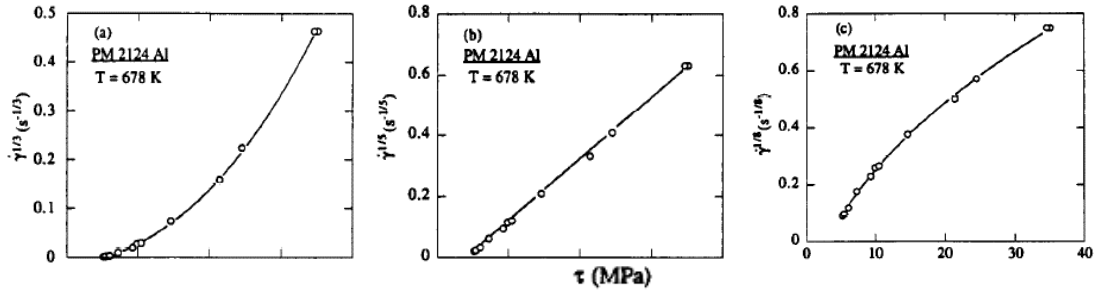

Figure 2.25. Graphic determination of a threshold stress [134].

3 Modelling of differential scanning calorimetry of precipitates

3.1 Introduction

6xxx series aluminum alloys containing Mg and Si have been considered as the most promising age-hardenable materials for automotive applications. These alloys have been the subject of several studies in recent years (e.g. [3], [7], [8], [22], [23]). In particular, Al-Si-Mg alloys have displayed excellent mechanical properties owing to substantial age-hardening upon heat treatment. To tailor precisely the mechanical properties of these alloys, it is fundamental to know the exact precipitation sequence and their corresponding kinetics of precipitation and growth. In this regard, experimental investigations have shown that the precipitation hardening response is related to the Mg-Si phases [9], [29]–[31]. The sequence of precipitate formation from the solid solution condition in Al-Mg-Si alloys with moderate Si content can be described as clusters → GP zones → β'' → β' → β (Mg_2Si), whereas the precipitation sequence of Al-Mg-Si alloys with high Si content has been described to be GP zones → small precipitates with an unknown structure → β'' → B' → Si → β (Mg_2Si) [32].

Owing to the difficulty of direct observation of the precipitation sequence, DSC has been used to determine the temperatures associated with precipitation and to capture the precipitation behavior indirectly, and has been simulated by means of the ClaNG model, which is based on the classical nucleation and growth theory. An advantage of DSC measurements is that the recorded curves show the precipitation and dissolution of precipitates in-situ [63], [69]. For this reason, DSC is also an option to validate simulation models. Understanding the precipitation kinetics during isothermal and non-isothermal heat treatments is essential to predict microstructural evolution and to tailor the alloy to specific applications. For this purpose, in recent years, the simulation of isothermal heat treatments has been investigated widely [75], [85], [87], [88]. However, either simulations of isothermal heat treatments were conducted (e.g. [140]–[142]) or simulations of non-isothermal heat treatments, which are more relevant for technical applications. Simulations of non-isothermal heat treatments have been less frequent to our knowledge, in particular, in conjunction with a comprehensive model validation (e.g. [89], [91]–[93], [95], [143]). This last point is very relevant because in most cases the validations of precipitation models have relied on observations with poor statistics owing to the very small size of the particles, such as particle size or volume fraction derived by Transmission Electron Microscopy (TEM) [88]. Evidently, dissolution and

precipitation of phases are difficult to characterize accurately by this method. An alternative approach is the use of DSC measurements that can capture such events depending on the type of the reaction. In fact, DSC curves have been frequently utilized to characterize phase transformations. In the specific case of Al alloys, DSC curves have also been simulated recently. For instance, Khan et al. introduced a first model for this purpose [89], [90] which was used by Falahati et al. [91]–[93] to simulate DSC curves in two aluminum alloys, 6xxx and 2xxx. Khan et al. defined the heat flow ϕ (unit: W/g) as:

$$\phi = \left(c_p^{sys} - c_p^{Al}\right) \cdot \dot{T} = \frac{d\left(h^{sys} - h^{Al}\right)}{dT} \cdot \dot{T} \qquad \text{Eq. 28}$$

where c_p^{sys} and c_p^{Al} are the alloy and pure reference aluminum specific heat capacities, respectively; h^{sys} and h^{Al} are the alloy and pure Al specific enthalpies, respectively, and $\dot{T}$ is the heating rate. It is noted that in this model the effect of interfacial energy on the heat flow has not been considered. Hersent et al. calculated the released or absorbed energy by using the classical Gibbs model [94]:

$$G_{sys}^{w} = \frac{1}{\rho}\left(\frac{g_{ss}^{m}}{V_{ss}^{m}} + \frac{\Delta g_p^m}{V_p^m} \cdot f_V + \gamma \cdot \frac{A}{V_{sys}}\right) \qquad \text{Eq. 29}$$

where G_{sys}^{w} is the total Gibbs energy per unit mass of the system, ρ is the mass density, g_{ss}^{m} is the Gibbs molar enthalpy of the solid solution, Δg_p^m is the difference of Gibbs molar energy between the precipitates and the solid solution, and V_{ss}^{m} and V_p^m are the molar volumes of the solid solution and the precipitates, respectively. f_V is the volume fraction of the precipitates and A is the total interface area developed by the precipitates. These models or slight variations thereof have been used to predict DSC curves. For instance, Starink et al. [89], [95] simulated the DSC curves of a 2024-T351 Al–Cu–Mg alloy using basically Khan's model (Eq. 1). They also studied the effect of the heating rate, which essentially shifts the precipitation reaction on the time axis, in a 2024-T351 alloy. In their approach, a time delay $\Delta t = \Delta T/\dot{T}$ was implemented that accounts for the fact that a certain undercooling ΔT is required to provide the energy needed to create the interface [89]. These models have simulated their specific DSC curves with good accuracy. In the present work, further improvements are made by accounting for the duration of precipitate nucleation after the particular phase becomes stable. In addition, nucleation at preexisting lattice defects is considered. The new model is

used to describe endothermic und exothermic reactions during heat treatment of an Al-Mg-Si alloys, and it is validated and calibrated by measured DSC curves.

3.2 Method

3.2.1 Experimental

AA6016, AA6005 and AA3105 aluminum alloys were investigated. The as-cast ingot of AA6016 was provided by Aleris Rolled Products Germany GmbH, and thermomechanically processed on an industrial scale at Aluminium Norf GmbH. For this work, the material was first cold rolled to a thickness of 1.15 mm. The material was then solution heat treated (SHT) in an air furnace at 560 °C for 5 minutes. TEM investigations were performed to determine the size and number density of particles for the following conditions: 20min, 1h, 4h, 24h artificial ageing at 185 °C. TEM foils with 3 mm diameter and about 0.1 mm thickness were cut and double jet-polished with an electrolytic solution of water-free A2 at 15 °C and 25–30 Volts. The TEM foils were imaged in a JEM FX2000. The precipitates were characterized by length and area of cross section with an estimated measurement error of 1 nm and 1 nm^2, respectively. The measured area of cross section was corrected with regard to the elastic coherency strain surrounding the particle [3]. The as-cast ingot of AA6005 and AA3105 aluminum alloys were provided by Hydro Aluminium Rolled Products GmbH. The as cast ingots of AA6005 and AA3105 aluminum alloys were homogenized for 24 h at 550 °C and subsequently hot extruded at 480 °C to a 10 mm thick by 50 mm wide rectangular profile.

For the validation of the model, an effective spherical radius of precipitates was calculated from the transformed volume of the assumed cylindrical particles into that of a sphere. For the calculation of the number density, the thickness of TEM samples was determined via the convergent beam electron diffraction (CBED) method together with a correction of the average particle length[144].

The DSC tests were conducted under argon atmosphere using a NETZSCH STA 449C device with two different heating rates of 5 and 10 K/min. The DSC measurements of AA3105 and AA6005 alloys were conducted at the Faculty of Mechanical Engineering and Marine Technology of University of Rostock using a Setaram 121 DSC device at by Richard Kemsies and Julia Osten under supervision of Prof. Kessler. The DSC tests of AA6016 alloy were conducted under argon atmosphere using a NETZSCH STA 449C device with two different heating rates of 5 K/min and 10 K/min. The tests were performed at temperatures between

100 °C and 500 °C to analyze the precipitation behavior of the samples. The samples have a cylindrical geometry with a dimension of Ø6 mm × 1 mm. In order to obtain corrected DSC curves, pure Al (99.999%) was used to measure the baseline of the device-specific heat-flow curvature. Its data was subtracted from the measured DSC curves of sample material to show the real heat effects of phase transitions. Moreover, during the measurements, samples are scanned against a similar empty crucible to ensure the symmetry of the tests. In addition, all measurements are started and ended with an isothermal step of 30 minutes taking account of the thermal inertia of device. DSC tests were repeated two times for each heating rate. The results presented are the averaged values of those measurements.

3.2.2 Simulation

Simulations were conducted with the ClaNG model [75], [145], which is based on the Kampmann and Wagner [83] numerical approach and is a classical nucleation model. The model includes homogeneous and heterogeneous nucleation. In the case of heterogeneous nucleation, the precipitation at grain boundaries and at dislocations were considered. In the computer program, a heat treatment was discretized into finite time intervals. All phases were described by size distributions. In each step, the critical nucleation radius and its respective critical nucleation work were calculated. Based on the Becker and Döring theory, the nucleation probability was calculated and added to the particle size distribution [27]. Then, growth and coarsening of the size classes are calculated. The mean radius, volume fraction, number density and heat flux are calculated at each time step. After each time step the new chemical concentration of the matrix was calculated and used in the next time step. Figure 3.2 shows the flow chart of the new ClaNG model.

3.2.2.1 Size distribution representation

The particle size distribution in the model is a combination of the Lagrange and Euler like approaches. This means that at each nucleation step one Gauss distribution of the particles will be added which can grow or shrink like a Lagrange like approach. Figure 3.1 shows the schematic of the combination of the Lagrange and Euler approaches.

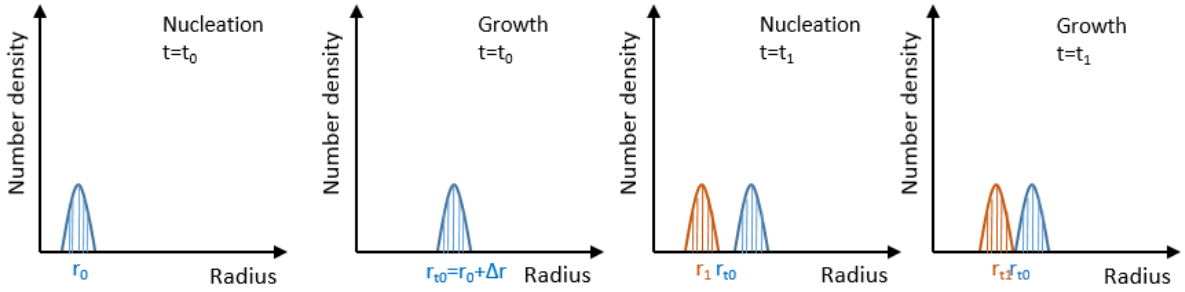

Figure 3.1. A schematic of the combined Lagrange and Euler approaches.

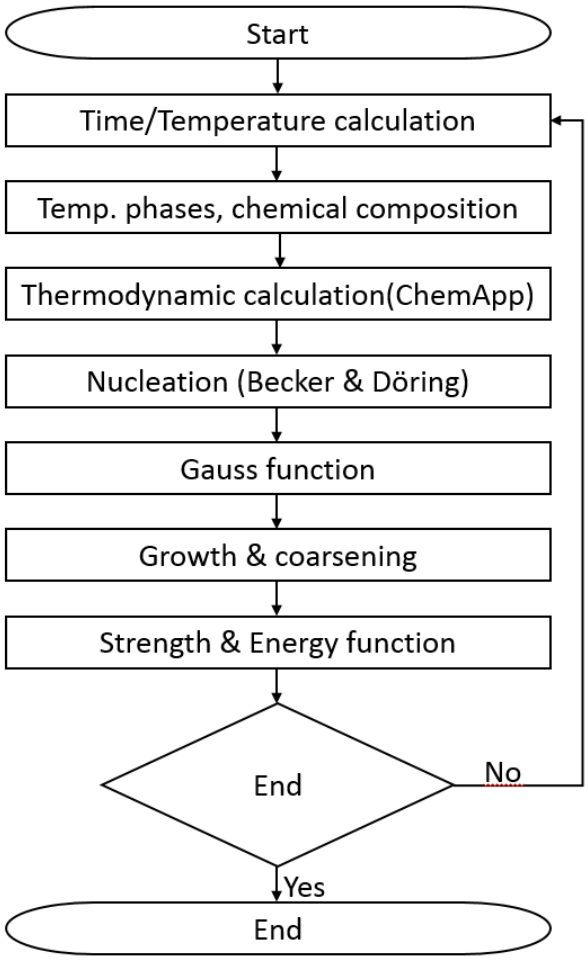

Figure 3.2. The flow chart of the ClaNG model.

3.2.2.2 Nucleation model

Here, the nucleation rate J is given by:

$$J = N_0 Z v \, exp\left(-\frac{\Delta G^*(r_c)}{k_B T}\right)\eta(t) \qquad \text{Eq. 30}$$

where N_0 is the number density of possible nucleation sites. For homogenous nucleation, N_0 equals to all atomic sites. In turn, heterogeneous nucleation sites are grain boundaries and dislocations. For the respective defects, the absolute number of nucleation sites is calculated by:

$$N_{gb} = \frac{3}{a^2 D_g} \quad \text{Eq. 31}$$

$$N_{dislo} = {}^{\rho}/_{a} \quad \text{Eq. 32}$$

where N_{gb} and N_{dislo} are the number density of possible nucleation sites at grain boundaries and dislocations, respectively. ρ is the dislocation density, a is the mean atomic distance and $\mathrm{D_g}$ is the grain diameter. In Eq. 33, Z denotes the Zeldovich non-equilibrium factor:

$$Z = f_z.\left(\frac{a^6}{64\pi^2 k_B T}.\frac{\Delta g_T^4}{\gamma^3}\right)^{1/2} \quad \text{Eq. 33}$$

$$\upsilon = \frac{4\pi(r_c.f_\upsilon)^2}{a^4} D_0 \quad \text{Eq. 34}$$

here, υ is the rate of atomic attachment to a growing nucleus. K_B is the Boltzmann's constant, T is the absolute temperature and ΔG* is the work of nucleation. In the present model, only dislocations and grain boundaries were considered as nucleation sites. r_c is the critical nucleation radius which can be calculated by:

$$r_c = f\frac{2\gamma}{-\Delta g_t} \quad \text{Eq. 35}$$

where γ is the interfacial energy, which was calculated based on by Nearest-Neighbor Broken-Bond model [146][71] and Δg_t is the chemical driving force as calculated by the ChemApp thermodynamic model based on the CalPhad approach and provided by GTT Technologies [147], [148]. The activation factor had originally been introduced [33] as

$$\eta(t) = exp\left(-\frac{\tau}{t-t_0}\right) \quad \text{Eq. 36}$$

where t_0 is the point in time when the particular phase reaches thermodynamic stability, and τ is the incubation time given by [149] :

$$\tau = \frac{1}{4\pi Z^2 \upsilon} \quad \text{Eq. 37}$$

Where the factors Z and υ, and hence τ strongly depend on temperature. In order to account for temperature changes $\dot{T}$ in the activation factor, the present work defines η by an activation rate $\dot{\eta}(T)$ and

$$\eta(t) = \int_0^{t-t_0} \dot{\eta}\left(t', \dot{T}\right) dt' \qquad \text{Eq. 38}$$

such that for $\dot{T}$ = 0, eq. (10) transforms into Eq. 36. In order to account for a heating rate $\dot{T}$, the usage of an activation rate $\dot{\eta}\left(t', \dot{T}\right)$ is proposed in Eq. 38. For simplicity, $\dot{\eta}$ is only approximated by a numerical approach:

$$\dot{\eta}\left(t', \dot{T}\right) = \frac{\left(\exp\left(-\frac{\tau}{t_{eff}^{i}+\Delta t}\right) - \exp\left(-\frac{\tau}{t_{eff}^{i}}\right)\right)}{\Delta t} \qquad \textit{Eq. 39}$$

where Δt is the time increment between subsequent time steps t^i and t^{i+1}, and $t_{eff}^{i} = -\tau/\ln\left(\eta\left(t^i\right)\right)$ is an effective, adjusted time (replacing the dependence on t') with the initiation $t_{eff}^{i}(0) = 0$ at the time t'=0.

A comparison of the heat flux and classical nucleation models have showed that any nucleation and growth of the precipitates are endothermic processes until the precipitates are 50% larger than the calculated critical size (see Figure 3.3). For this reason, a factor *f* in Eq. 4 was introduced and set to 2.0. Similar approaches have been also used before [90][150].

3.2.2.3 Growth model

In the ClaNG model, the SFFK growth and coarsening model is implemented based on a mean field approach [79], [80] . To be able to predict particle dissolution in the non-equilibrium condition [79], a growth model described below was used. In this model, the evolution of the precipitate radii r is determined by the growth rate, which in turn is defined by the chemical driving force and the capillary force.

$$\dot{r} = m \cdot \left(\Delta g_T - \frac{2\gamma}{r}\right) \qquad \text{Eq. 40}$$

Here m is the diffusion-controlled mobility of the interface, which is calculated from

$$m^{-1} = \frac{1}{M^{IF}} \cdot RT \cdot r \cdot \frac{\left(C_{KB} - C_{0B}\right)^2}{C_{0B} D_0} \qquad \text{Eq. 41}$$

Here, M^{IF} is an interfacial friction factor [71], which is fixed at 0.8. The respective data were directly taken from literature [151]. C_{KB} and C_{0B} are the concentrations of element B in the

precipitate and in the matrix, respectively. γ is the interfacial energy of different phases, $\frac{d_{chem}^{\beta}}{v^{\alpha}}$ is the chemical driving force for nucleation, which is derived by the software package ChemApp, and D_0 is the diffusion constant of the elements in the matrix, which was obtained from literature[151].

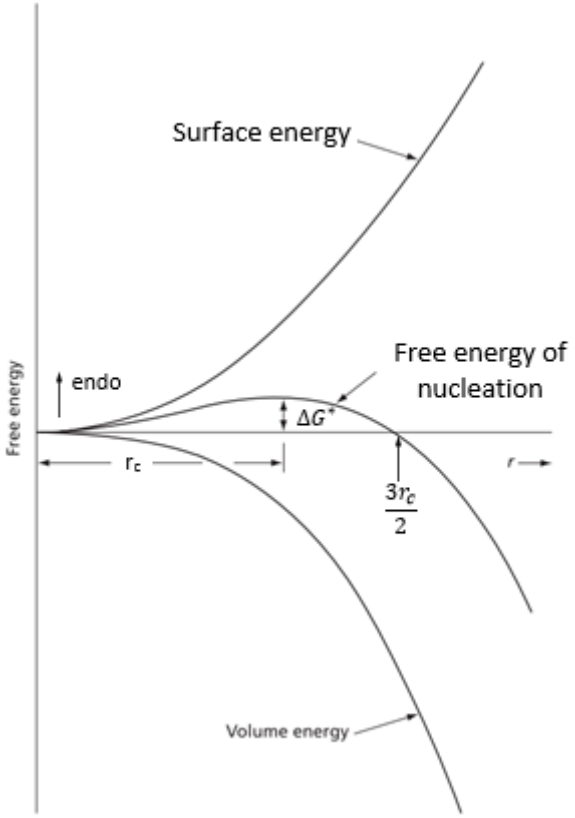

Figure 3.3. The free energy of a nucleation of a particle as a function of its radius.

3.2.2.4 Heat flux model

In order to calculate the heat flux, a system where the precipitates appear from a supersaturated solid solution was considered. The precipitates were considered spherical and their interfacial energy γ was assumed to be independent of the precipitate–matrix orientation relationship and temperature. Dislocations and grain boundaries were considered as possible heterogeneous nucleation sites. Under these considerations, the total change of the free energy ΔG yields:

$$\Delta G = \sum_k n_k(\Delta G^*(r_k) - \Delta G_{gb}(r_k) - \Delta G_{disl}(r_k)) \quad \text{Eq. 42}$$

where n_k is the number of particles in class k and $\Delta G^*(r_k)$ is the driving force and ΔG_{gb} and ΔG_{disl} are the grain boundary energy and dislocation energy released during precipitation of disk-like particles, respectively. The nucleation work at a grain boundary was assumed to be:

$$\Delta G_{gb} = 2\pi r^2 \gamma \quad \text{Eq. 43}$$

where γ is the interfacial energy, r is the radius of the particles. ΔG_{disl} is the energy of dislocations released during precipitation at dislocation lines [1]. The nucleation work is in turn calculated as:

$$\Delta G_{disl} = E_{dislo} * 2r_c = Gb^2 r_c \quad \text{Eq. 44}$$

The energy calculation in the model is conducted with units of (J/mole). With the purpose of comparing with the DSC curves, the energy is divided by the density ρ of the alloy to yield the total energy per unit mass:

$$q = \frac{1}{\rho}\sum_k n_k(\Delta G^*(r_k) - \Delta G_{gb}(r_k) - \Delta G_{disl}(r_k)) \quad \text{Eq. 45}$$

and the heat flux is calculated by:

$$\dot{q} = \frac{d}{dT}\left(\frac{1}{\rho}\sum_k n_k(\Delta G^*(r_k) - \Delta G_{gb}(r_k) - \Delta G_{disl}(r_k))\right) \quad \text{Eq. 46}$$

3.2.2.5 Strength model

Myhr et al. [88] used an strengthening model to calculate yield stress of an aluminum alloy. The model contains the intrinsic yield stress of pure aluminum (σ_i), solid solution hardening potential (σ_{ss}) and precipitation hardening (σ_p). In the ClaNG model this model was implemented.

$$\sigma_y = \sigma_i + \sigma_{ss} + \sigma_p \quad \text{Eq. 47}$$

The intrinsic yield stress of pure aluminum (σ_i) is 10 MPa. The solid solution hardening potential (σ_{ss}) is the summation of the contribution of each element:

$$\sigma_{ss} = \sum_j K_j C_j^{2/3} \quad \text{Eq. 48}$$

here C_j is the concentration of an element in solid solution and K_j is the corresponding scaling factor.

The precipitation hardening (σ_p)

$$\sigma_p = \frac{M}{b\bar{r}}(2\beta G b^2)^{-1/2}\left(\frac{3f}{2\pi}\right)\bar{F}^{3/2} \quad \text{Eq. 49}$$

where M is the Taylor factor and equal to 3.1, b is the burgers vector, G is the shear modulus of the aluminium matrix and β is a constant close to 0.5. $\bar{r}$ is mean particle size, f is mean particle size and $\bar{F}$ is the mean obstacle strength:

$$\bar{F} = \frac{\sum_i N_i F_i}{\sum_i N_i} \quad \text{Eq. 50}$$

where N_i is the number density of particles of a given size class. F_i is the obstacle strength.

$$F_i = 2\beta G b^2 \left(\frac{r_i}{r_c}\right) \quad \text{Eq. 51}$$

here r_i is the particle radius and r_c is the critical size ($r_c = 5\times10^{-9}$). If the particle is larger than critical size $\left(\frac{r_i}{r_c}\right)$ is equal to 1.

The yield stress is then converted to hardness HV.

$$HV = 0.33\sigma_y + 16.0 \quad \text{Eq. 52}$$

3.3 Results

3.3.1 Initial simulations results

At the beginning of the study, simulations were conducted to plan mandatory changes and to improve the simulation capability of the ClaNG model. Figure 3.4 shows a DSC simulation of AA3105. The model did not contain metastable phases, the dissolution of the particles does not take places over the time ,but instantaneously, and the heat flux model and strength model were not implemented. Accordingly, virtually no agreement between simulations and measurements had been found. Additionally particle distribution presentation was done by the Euler-like approach which is slow. Therefore, the following changes were made to improve the ClaNG model (see section 3.2.2):

1- A new database were added
2- A new growth law was implemented in code.
3- A combination of Lagrange and Euler like approaches were used.
4- A heat flux model was implemented.
5- A Strength model was implemented.

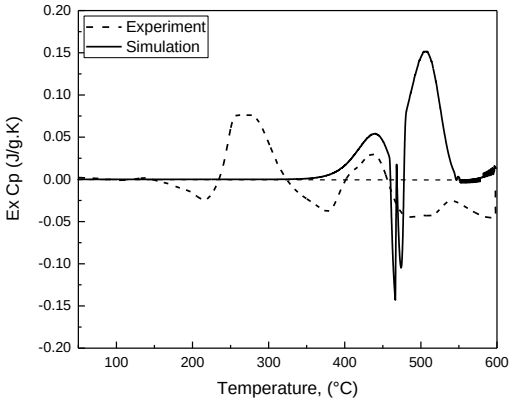

Figure 3.4. Example for the first comparisons between simulated and experimental DSC curves of AA3105 at 5 K/min.

3.3.2 Validation (6016)

In order to validate the models of nucleation and growth of the metastable and stable phases in the Al-Si-Mg system an isothermal heat treatment of an aluminum 6016 alloy was conducted at 185 °C. The model described in section 3.2.2 was used to simulate the number density and the mean radius evolution of the particle. The parameters used for the simulations are listed in Table 3.1.

Table 3.1. List of the parameters used in the simulations

Parameter	Eq.	Value	Unit	Physical meaning
Critical radius correction factor (f)	33	2.0	1	see discussion
Dislocation density	30	1×10^{11}	$1/m^2$	For an as-cast condition
Nucleation factor β (f_v)	32	3×10^{-4}	1	Size effect
Nucleation factor β' (f_v)	32	6×10^{-5}	1	Size effect
Nucleation factor β'' (f_v)	32	6×10^{-6}	1	Size effect
Zeldovich correction factor (f_z)	31	6.3	1	Size effect

Figure 3.5 shows a comparison of the simulated evolution of the mean radius and number density of the particles and the experimentally measured values. A good agreement is observed. The first stage of the simulation corresponds to the nucleation of metastable phases at the grain boundaries and dislocation sites. It continues until all of the nucleation sites are saturated. Then, the normal growth stage takes place until the matrix is depleted from the elements Mg and Si, and finally Ostwald ripening occurs.

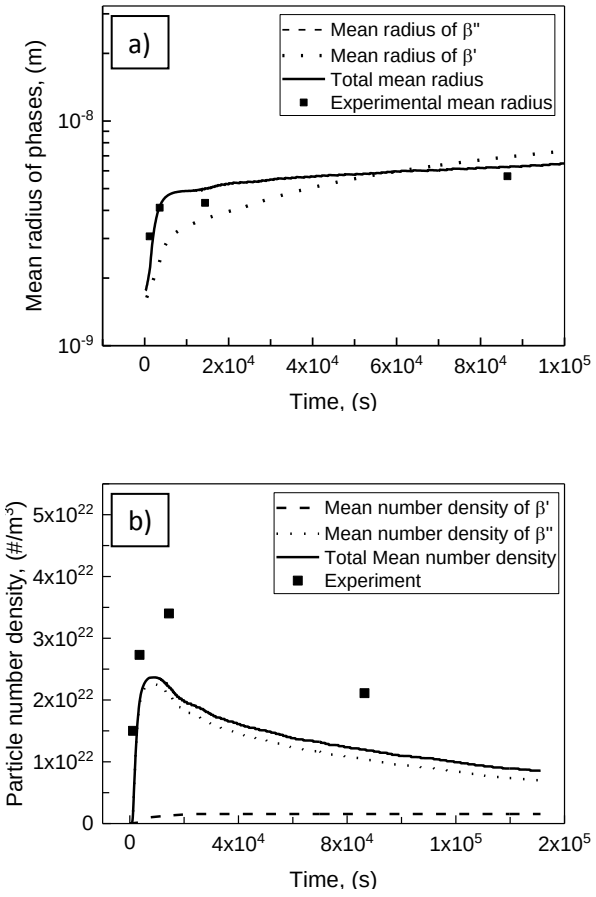

Figure 3.5. The evolution of (a) mean radius and (b) number density of the β" and β' particles at 185 °C respectively.

In the model, the balance between the chemical driving force and the capillary force determines whether a particle grows or dissolves. If the driving force is higher than the capillary force of the particles, the particles grow. When the concentration of dilute atoms in the matrix decreases, the capillary force becomes dominant for smaller particles and causes their dissolution leading to the growth of the larger particles.

Figure 3.6.a and b show the simulated and experimental DSC curves of the investigated AA6016 aluminum alloy obtained for heating rates of 5K/min and 10K/min, respectively. At 247 °C (in the experiment), an exothermic reaction corresponding to the precipitation of the β" precipitates was observed. The same occurred at 292 °C, when the precipitation of the β' phase occurred. By increasing the temperature further, the β" and β' particles dissolved and at 375 °C, and stable β particles precipitated. Finally, at 410 °C, the silicon rich particles precipitated [70]. In turn, Figure 3.6.b shows the DSC curves measured with a heating rate of 10K/min. At 252 and 300 °C, the exothermic reactions of β" and β' precipitation were

observed, consequently. By increasing the temperatures, the β" and β' particles dissolved and at 389 °C the stable β particles precipitated [70]. The precipitation of the silicon rich particles occurred at 447 °C. The simulations showed the same tendency. However, the rate of the energy change was faster than in experiments. This is due to a higher nucleation rate and faster growth kinetics, compared to the experiments.

Figure 3.6.c and d show the simulated and experimental DSC curves of the investigated AA6005 aluminum alloy obtained for heating rates of 0.6 K/min and 6 K/min, respectively. As the material did not contain an excess of Si, the peak of the Si precipitates is not observed. Increasing the heating rate causes a shift of the peaks to higher temperatures.

Figure 3.6.e and f show the simulated and experimental DSC curves of the investigated AA3105 aluminum alloy obtained for heating rates of 0.6K/min and 1.2K/min, respectively. According to the TEM investigation on DSC samples, a new peak occurs at 375 °C and 0.6 K/min. This is attributed to the formation of the α-Al(Mn,Fe)Si phase. This section is just about the modeling and the TEM investigations will be discussed more in detail in section 4.3.

Figure 3.7.a shows the simulated and experimental enthalpy change of the AA6016 aluminum alloy obtained for heating rates of 5K/min from a supersaturated solid solution. In order to compare the curves, the enthalpy change for the GP Zone region and the Fe and Mn primary precipitates, which were already present in the matrix, were subtracted. This data is shown in Figure 3.7.b. The simulated change of enthalpy for the same heating rates is of the same order of magnitude as that of the experimental results and, more importantly, shows exactly the reactions as the experimental one. Figure 3.7.c-f show the simulated and experimental enthalpy change of the AA6005 and AA3105 aluminum alloys obtained for heating rates of 0.6 and 1.2 K/min from a supersaturated solid solution and as-cast conditions, which show same trend of the precipitation. In Figure 3.7.b and d, the simulated curves end at the same energy level where they start, this reflects the fact that before and after the heat treatment all foreign atoms were fully solved in the matrix. This is due to the dissolution of the Mg-Si and Si particles, but in AA3105 aluminum alloy the end point is not zero. This is due to the low diffusivity of the Fe atoms, which caused the α -Al(Mn,Fe)Si to not dissolve completely.

Figure 3.8.a-b show the simulated evolution of particle number density for different heating rates of AA6016 aluminum alloy. Increasing number density shifts all the peaks to lower

temperatures and the number densities are also higher. Additionally, the particles are dissolved at lower temperatures when the heating rate is slower.

Figure 3.8.c-d show the evolution of the mean radius for different DSC curves of AA6016 aluminum alloy. With 10K/min heating rate, the β" precipitation occurred at 200 °C and the last precipitates dissolved at 320 °C. Decreasing the heating rate led to a shifting of the nucleation growth and dissolution to lower temperatures. The maximum mean radius was higher in the samples annealed at a lower heating rate. The mean radius of Si precipitates showed a serration, which is attributed to the increase of the driving force of the silicon particles nucleation due to the solute enrichment of the matrix resulting from the dissolution of the formerly stable β particles.

Figure 3.8.e-f show the volume fraction of different phases during DSC test of AA6016 aluminum alloy. Decreasing the heating rate shifts the peaks to a lower temperature, but the height of the peaks is higher. This means the maximum volume fraction of the particles is larger than at the higher heating rate condition. This is attributed to the growth time, which is longer for the lower heating rate.

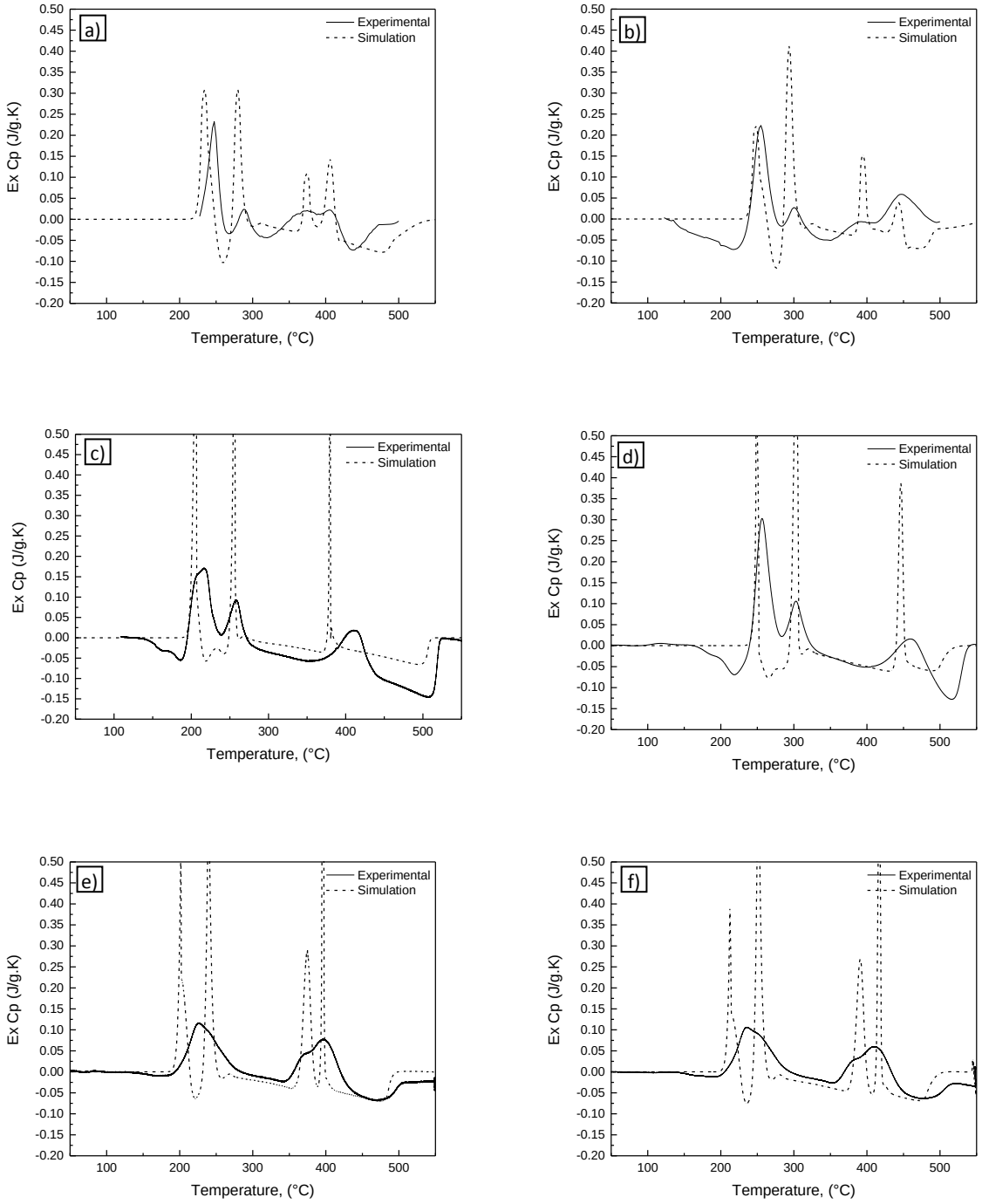

Figure 3.6 The simulated and experimental DSC curves of an AA6016 aluminum alloy with a heating rate of with (a) 5K/min and (b) 10 K/min, an AA6005 aluminum alloy with a heating rate of with (c) 0.6 K/min and (d) 6 K/min and an AA3105 aluminum alloy with a heating rate of with (e) 0.6K/min and (f) 1.2 K/min respectively.

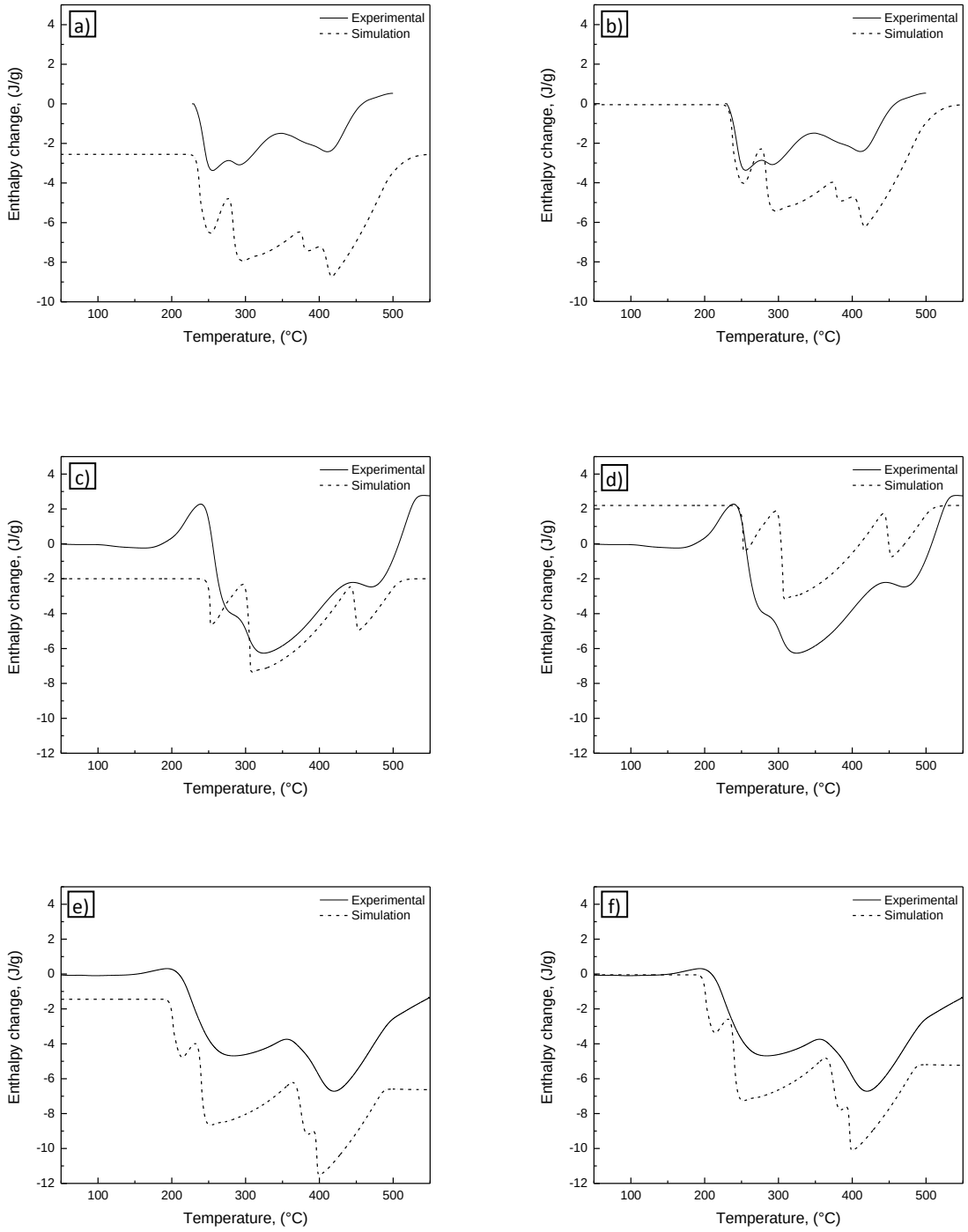

Figure 3.7. The simulated and experimental enthalpy change with and without considering GP zone and primary precipitates for (a-b) an AA6016 aluminum alloy with a heating rate of with 5K/min, (c-d) an AA6005 aluminum alloy with a heating rate of with 0.6 K/min and (e-f) an AA3105 aluminum alloy with a heating rate of with 0.6K/min respectively.

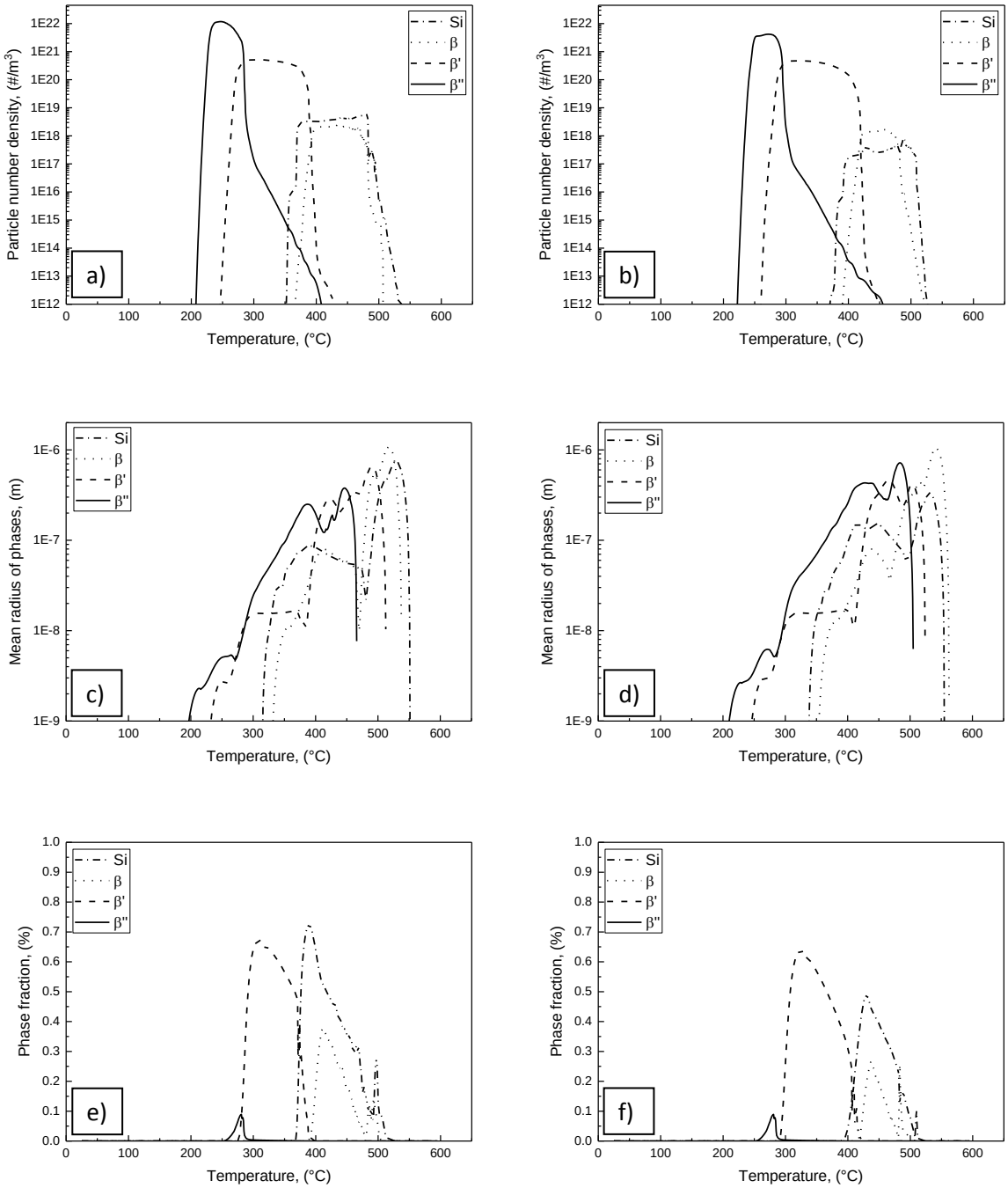

Figure 3.8. Simulated (a,b) particle number density, (c,d) mean radius and (e,f) phase fraction for a heating rate of (a,c,e) 5 K/min and (b,d,f) 10 K/min.

Figure 3.9 shows the particle number density, mean radius and phase fraction of precipitates for different heating rates of AA6005 aluminum alloy. The microstructure contains just Mg-Si particles, and the Si content is not high enough to precipitate Si particles.

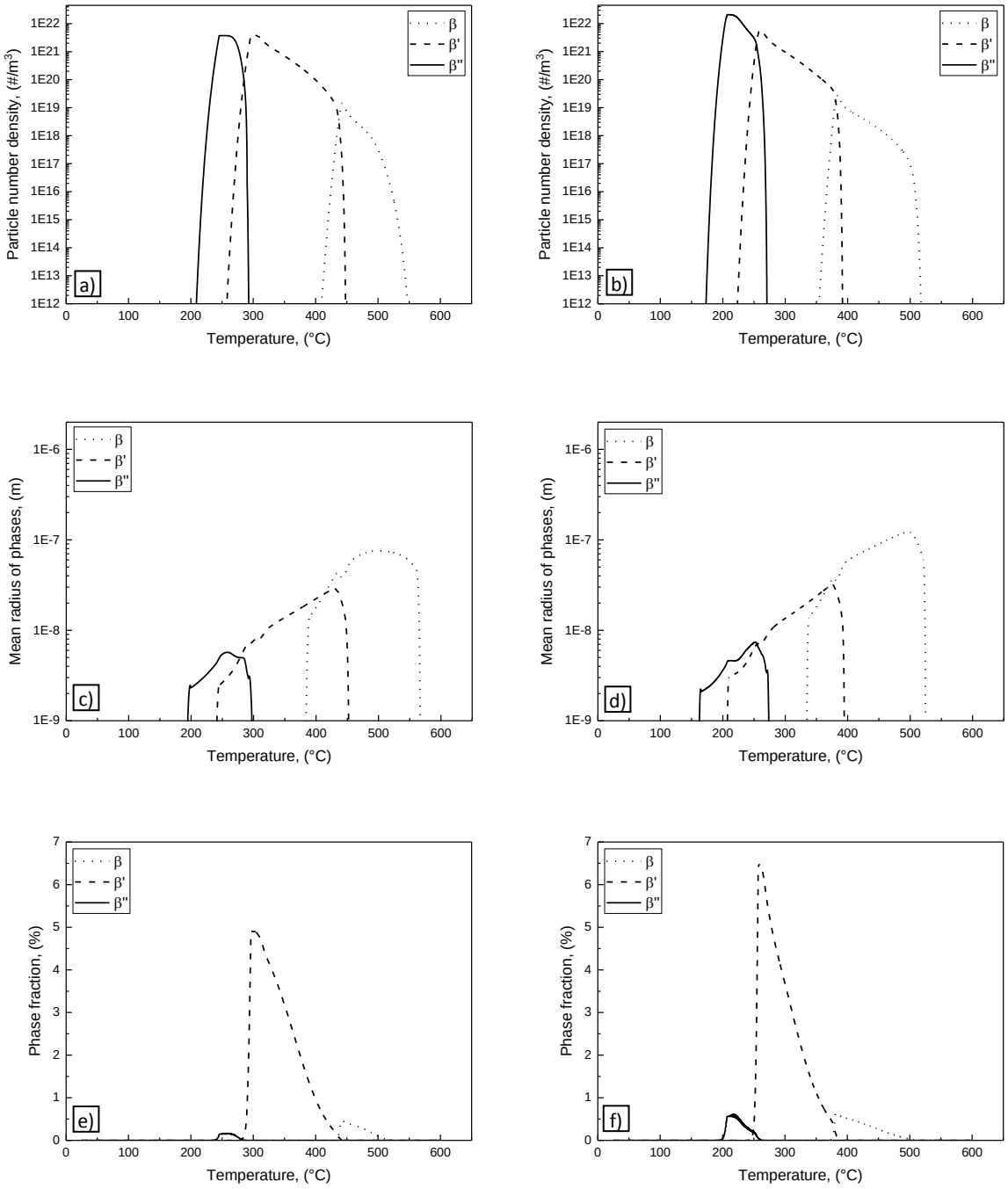

Figure 3.9. The simulated (a,b) particle number density, (c,d) mean radius and (e,f) phase fraction for a heating rate of (a,c,e) 6.0 K/min and (b,d,f) 0.6 K/min of AA6005 aluminum alloy.

The evolution of the particle number density, mean radius and phase fraction of precipitates of AA3105 aluminum alloy during DSC measurement is shown in Figure 3.10. Two different heating rates were simulated. Figure 3.10.a, c and e show the simulations for a heating rate of 0.6 K/min and (b,d,f) for 1.2 K/min. The microstructure contains Mg-Si particles and α-Al(Mn,Fe)Si.

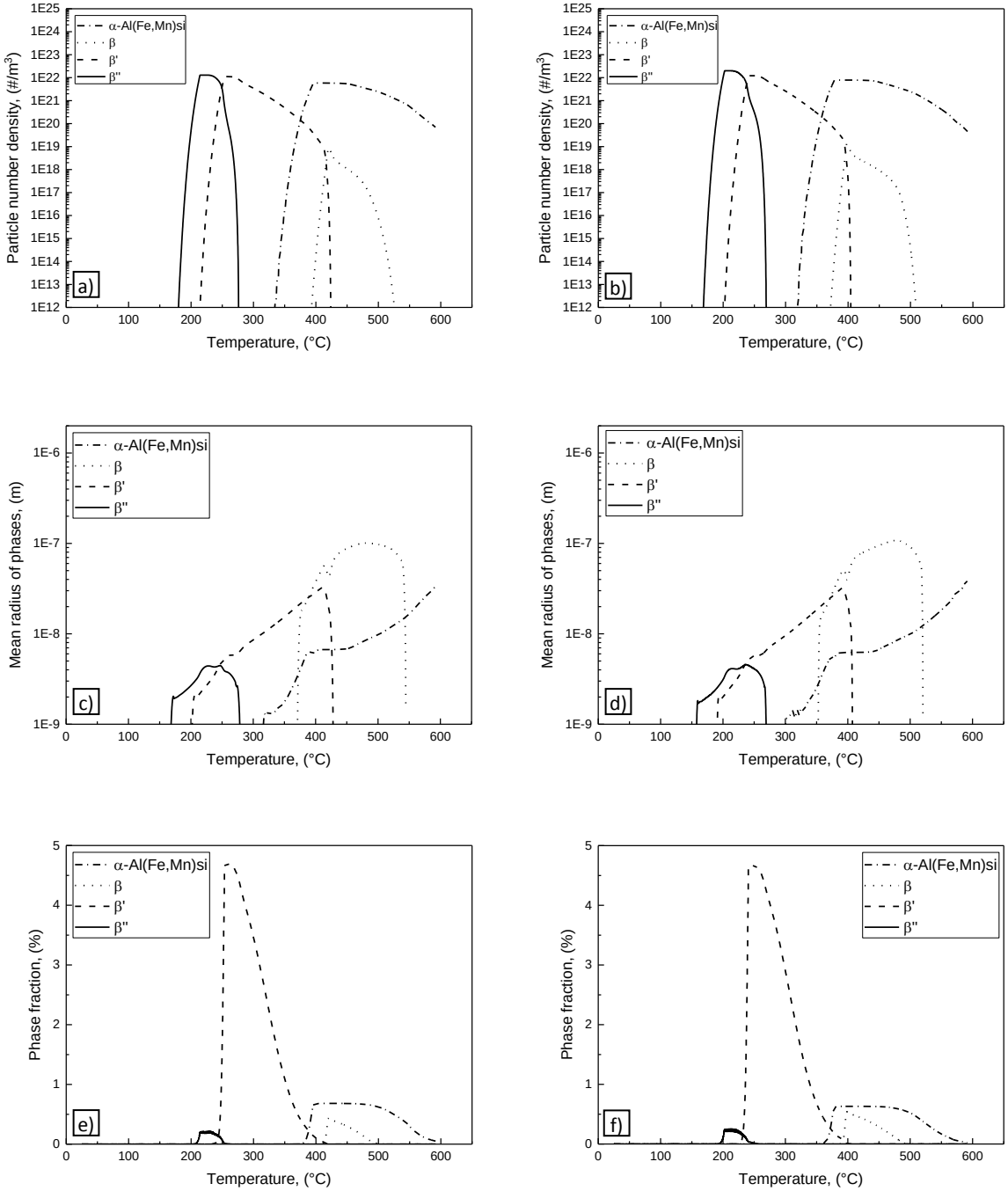

Figure 3.10. The simulated (a,b) particle number density, (c,d) mean radius and (e,f) phase fraction for a heating rate of (a,c,e) 1.2 K/min and (b,d,f) 0.6 K/min of AA3105 aluminum alloy.

The simulation results were compared to results of the DSC experiments. The simulation results showed a very good agreement with the experimental results. The model can be used to predict results of a new proposed heat treatment.

3.3.3 Proposed heat treatment for AA3105

In order to obtain a creep resistant AA3105 aluminum alloy and improve its high temperature mechanical properties, the validated model was used. Randomly distributed fine Al(Mn,Fe)Si particles, which are more stable than Mg-Si particles at high temperatures, were used to obtain an improved creep resistant AA3105 Aluminum alloy.

An isothermal heat treatment was simulated at 265°C for 25 hours. Figure 3.11 shows the hardness change with respect over the time. The first peak which is observed after 8 hours is obtained from fine Mg-Si particles. After 8 hours, overaging and coarsening take places and the contribution of Mg-Si particles to the hardness decreased. Simultaneously, nucleation of α -Al(Mn,Fe)Si particles was observed, which increased the hardness again after 15 hours.

The simulations shows that AA3105 can be optimized for high temperature application. The fitting parameters for the simulated hardness during the heat treatment were valid for Mg-Si particles and we assumed that the α -Al(Mn,Fe)Si particles have the same fitting parameters. This assumption reduce the accuracy of the data. In chapter 5 experimental heat treatments were conducted to find the best heat treatment to get the maximum hardness.

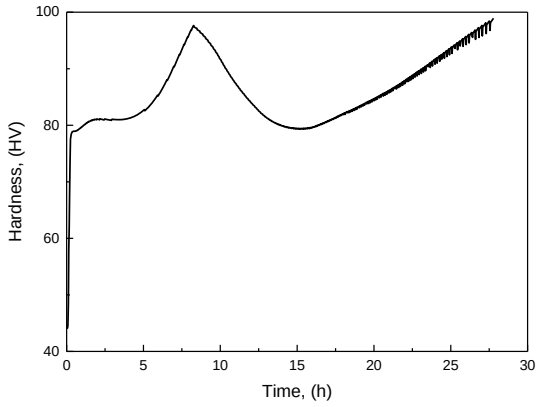

Figure 3.11. The simulated isothermal heat treatment of AA3105 aluminum alloy at 265°C.

3.4 Discussion

3.4.1 Microstructure evolution and DSC curves interpretation

The TEM investigation on the DSC AA3105 samples showed that the precipitation sequence of the AA3105 from the as-cast condition is not the same as the precipitation sequence after homogenization. Details of the TEM investigations will be explained in chapter 4. Here the

relevant information for the model validation are explained. TEM diffraction patterns showed that the formation β'' and β' occurred at temperatures between 230 - 330 °C. At higher temperatures two peaks were observed. The first peak, which has not been reported previously, is attributed to the precipitation and growth of α-Al(Mn,Fe)Si particles. The formation of α-Al(Mn,Fe)Si particles from the as-cast condition is due to the solidification of the alloys in a non-equilibrium condition, in which the diffusion of solute elements in the melt is higher than that in the solid. Therefore, the final composition of the matrix is not same as the expected equilibrium matrix concentration. From Figure 4.1 and Figure 4.2 the precipitation sequence of the AA3105 aluminum alloy from the as-cast condition can be described as GPI zones → β'' → β' → α -Al(Mn,Fe)Si → β (Mg_2Si). A different heating rate shows that the increasing heating rate shifted the peaks to higher temperatures.

The thermodynamic assessment of the metastable phases was based on the CALPHAD approach [93]. The evolution of metastable and stable particles and the heat flux evolution during DSC of the alloy in continuous heating experiments were simulated. Simulation results of isothermal heat treatment of a 6016 aluminum alloy at 185 °C showed a good agreement with experimental findings. As the β" and β' particles could not be discriminated experimentally in TEM investigations, a separate particle number density was not measured. The simulations showed that the precipitated β" particles dissolved and more stable β' particles precipitated and grew.

Simulation of non-isothermal heat treatment were calculated for the AA6016 alloy based on Eq. 46, in which, the interfacial energy was considered as the barrier energy for homogenous nucleation at grain boundaries whereas the elastic energy of dislocations and the formation enthalpy of the phases were considered to be released when precipitates formed. However, according to thermodynamic models, the chemical driving force decreases with decreasing concentration of solute atoms and with increasing temperature, which lead to a wrong energy release, although the particles are not dissolved. This leads to an energetic discrepancy between the endothermic and exothermic reactions, as indicated in Figure 3.12.Here, a closed loop of precipitation and dissolution at two constant temperatures, T1 and T2, is plotted in the AA6016 phase diagram, which was calculated using FactSage software [152]. If an isolated system was considered, according to the first law of thermodynamics, the energy released during the nucleation and growth of precipitates should be the same as the one absorbed

during dissolution. For precipitation which is occurring during cooling from T_2= 723 K to T_1 = 718 K in a super saturated solid solution FCC-Matrix M with a composition x_0,

M(x0) → M(x) + ß' , ΔHR(T1) = -19,623 J

During heating to T2 = 723 K,

M(x) + ß' → M(x0), ΔHR(T2) = +19,634 J

However, dissolution occurs when the temperature is increased, and the precipitated phase is not thermodynamically stable anymore. Therefore, without correction, the driving force for the calculation of the heat flux is zero in this case, which is physically inconsistent. To overcome the problem of calculating a chemical driving force for the dissolution of particles at non-equilibrium temperatures (particles are unstable at dissolution temperature), this force was considered constant and equal to the chemical driving force at a fixed reference temperature, which was chosen to be 25°C. During precipitation, the entropy decreases, and enthalpy becomes dominant. During dissolution, the entropy, which would compensate an equal amount of the enthalpy released during nucleation and growth, is absorbed. This means that the particles simply collapse under the effect of the capillary force of their interface. This assumption was a necessary step in order to calculate reasonable enthalpy change curves in Figure 3.6, where in good agreement between experiments and simulations, the total enthalpy change after formation and dissolution of several phases must be close to zero.

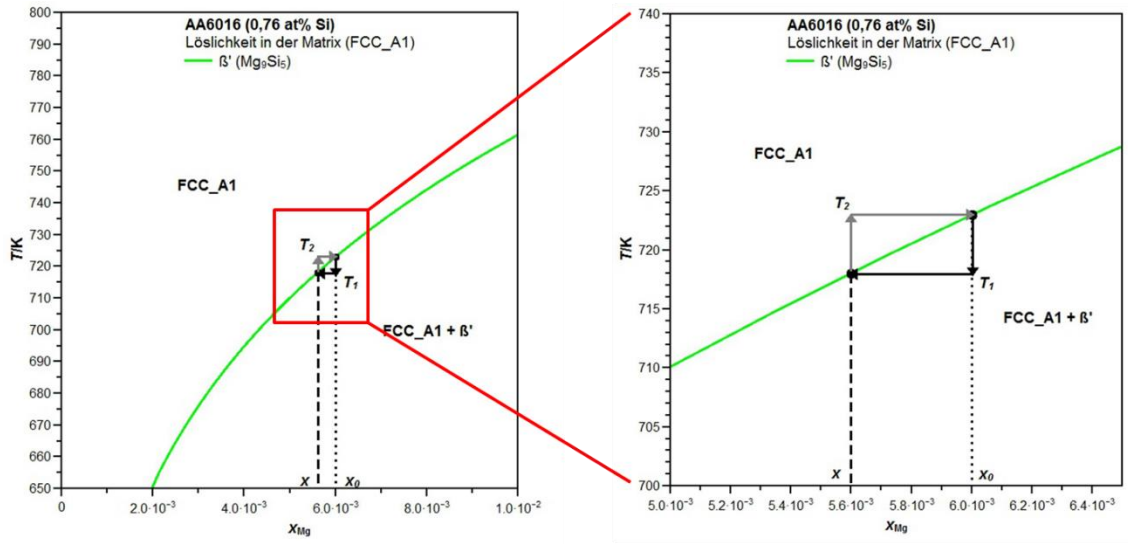

Figure 3.12. A Phase diagram of precipitation and dissolution of a β' from aluminum matrix.

Figure 3.6.a-f show that the implemented incubation model calculated the incubation time correctly. The model was able to predict the shifts in temperature of the reactions caused by the different heating rates and different chemical compositions. Increasing the heating rate decreased the period and it led to the shifting of the nucleation to higher temperatures. Unfortunately, Figure 3.6.b does not contain the dissolution of the Mg_2Si and Si particles because the experimental tests were conducted only up to 500°C, therefore the simulated dissolution of the Mg_2Si and Si particles cannot be compared with experiments. Figure 3.7.a-b shows the simulated and experimental enthalpy change of the AA6016 aluminum alloy. The excess C_p is the first derivative of the energy with respect to the temperature. A higher simulated excess C_p compared to the experimental one is related to a higher nucleation rate in the simulations. Nevertheless, the released total energy was the same. In the other words, comparing the DSC curves without comparing the enthalpy change is not enough to assert the accuracy of the simulations. The enthalpy change curves show the total energy, which is released and absorbed during the heat treatment. The amount of the released and absorbed energy before the precipitation and after dissolution of the particles should be the same. The DSC curves are the summation of the exothermic and endothermic reactions in a material. During the heating, Mg atoms can precipitate in the form of the Mg-Si stable and metastable phases. By increasing the temperature their chemical driving force decreased and they dissolved. The difference between experimentally measured enthalpy change and simulated enthalpy change between 100-230 °C is attributed to the dissolution of the GP zones, which are not considered in the model and are not available in the database. Additionally, the shift along the enthalpy change axis is related to the Fe and Mn primary precipitates, which are already present in the matrix. These particles originated during solidification. For this reason, their released energy cannot be measured using the DSC device. Figure 3.7.b shows the enthalpy change for the same condition without considering the GP zones and primary precipitates. The simulation results showed a tendency similar to the experiment. As spherical particles have the lowest surface to volume ratio and only spherical precipitates are considered in the model, a higher enthalpy change in the simulation result was expected and observed dominantly at higher temperatures.

The precipitation sequence of AA6016 aluminum alloy according to the simulations was β'' → β' → Si→ β (Mg_2Si). This sequence is consistent with literature [153]. As the Mg_2Si phase

is not stable at temperatures higher than 475 °C, it is not possible to determine its precipitation at 450 °C. However, the Si particles are stable at higher temperatures. The peak at 375 °C represents nucleation and growth peak of Si-rich particles. In other sources, the peak is attributed to uncertainties in the base line construction in DSC experiments[91].

Figure 3.8 show the dissolution of the stable and metastable precipitates at different temperatures and for different heating rates. According to the phase diagrams, different particles can be stable and stay in the matrix until the temperature reaches the border of the phase diagram, but different DSC simulations with different heating rates showed different nucleation and dissolution temperatures for the same phases. When the heating rate is high, the precipitates nucleate later and at higher temperatures. Therefore, the particles are bigger. As the temperature increases with a constant heating rate, the driving force decreases and eventually becomes smaller than the capillary force. In the case of a lower heating rate, the particles are smaller, and they will precipitate at lower temperatures. Although they have more time to grow, the increase of temperature causes the particles to be unstable and the capillary force becomes dominant. Therefore, the particles dissolve at lower temperatures compared to the higher heating rates. This description is important to understand the effect of the capillary force also for coarsening and the kinetic of the stable precipitates formation from metastable precipitates.

3.5 Conclusion

In this study, the microstructural evolution of a homogenized AA6016, AA6005 and an as-cast AA3105 aluminum alloy was simulated by means of the ClaNG model. The ClaNG model was coupled with a thermodynamic database. Isothermal and non-isothermal heat treatments were conducted. A new model was used to simulate the incubation time. The heat flux evolution during DSC of the alloy in continuous heating experiments was simulated. The simulations were in a good agreement with experimental data. The evolution of the metastable and stable phases was well reproduced by the computer simulations. Additionally, the results point out that the DSC curves are better tools to calibrate the models than TEM investigations. The DSC simulation can be used to interpret the DSC curves. DSC curves with different heating rates are useful tools to validate the models.

4 Effect of Mg content on the precipitation sequence of as-cast AA3105 aluminum alloys

4.1 Introduction

AA3xxx series aluminum alloys are mainly used in architecture and packaging, applications in which high ductility and corrosion resistance are needed. The main alloying element in these alloys is Mn [9]. During heat treatment different phases from metastable to stable particles can precipitate. These precipitates have an influence on the microstructure evolution during the processing of the alloys as they affect and influence recrystallization, texture formation, grain diameter, and more importantly, mechanical properties as well as electrical conductivity [154], [155]. AA3xxx alloys are considered as non-heat-treatable alloys. In the binary systems Al–Mn or Al-Fe, the decomposition from the supersaturated solid solution is very slow [48], [58], [156], [157] owing to the low mobility of Mn and Fe in the Al matrix. Recently, Liu et al. reported that precipitation of dispersoids in an as-cast AA3004 alloy improved the mechanical properties and electrical conductivity [51], [52]. Liu et al. investigated the effect of Fe on the precipitation hardening of AA3004 and reported that an alloy with 0.3 wt.% Fe has the best combination of yield strength and creep resistance due to the uniform distribution of fine size dispersoids [158]. A way to improve the yield strength in these alloys is adding Mg to promote dispersion hardening and solid solution strengthening [159]. In addition, additions of Si can be used to increase the precipitation rate of second-phases [156], [160]. During the ageing of AA3xxx alloys, a significant precipitation strengthening was achieved through precipitation of partially coherent α-Al(Mn,Fe)Si dispersoids [53]–[57]. Besides precipitation of α-Al(Mn,Fe)Si dispersoids in AA3xxx alloys, the dissolution of Al_6(Mn,Fe) particles has been observed [58], [59]. AA3xxx alloys usually contain Mg, Si and Fe as well as Mn and show the same precipitation sequence as AA6xxx alloys. The presence of the Mg and Si elements, which are the major elements in AA6xxx series aluminum alloys, have great influence on the precipitation behavior of the AA3xxx alloys. These alloys have been investigated widely in recent years because of their age-hardening potential and are used in the automotive industry as body sheet material [3], [22], [23]. Al-Si-Mg aluminum alloys show a remarkable response to age-hardening. As a result, the precipitation behavior of Al-Si-Mg aluminum alloys has been studied extensively (e.g. [9], [29]–[31]). The precipitation hardening response in Al-Si-Mg aluminum alloys is related to the Mg-Si phases. The sequence of the precipitation formation

from a solid solution condition in Al-Mg-Si alloys is described as *cluster* → *GP zones* → β'' → β' → β *(Mg_2Si)*[30], [161], but the precipitation sequence of Al-Mg-Si alloys with high silicon content is described as *GP zones* → *small precipitates with an unknown structure* → β'' → B′ → *Si* → β *(Mg_2Si)*[32].

In the present chapter, the precipitation sequence of a AA3105 aluminum alloy with and without Mg addition is elucidated by means of TEM measurements and DSC [63], [69]. Additionally, phase identification is conducted for AA3105 alloy, particularly for the peak at 375°C. These determined phases were used to validate the simulations of DSC curves.

4.2 Methods

The chemical composition of the alloys, received in as-cast condition, is listed in Table 4.1. The chemical composition of the whole materials in this study were measured with Atomic emission spectroscopy. The ingot was provided by Hydro Aluminium Rolled Products Germany GmbH. TEM investigations were performed using a FEI Tecnai F20 microscope operated at 200 kV to determine the size of the particles for different conditions by S. Zischke at Central Facility for Electron Microscopy, RWTH of Aachen. TEM samples were ground down to 4000 grit and then electro polished with AC2 at 17 °C and 30% HNO_3 and 70% Methanol at -30 °C. DSC tests were conducted using a Setaram 121 DSC device at 0.01 K/s. These DSC samples were prepared at the University of Rostock, Faculty of Mechanical Engineering and Marine Technology, Chair of Materials Science, by R. H. Kemsies under supervision of Prof. O. Keßler.

Table 4.1. The chemical composition of the AA3105 aluminum alloy with and without Mg addition

Alloy	Si(wt.%)	Fe(wt.%)	Cu(wt.%)	Mn(wt.%)	Mg(wt.%)	Al
AA3105	0.48	0.38	0.145	0.7	0.6	balanced
AA3105	0.50	0.38	0.142	0.71	-	balanced

4.3 Result and discussion

Figure 4.1.a shows the experimental DSC curve of the AA3105 aluminum alloy with a heating rate of 0.01K/s. Figure 4.1.b-f show the dark-field and selected-area electron diffraction (SAED) pattern of the samples, which were heated up to temperatures of 240, 300, 375, 405 and 500 °C and subsequently quenched. The chosen temperatures are at the exothermic or endothermic peaks, which may indicate nucleation or dissolution of particular phases. The

first exothermic reaction at 240 °C corresponds to the precipitation of the needle-like β" precipitates. This was verified by comparing the SAED pattern with the same patterns found in the literature[30], [162]. At 300 °C, an endothermic reaction signifying the dissolution of the β'' precipitates was observed. By increasing the temperatures further, the β" and probably β' particles, which were not verified by SAED pattern, dissolved. The evaluation of SAED patterns and STEM images of dominant precipitates at 375 °C showed that the particles with a mean radius of 12 ± 4.8 nm have a coherent phase boundary with the matrix. According to the calculated lattice plane spacing (d), the α-Al(Mn,Fe)Si has the best fit between the experiments and literature [163]. The Energy-dispersive X-ray Spectroscopy (EDS) measurements showed that the phase contains the elements Al, Fe, Mn and Si. At 405 °C, the β particles precipitated. These particles have a larger mean radius compared to the α-Al(Mn,Fe)Si particles. The mean radius of the α-Al(Mn,Fe)Si particles is 46 ± 18.5 nm. By increasing the temperature to 500 °C, the β precipitates are dissolved and coarsening occurred. Afterwards, the mean radius of α-Al(Mn,Fe)Si particles was found to be 73 ± 31.5 nm. Simultaneously, the α-Al(Mn,Fe)Si particles became entirely incoherent, which explains that no SAED diffraction patterns of particles (superstructures) were visible. To summarize, the most probable precipitation sequence of the AA3105 aluminum alloy was found to be: (*GP zones)* → β'' → β' → α*-Al(Mn,Fe)Si* → β *(*Mg_2Si*)*. The proposed precipitation sequence does not claim that the α-Al(Mn,Fe)Si particles precipitate directly from metastable phases or that β precipitates are precipitated from the α*-Al(Mn,Fe)Si* particles.

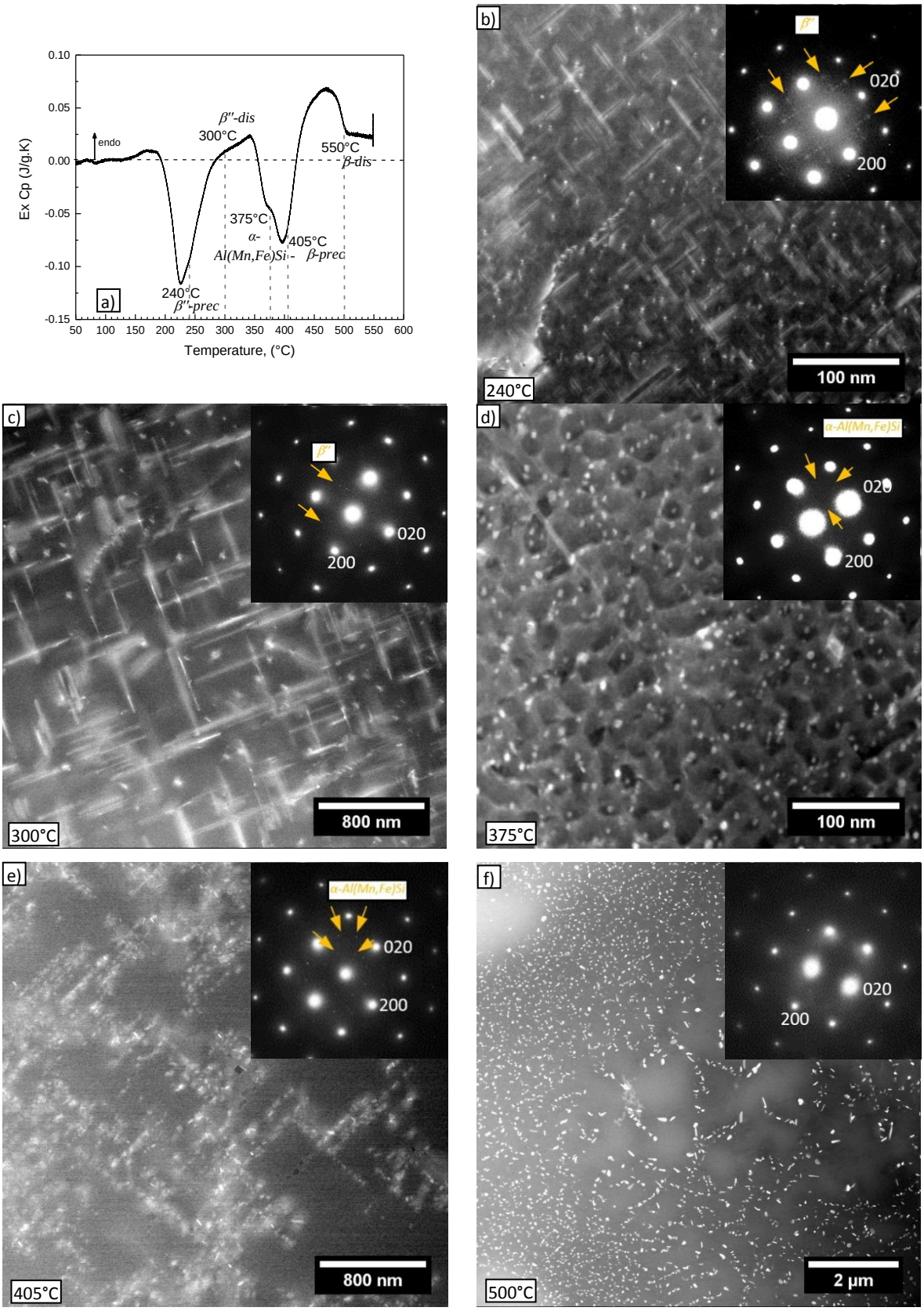

Figure 4.1. (a) The experimental DSC curves of the AA3105 alloy at 0.01 K/s in as-cast condition (Measurement performed by R. H. Kemsies) and (b-f) the dark-field and SAED pattern of the samples, which are quenched at 240, 300, 375, 405 and 500 °C, respectively. (Image acquired by S. Zischke)

Figure 4.2.a shows the experimental DSC curve of the AA3105 aluminum alloy without Mg annealed at a heating rate of 0.01 K/s from the as-cast condition. The STEM and SAED patterns of the quenched samples are shown in Figure 4.2.b-e. At 310 °C, an exothermic reaction signifies that precipitation occurred. It was not possible to observe the diffraction pattern of these precipitates because the volume fraction of the precipitates was too low. This made an identification of the precipitates impossible. The mean radius of the unknown precipitates was 6 ± 1.2 nm. By increasing the temperatures further to 400 °C, an endothermic dissolution reaction of the unidentified precipitates was observed. Simultaneously, precipitation of other precipitates took place. The mean radius of this phase was 16 ± 3.7 nm. The evaluation of SAED patterns showed that these precipitates have a semi-coherent phase boundary with the matrix and according to the calculated d-spacing from its SAED pattern, it was ascertained that the particles corresponded to α-Al(Mn,Fe)Si particles. Li et al. [53] also reported α-Al(Mn,Fe)Si to be partially coherent. At 400 °C, the α-Al(Mn,Fe)Si phase precipitated, and they grew at temperatures from 400 – 460 °C. By increasing the temperature to 500 °C, coarsening and the dissolution of the α-Al(Mn,Fe)Si particles occurred. The mean radius of the α-Al(Mn,Fe)Si particles at 550 °C was equal to 86 ± 36.1 nm. Like in the Mg containing alloy, the α-Al(Mn,Fe)Si particles became entirely incoherent, showing no superstructures. The precipitation sequence of the AA3105 aluminum alloy without Mg can be summarized as: *small precipitates with an unknown structure* → *α-Al(Mn,Fe)Si*. Evidently, the formation of β'' and β' precipitates was not observed.

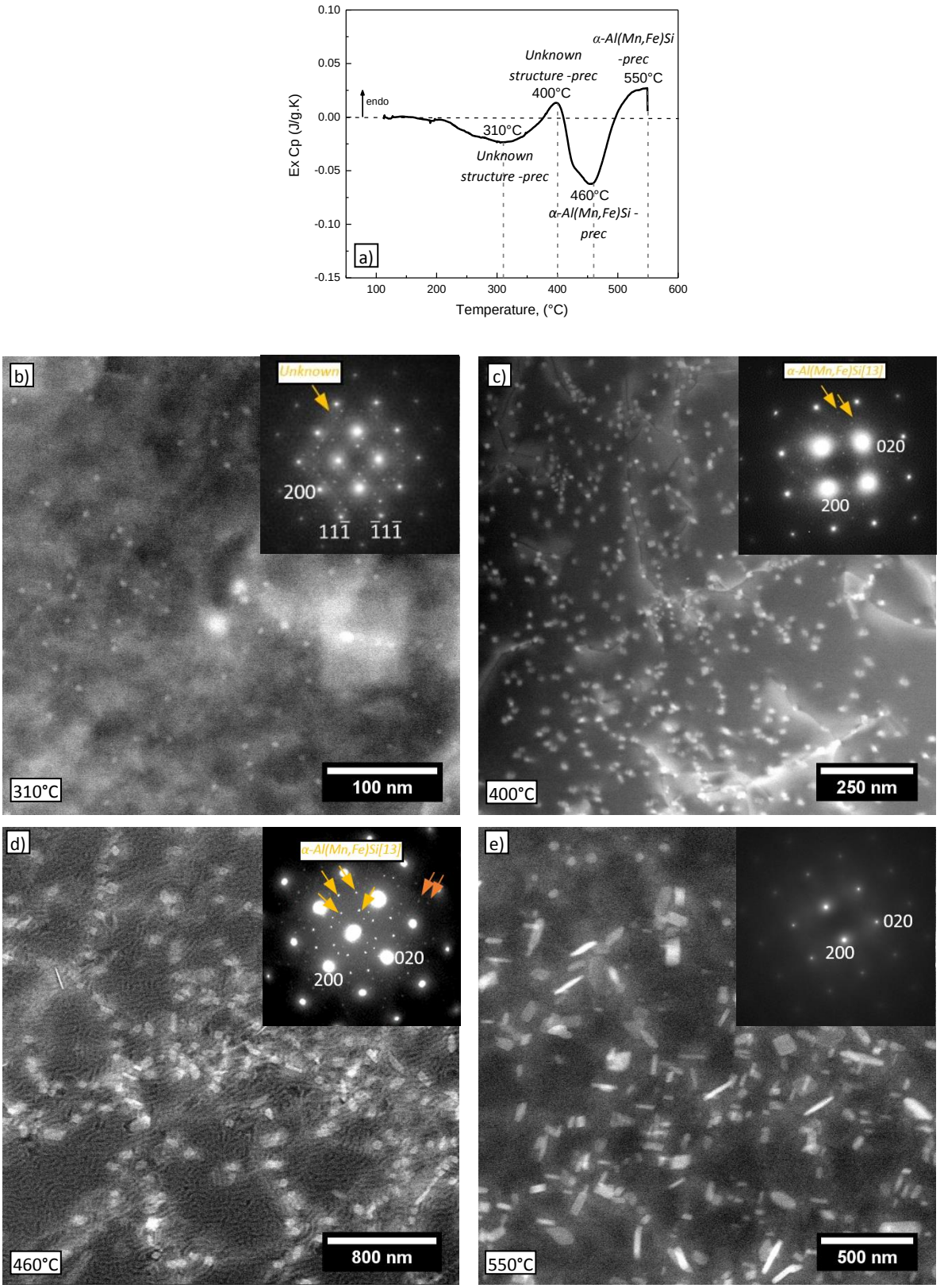

Figure 4.2. (a) experimental DSC curves of the AA3105 alloy with 0.01 K/s in as-cast condition (Measurement performed by R. H. Kemsies) and (b-e) the dark-field and SAED pattern of the samples which are quenched at 310, 400, 460 and 550 °C, respectively. (Measurement performed by S. Zischke)

A comparison of the precipitation sequences shows that the addition of Mg accelerated and shifted the precipitation of the α-Al(Mn,Fe)Si phase to lower temperatures. Lodgaard et al. [164] proposed that a u-phase, which is an unknown phase, precipitate on the surface of the metastable Mg-Si, and the u-phase acts as heterogeneous nucleation sites of the α-Al(Mn,Fe)Si dispersoids, which consume the u-phase entirely. However in this study, nucleation of other nucleus was not observed at metastable Mg-Si phases. The accelerated nucleation of the α-Al(Mn,Fe)Si dispersoids by Mg is therefore attributed to the localized enrichment of the matrix with Mg and Si, in particular due to the dissolution of the metastable phases and the precipitation of stable phases. The stable Mg_2Si phase contains a lower content of Si (higher Mg:Si ratio), which leads to a local enrichment of Si in the matrix during the dissolution of the metastable phases and precipitation of stable phases. It is suggested that these Si enriched sites accelerated the nucleation of the α-Al(Mn,Fe)Si phase. Figure 4.3 shows the TEM dark-field microstructure of the AA3105 alloy after continuous heating to 375 and 405 °C. A few unknown rod-like precipitates were observed in the sample at 375 °C, but the precipitation of α-Al(Mn,Fe)Si dispersoids did not occur at or even near this unknown phase. At 405 °C, no u-phase precipitates were observed in the microstructure.

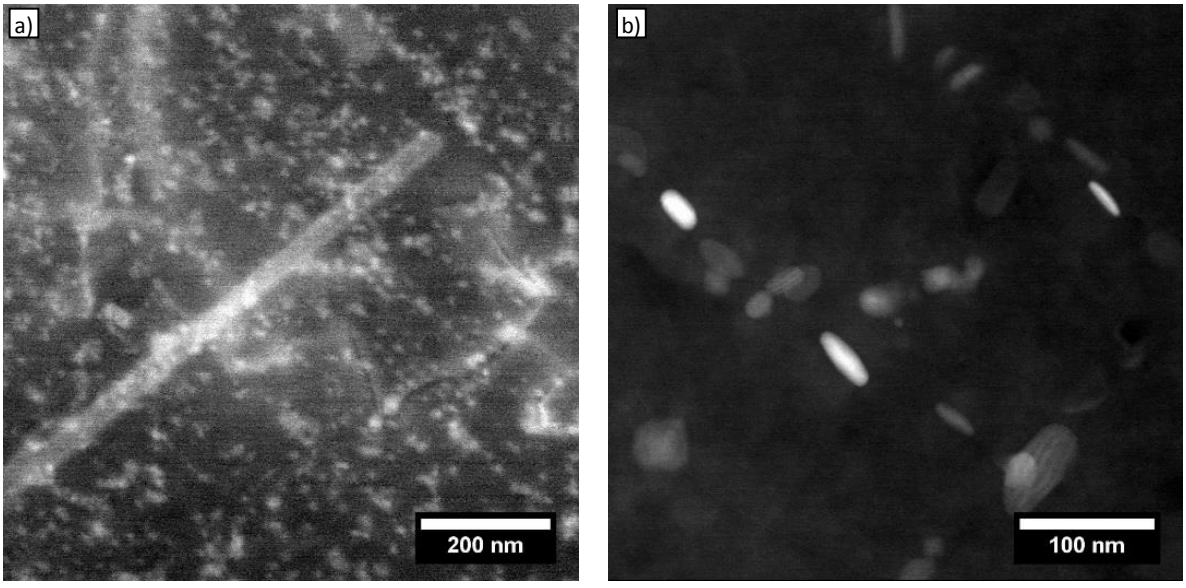

Figure 4.3. TEM dark-field micrograph of the AA3105 alloy after continuous heating to (a) 375 °C and (b) 405 °C. (Image acquired by S. Zischke)

By comparing the size of the unknown particles at around 300 and 400 °C in both conditions, it can be concluded that the particles present in the samples without Mg addition were three

times smaller than those in the Mg-containing AA3105 aluminum alloy. This implies that Mg accelerates the precipitation and growth of these particles, by the localized enrichment of the matrix (assuming they were of the same phase not only at 400 °C, but at 300 °C as well).

4.4 Conclusion

In this study, the precipitation sequences of an as-cast AA3105 aluminum alloy with and without Mg addition were investigated. The TEM investigation shows that the precipitation sequence of the AA3105 aluminum alloy is: (*GP zones)* → β'' → β' → α*-Al(Mn,Fe)Si* → β *(Mg_2Si)*. The precipitation sequence of the AA3105 aluminum alloy without Mg is: *small precipitates with an unknown structure* → α*-Al(Mn,Fe)Si*. The α*-Al(Mn,Fe)Si* is a semi-coherent phase, the precipitation of which is not observed after standard heat treatments and is only detected in the as-cast condition. It was evinced that Mg addition shifts the precipitation temperature of the α-Al(Mn,Fe)Si to lower temperatures. Moreover, the precipitation of Mg-Si particles were not observed by eliminating the Mg content from the matrix. This shows that the precipitation of α-Al(Mn,Fe)Si and Mg-Si particles are parallel processes and the precipitates at low temperature are Mg content precipitates.

5 Optimization of chemical composition and improved precipitation strengthening for elevated temperature applications

5.1 Introduction

In the literature, aluminum alloy optimizations have been mainly confined to the mechanical properties and electrical conductivity. An optimum chemical composition, size and distribution of the dispersoids or precipitates in the matrix of aluminum alloys improves the mechanical properties and electrical conductivity [48], [88], [165]–[168]. The optimization processes were considered for homogenization, recrystallization, age-hardening and alloy composition designs. These optimization processes were based on the experimental investigation or usage of classical nucleation and growth models to define new production processes. These optimization methods were used in automotive manufacturing such as the paint baking processes, structural applications for extruded load-bearing components, electrical applications and welded fuselage panels (e.g. [144], [160], [169]–[173]).

Additionally, precipitation of dispersoids from an as-cast condition was observed during the ageing of AA3xxx alloys, and it was suggested that a significant precipitation strengthening can be achieved through precipitation of partially coherent α-Al(Mn,Fe)Si dispersoids [53]–[57].

The precipitation sequence in the as-cast condition and homogenized condition are not the same in aluminum alloys. One model to calculate the non-equilibrium as-cast condition is the Scheil-calculation. This model determines the phases occurring during a non-equilibrium solidification[78], [174]–[176]. In this model the following assumptions are made. Firstly, diffusion of the solute in the solid is considered negligible whereas the diffusion of the solute in liquid is assumed to be infinitely fast. Moreover, the interface is assumed to be in local equilibrium [2], [174]. In the present work, a Scheil calculation was used to calculate the difference between equilibrium and non-equilibrium solidification. The aim of this study is to determine an optimum heat treatment for the conventional AA3105 and optimized AA3105 aluminum alloys by means of hardness measurement and TEM investigation. The optimized heat treatment should effectuate the maximum contribution of precipitation hardening of α-*Al(Mn,Fe)Si*.

5.2 Experimental procedure

In this study, two different aluminum alloys were produced in an induction furnace. The chemical compositions of the aluminum alloys are shown in the Table 5.1. In each charge, 135 gr molt is preheated to 850 °C in a vacuum chamber and then cast into a cold copper mold or a sand mold. The samples were cut from the ingot and then each heat treated with three different heat treatment paths.

- Path A: An isothermal heat treatment at 250, 275, 325, 350, 375 and 400 °C.
- Path B: A double isothermal heat treatment with a pre-isothermal heat treatment at 185 °C for 6 hours which is followed by the second heat treatment at 325, 350, 375 and 400 °C.
- Path C: A non-isothermal heat treatment with a heating rate of 0.01 K/s from room temperature to the target temperature (350, 375, 400, 425 °C), and a subsequent isothermal heat treatment at the target temperature.

The hardness measurements were conducted by a Wolpert hardness device with a load of 10 Kg.

The SEM images were taken by a Zeiss Leo 1530 FEG (Field emission gun). TEM foils with 3 mm diameter and about 0.8 mm thickness were cut and then ground down to 0.1 mm thickness and then double jet-polished with an electrolytic solution of 30% HNO_3 and 70% Methanol at -30 °C and 15-17 Volts. The TEM foils were imaged in a FEI Tecnai F20, which is equipped with an EDS detector.

Table 5.1. The chemical composition of the commercial and optimized AA3105 aluminum alloy.

Alloy	Fe	Si	Mg	Mn	Cu	Al
Commercial AA3105	0.38	0.5	0.6	0.7	0.145	Balanced
Optimized AA3105	0.88	0.6	0.6	0.7	0.145	Balanced

The amount of solute atoms in the matrix, and clusters or vacancies are microstructure features known to change the electrical conductivity [177]–[179]. In order to estimate if the new optimized AA3105 alloy is comparable in electrical resistivity to the commercial AA3105, the necessary time for 100 nm diffusion distance for Fe atoms were calculated for different

temperatures. The 100 nm distance is assumed to be the maximum distance which is necessary for Fe atoms to reach a particle. Figure 5.1 shows that after 10hours at 325°C, the majority of the Fe solute should have reached the particles.

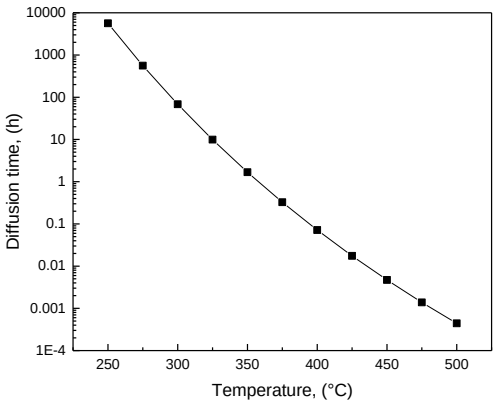

Figure 5.1. Diffusion time vs. Temperature of Fe atoms for 100 nm diffusion distance.

5.3 Results and discussion

5.3.1 Hardness measurements

In order to find the best heat treatment to have the highest contribution of the particles to the precipitation hardening, three different heat treatment paths were introduced. Path A is the conventional heat treatment at constant temperatures and the temperatures are 250, 275, 325, 350, 375 and 400°C. Figure 5.2. a-c shows the hardness results of this path for the commercial and optimized as-cast AA3105 aluminum alloy, which were cast into different molds. Isothermal heat treatments were conducted at 250-425 °C. The samples which were cast into a copper mold had a higher hardness (see Figure 5.2.b). Additionally, the hardness of the optimized AA3105 aluminum alloy increased by decreasing the heat treatment temperatures. The hardness of the conventional AA3105 aluminum alloy, which was cast in a sand mold, was constantly 45 HV10 during isothermal heat treatment and for the optimized AA3105 aluminum alloy after 24 hours heat treatment at 425 °C was also 45 HV10, which was considered as the lowest hardness of the material. However by remelting the same samples and casting them into the cold copper mold, the material becomes age hardenable from the as-cast condition and the maximum hardness was found to be 64 HV10 after 15 hours of isothermal heat treatment at 250 °C (see Figure 5.2.b). Figure 5.2.c shows that the maximum hardness of the newly designed alloy is 76 HV10 after 10 hours isothermal heat treatment at

250 °C. It is also important to mention that at 250 °C, 3 different peaks at 2, 10 and 20 hours are observed. The peaks could be attributed to the Mg-Si particles and *α-Al(Mn,Fe)Si* particles as described previously in section 4. In order to understand which phase has the highest contribution to the precipitation hardening, TEM investigations were conducted. Three samples were quenched after heat treatment for 2, 10 and 20 hours at 250 °C. Figure 5.3 shows the conventional TEM image and diffraction pattern of the optimized AA3105 cast in a copper mold after 10 and 20 hours heat treatment at 250 °C and quenching to room temperature. An overlap of diffraction patterns of the precipitates on the matrix diffracted pattern cannot be observed along lines [010]Al and [100]Al. However, in chapter 4, the precipitation sequence of AA3105 aluminum alloy had been determined. By comparing the morphology of the particles, the two peaks indicated in Figure 5.2 with arrows were attributed to the formation of the β'' and β' precipitates.

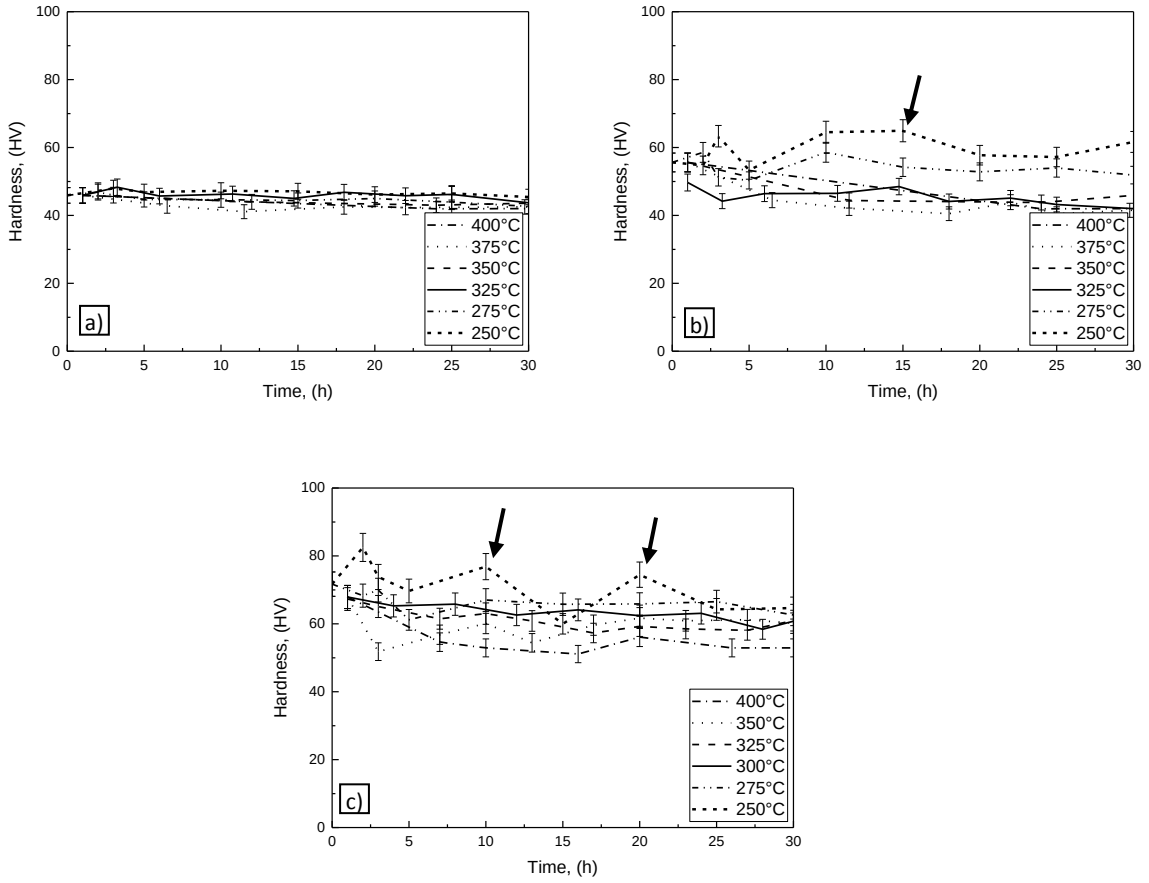

Figure 5.2. The hardness results of the commercial AA3105 alloy in an as-cast condition with heat treatment path A, (a) cast in a sand mold, (b) cast in a copper mold; (c) optimized AA3105 in a copper mold.

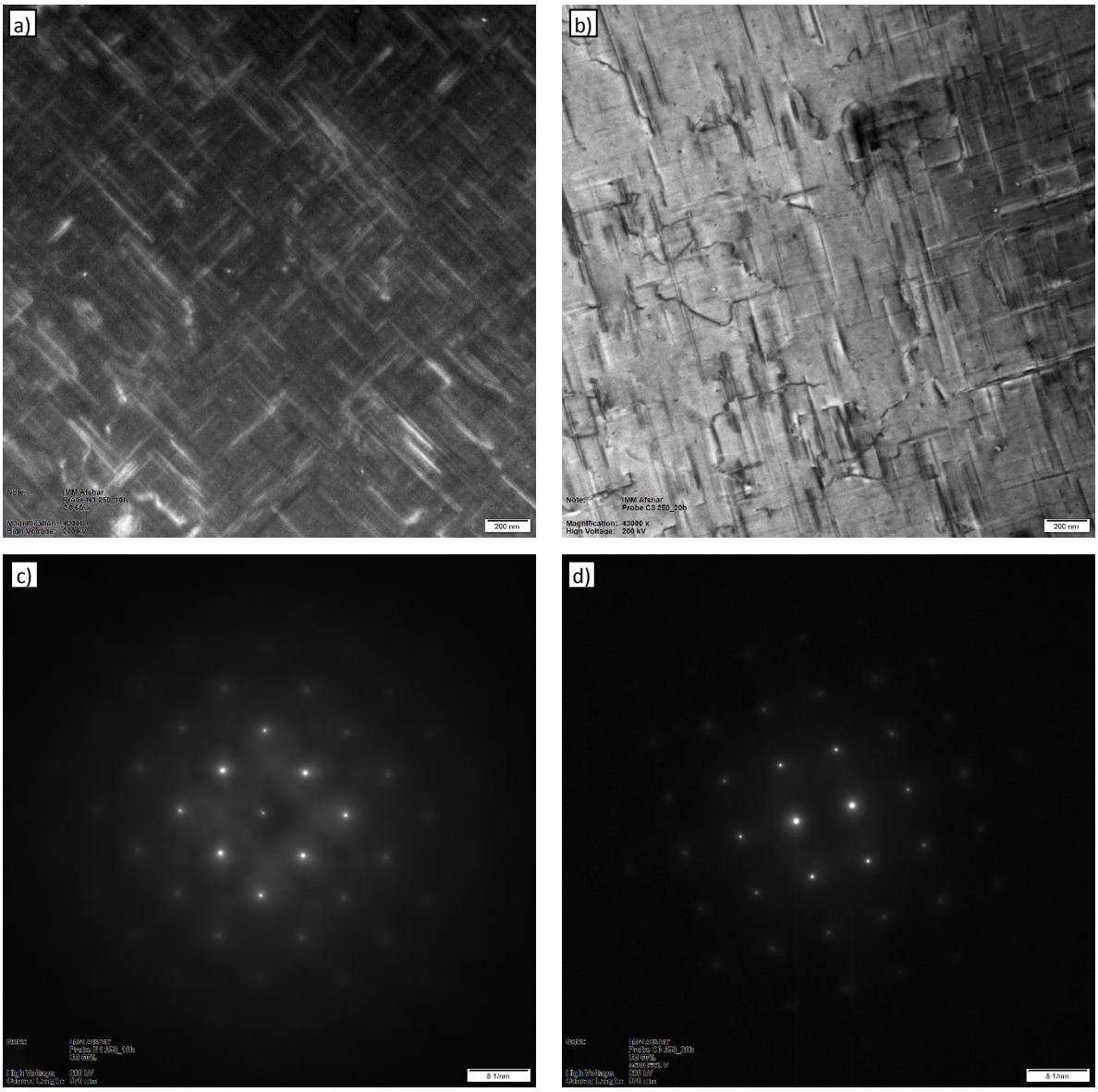

Figure 5.3. (a,b) The conventional TEM image and (c,d) diffraction pattern of the optimized AA3105 in a copper mold which are quenched at 250 °C after (a,c) 10 hours and (b,d) 20 hours, respectively. Specific diffraction pattern were not recognized but the morphology of the particles suggests that they are β'' and β' precipitates. (TEM performed by S. Zischke)

Figure 5.4.a and b show the hardness results of the commercial and optimized AA3105 aluminum alloy which were heat treated according to the second path, B (Figure 5.4.c). The results show that the hardness of the samples had increased to 72 HV10 for the commercial AA3105 aluminum alloy (see double arrow on Figure 5.4.a) and 97HV for the optimized AA3105 aluminum alloy after isothermal heat treatment at 180 °C for 6 hours (see double arrow on Figure 5.4.b). Any further heat treatment at higher temperatures led to a drastic drop of the hardness. Thereafter the hardness results remained constant. For the

conventional AA3105 aluminum alloy the maximum hardness after second heat treatment is 52 HV10, which was obtained by a heat treatment at 425 °C for 4 hours (see solid arrow on Figure 5.4.a), while the maximum hardness was achieved for the optimized AA3105 aluminum alloy 63HV after 2 hours for the same temperature (see solid arrow on Figure 5.4.b).

The increase of the hardness reached in the first part of heat treatment was attributed to the precipitation of the Mg-Si particles at 185 °C, which was same as with a peak aging heat treatment [87], [179]. After heat treatment the hardness drops, because the particles were either dissolved or they got larger and their interface became incoherent during Ostwald ripening. It was expected that the precipitation of the α-*Al(Mn,Fe)Si* particles contributed to precipitation hardening, but this was not observed. However, the hardness was more than 45 HV. Probably the precipitation of the α-*Al(Mn,Fe)Si* particles is not uniformly distributed, and their sizes are not small enough to increase the hardness significantly.

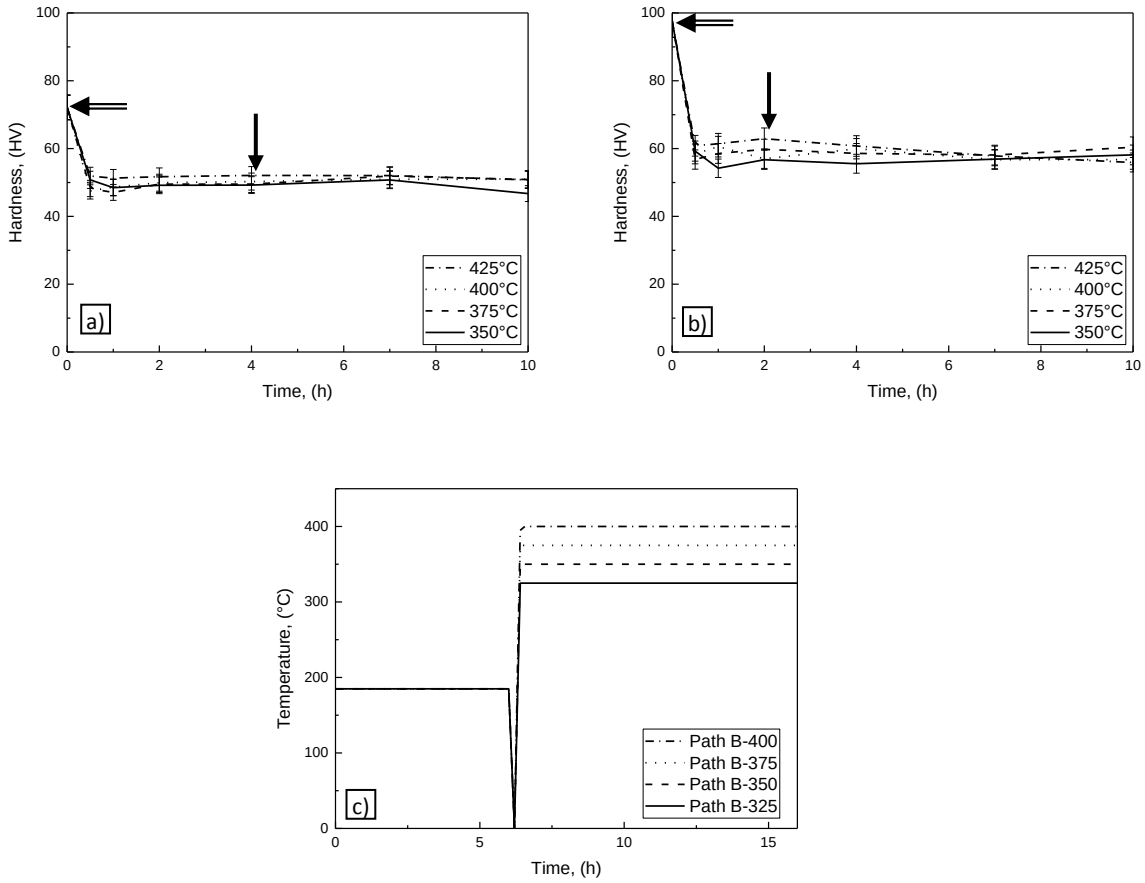

Figure 5.4. The hardness results (a) of the commercial AA3105 alloy in an as-cast condition in a sand mold, (b) of the optimized AA3105 in a copper mold with path B and (c) The heat treatment path B.

Figure 5.5 a and b show the hardness change of the samples which are heat treated according to path C (Figure 5.5 c). The hardness of the commercial AA3105 aluminum alloy was between 45-58 HV10, and the maximum was achieved after 5 hours heat treatment at 400 °C (See Figure 5.5.a). The hardness of the optimized AA3105 aluminum alloy was higher compared to the commercial AA3105 aluminum alloy, and the maximum hardness is 65.5 HV10 for the sample which was heat treated at 400 °C for 3 hours. For all the samples which were heat treated at temperatures higher than 350 °C, the increased hardness must be due to the α-$Al(Mn,Fe)Si$ particles, because all other particles are either dissolved or too large. This indicates that, as was aspired, these alloys can be used for high temperature applications.

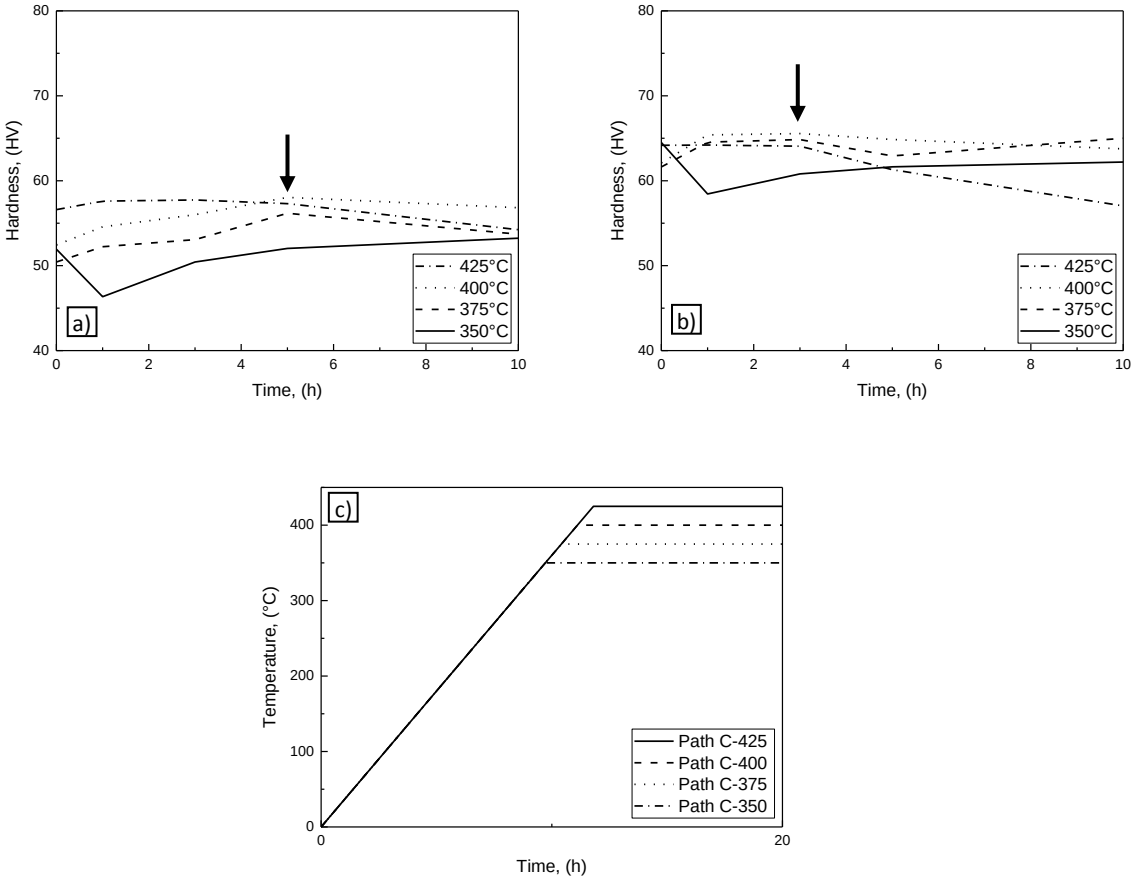

Figure 5.5. The hardness results (a) of the commercial AA3105 alloy in an as-cast condition in a sand mold, (b) of the optimized AA3105 in a copper mold with path C and (c) The heat treatment path C.

The comparison of the three different paths shows that the achieved hardness through the path A was higher for the samples which were cast into a copper mold than other paths. However for the samples which were cast into sand mold, the path C was also an alternative

which has improved the mechanical properties significantly. The path B did not show a significant improvement in the hardness.

The highest hardness was achieved by path C from the optimized AA3105 aluminum alloy, which makes this alloy a good alternative for high temperature applications.

5.4 Conclusion

In this study, the precipitation hardening of an as-cast commercial and optimized AA3105 aluminum alloy were investigated. The hardness measurements showed that the maximum achieved hardness was equal to 76 HV10, which was achieved after a heat treatment of the optimized AA3105 aluminum alloy according to path A for 10 hours at 250 °C. The TEM investigations proved that the Mg-Si particles had the highest contribution to the hardness in this samples. For the commercial AA3105 aluminum alloy, the maximum hardness of 58 HV10 was achieved after a heat treatment according to the path C for 5 hours at 400 °C. For high temperature applications, the optimized AA3105 aluminum alloy after ramp had the highest hardness at 400 °C after 1 hour, which was 65.5 HV. This hardness is the highest one achieved by the precipitation of the α-Al(Mn,Fe)Si particles. These particles are stable at the application temperature and the optimized AA3105 aluminum alloy can be considered as a high creep resistance aluminum alloy at this temperature. The new optimized AA3105 alloy is comparable in electrical resistivity to the commercial AA3105.

6 Creep behavior of AA3105 and Al-Zr-Fe aluminum alloys

6.1 Introduction

Creep refers to a permanent deformation of a material that occurs over time at high temperatures under a constant stress. As has been mentioned in chapter 2, creep has been observed in all metals at temperatures higher than 0.3 of the homologous melting temperature [96]. Precipitation hardening, solid solution hardening, increasing grain diameter and introducing preferred texture are the most important methods to improve creep resistance. The aim of using these methods is to prevent all possible mechanisms of creep at the same time. This means that the fast diffusion paths (like in grain boundaries) need to be avoided, and the strength must be improved by solid solution and particle hardening. The latter mechanism needs to prevent both slip and climb of dislocations.

Electrical conductivity in alloys decreases with increasing the alloying content in the matrix [2], [52]. Recently, Liu et al. reported that precipitation of dispersoids in an as-cast AA3004 alloy improved the mechanical properties and also electrical conductivity. Dispersion hardening is also a useful method to increase the creep resistance and also to increase the electrical conductivity [51], [52].

The aim of this study is to determine the dominant creep mechanism of the commercial AA3105 aluminum alloy and an Al-Fe-Zr alloy. Conventional tensile creep test were conducted, and creep samples were investigated by means of SEM and TEM.

6.2 Experimental procedure

The chemical composition of the extruded alloys is listed in Table 6.1. The TEM investigation method is explained in section 4.2.

Table 6.1. The chemical composition of the extruded aluminum alloy.

Alloy	Si(wt.%)	Fe(wt.%)	Cu(wt.%)	Mn(wt.%)	Mg(wt.%)	Zr(wt.%)	Al
AA3105	0.48	0.38	0.145	0.7	0.6	0	balanced
Al-Fe-Zr	-	0.1	-	-	-	0.15	balanced

Tensile tests and creep tests were conducted with a DZM machine at room and elevated temperatures. Before each test, the samples were kept for 15 minutes to have a homogenous temperature distribution. Figure 6.1 shows the dimensions of the tensile test specimens. The

creep tests were conducted in the application temperature range 373K – 473K (100 - 200 °C), which corresponds to $0.399 < T/T_m < 0.5$. The tensile stresses were in the range 30 - 100 MPa.

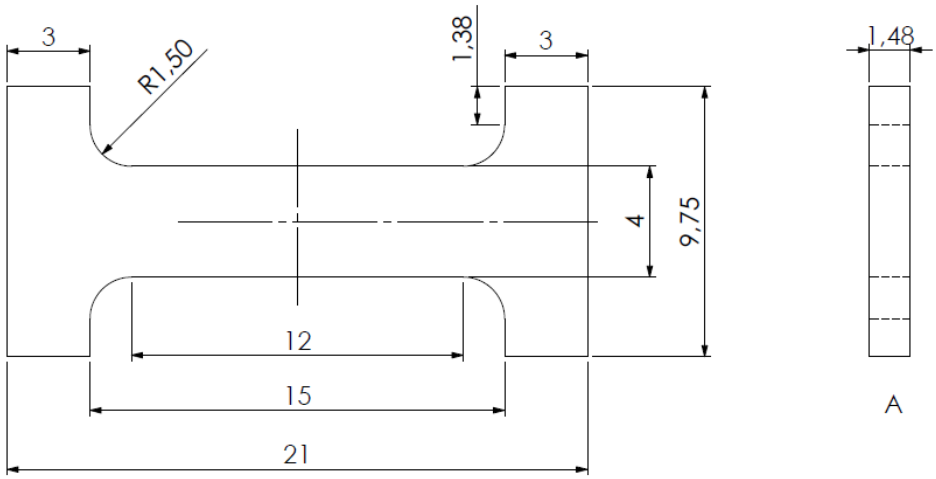

Figure 6.1. Geometry of the tensile samples in units of mm.

The TEM samples were also examined by utilizing a cross beam XB 1540 FIB instrument (Carl Zeiss SMT AG, Germany) with EDAX detector [180]. The SEM was operated at 20 KV accelerating voltage and beam current is 2.7 nA by S.J. Schröders. During EBSD data acquisition, exposure time was 0.03 s, pixel binning was 96 × 96 pixels and step-size was 0.25 µm.

6.2.1 Sample preparation for AA3105 aluminum alloy

Figure 6.2. shows a high resolution high-angle annular dark-field (HAADF) STEM image of the extruded AA3105 aluminum alloy. Brightness in a HAADF image shows the atomic number contrast [181]–[183]. The TEM micrographs show that two different precipitates are present in the matrix. Figure 6.2.b shows an EDS line scan on two precipitates which are close to each other. The EDS measurement demonstrates that one of the precipitates corresponded to a Mg_2Si particles whereas the other to an α-Al(Fe,Mn)Si. At temperatures above 100 °C, the Mg-Si particles cannot improve the creep resistance over a long time span, because the Mg and Si elements diffuse fast enough to encourage growth and coarsening of the Mg-Si particles. Figure 6.3.a shows the metastable Mg-Si particles in samples which were kept for 1000 hours at 140 °C, and Figure 6.3.b shows the SAED pattern of the same area. The precipitates were the needle-like β” precipitates. This was verified by comparing the SAED pattern with the

patterns found in the literature [30], [162], and these metastable particles in the matrix are not stable and can grow further. In order to eliminate the Mg-Si particle contribution to the strength, the samples were heat treated at 300 °C for 24 hours, which lead to the precipitation of Mg_2Si particles, which are so coarse that their contribution is negligible. This condition was considered as the initial condition of the AA3105 aluminum alloy.

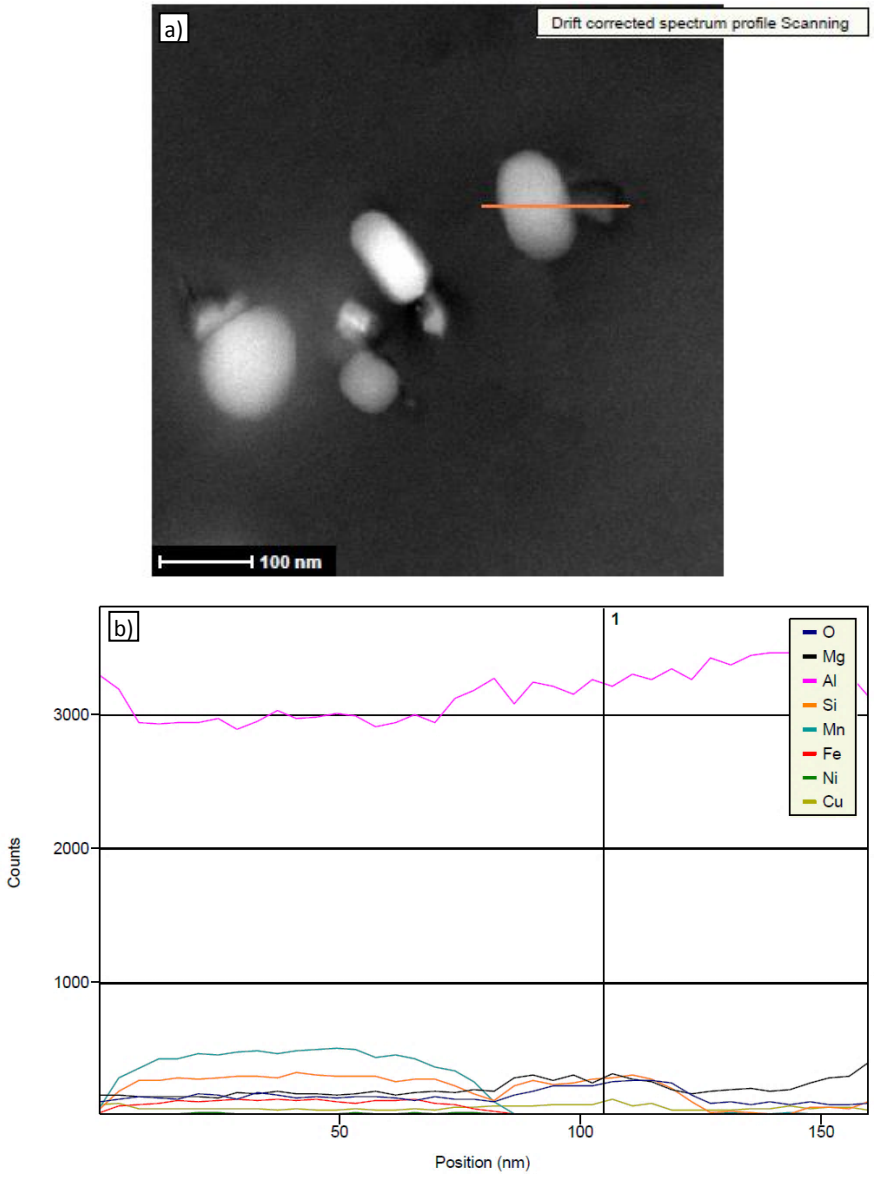

Figure 6.2. (a) HAADF image and (b) Line scan of X-ray spectrum of a dispersed particles. The main elements are: Al, Si, Mn, Mg and Fe. (TEM performed by S. Zischke)

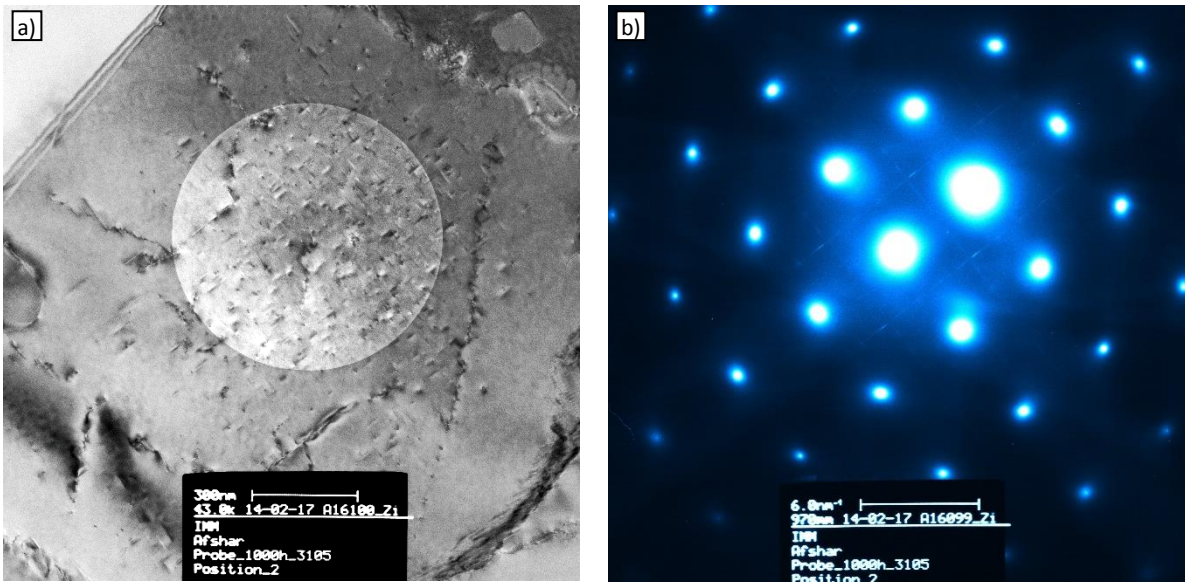

Figure 6.3. (a) The conventional TEM micrograph and (b) the SAED pattern of the same area of the heat treated sample at 140 °C for 1000 hours. (Image acquired by S. Zischke)

6.2.2 Sample preparation for Al-Zr-Fe aluminum alloy

The initial condition of Al-Zr-Fe aluminum alloy is the as-extruded sample, with an extrusion at a temperature of 480°C, after 3 hours of homogenization at 600°C.

6.3 Results of AA3105 aluminum alloy

6.3.1 Creep tests

The tensile creep tests were carried out at different temperatures ranging from 100 °C to 200 °C (373K – 473K) under different applied stresses. Figure 6.4 shows the creep curves, which are expressed as true strain against dwell time. Increasing the temperature activated different deformation mechanisms and accelerated the deformation. Therefore, the true strain increased under a constant stress with increasing temperature, and it increased by increasing the stress at a constant temperature.

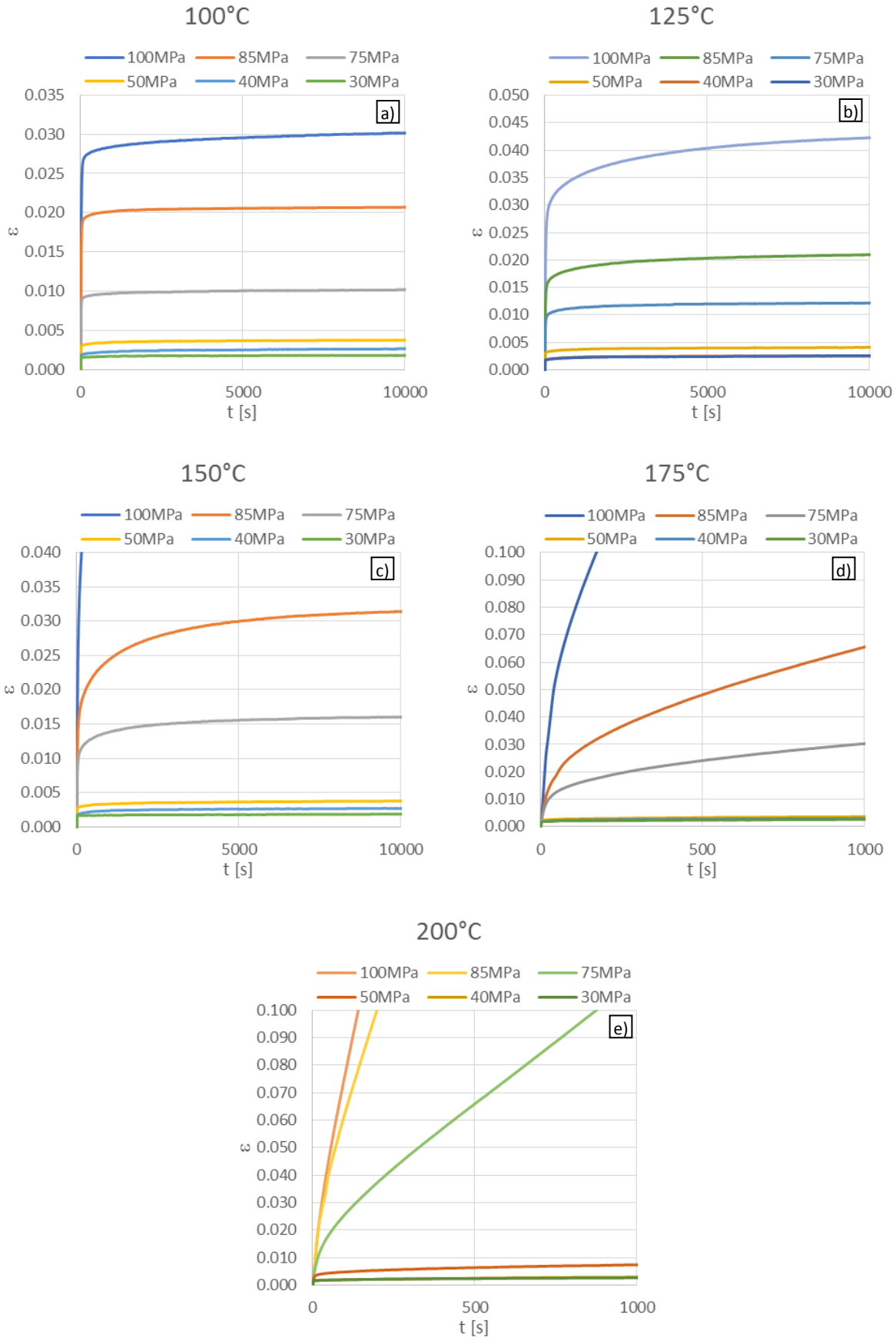

Figure 6.4. Creep strain over time for the AA3105 aluminum at different temperatures.

In order to define the dominant creep mechanism at a condition in which the steady-state creep rate is too short, the minimum creep rates were assumed to be the steady-state creep rate.

Eq. 26 describes that the steady creep rate depends on stress and temperature in a wide range of strain rates. The shear modulus depends on temperature [184]–[186] and the following equation was used to consider temperature dependence of the shear modulus of the material [186]:

$$G(MPa) = G_0 - G_T T \qquad \text{Eq. 53}$$

where G_0 is 3.022×10^4 MPa and G_T is the variation of the shear modulus per degree Kelvin and is equal to 16.0 MPa.K^{-1}. Figure 6.6 shows the minimum creep rates in the Arrhenius diagram. According to the activation energies, three different regimes are recognized, one low temperature regime and two high temperature regimes. At low temperatures the average activation energy is 15.3 kJ/mole; at high temperatures and low stresses, the average activation energy is 89.3 kJ/mole, and at high stresses it is around 174.9 kJ/mole.

In order to calculate the stress exponent, on a double logarithmic scale the minimum creep rates were plotted against normalized stress (see Figure 6.7). Based on the creep exponents, two distinct regimes are observed at low and high stresses. In the lower stress regime, the stress exponent is in the range of 2-3 and at higher stress is in the range of 9-11. High stress exponents indicate the presence of a threshold stress [187]. The threshold stress (σ_{th}) was determined by plotting the strain rate raised to the power 1/n ($\dot{\varepsilon}^{1/n}$) as function of stress at different temperatures, following the procedure of Ref. [188]. The threshold stresses were in the range of 28-45 MPa and decreased with increasing the temperature. Figure 6.5 shows the strain rate raised to the power 1/n as a function of stress at 200 °C. By considering the results of all the temperatures, it was found that the stress exponent of 5 yields the best linear fit between $\dot{\varepsilon}^{1/n}$ vs σ. The threshold stresses were determined for all the temperatures. Figure 6.5.b shows the threshold stress as a function of reciprocal absolute temperature. The results show that the experimental value of the threshold is temperature dependent and is represented by the following equation [188]:

$$\frac{\tau_{th}}{G} = B_0 \exp\left(\frac{Q_0}{RT}\right) \quad \text{Eq. 54}$$

Here, Q_0 is an activation energy and B_0 is a constant. The fitted Q_0 is 6.410 kJ/mole, which was determined from Figure 6.5.b. The results are consistent with literature [189].

Additionally, a comparison is made between the calculated threshold stress in this work and the predicted results from various models proposed for dispersion hardened alloys in the literature [125], [189]–[195]. Figure 6.5.b shows the temperature dependency is compared to the Orowan, climb and threshold stresses from different models. In the calculations, the average planar spacing is approximately 400 nm and the average particle size is 150 nm. The results show that the experimental results are consistent with the predictions.

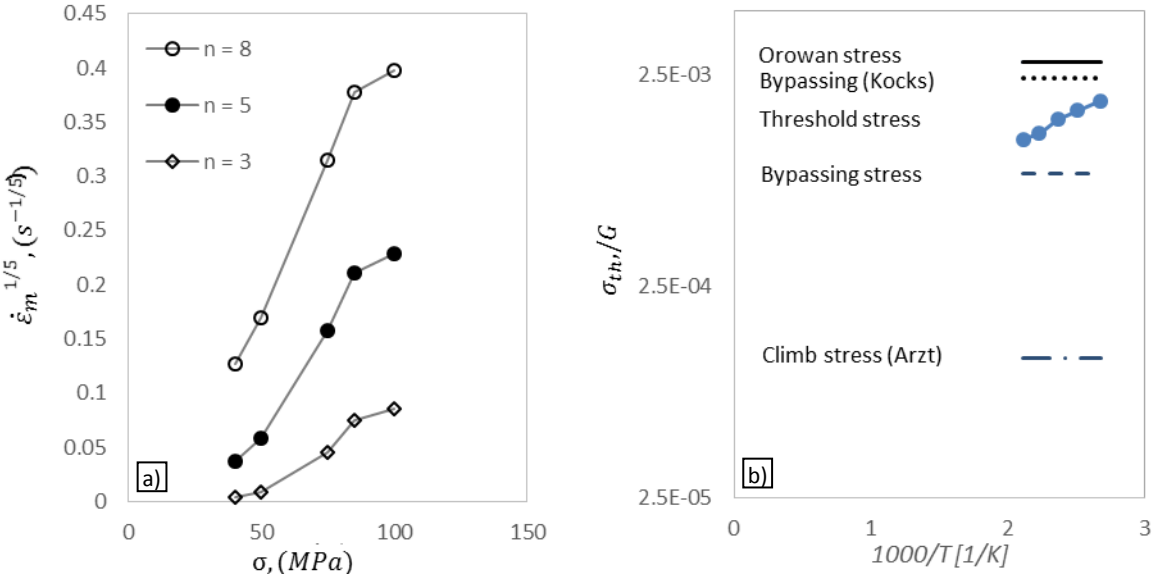

Figure 6.5. (a) The strain rate raised to the power 1/n as a function of stress at 200 °C. b) the comparison between temperature dependence of normalized threshold stress and those predicted from various models proposed for dispersion hardened alloys [188].

The mentioned data were used to determine the stress exponent based on Eq.27. At higher stresses, the stress exponents were from 5 to 6 and at low stresses was in the range of 0.5-1.0 (see Figure 6.7)

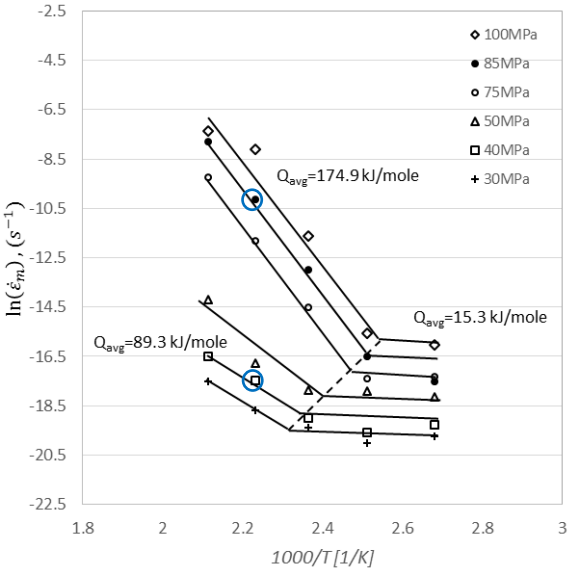

Figure 6.6. The minimum creep rates vs. reciprocal temperature at different stresses for AA3105 aluminum alloy.

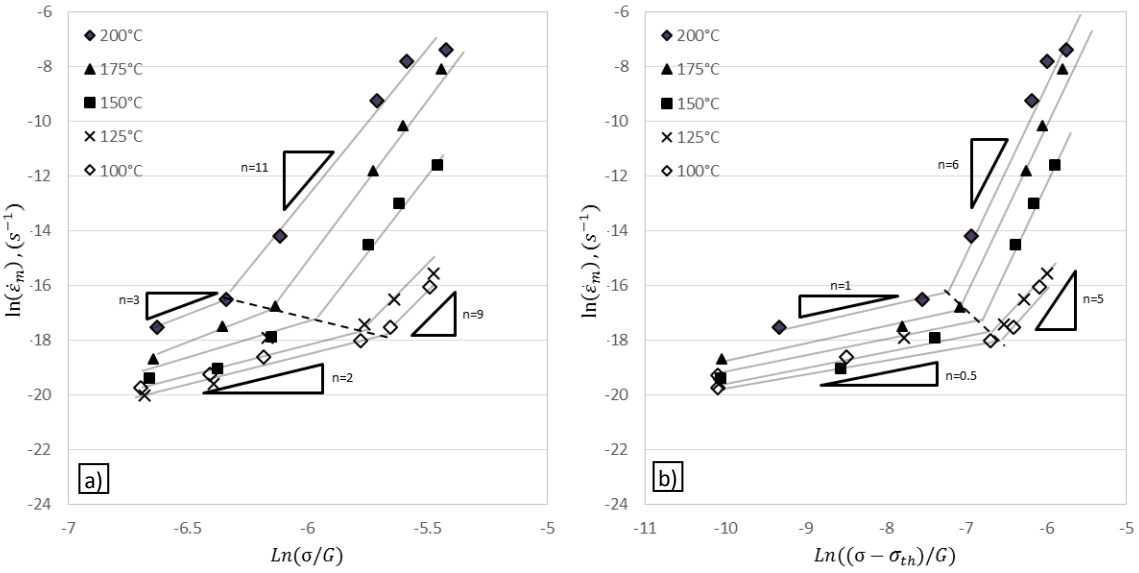

Figure 6.7. The minimum creep rates vs. normalized stress at different temperatures a) without considering the threshold stress and b) with considering threshold stress for AA3105 aluminum alloy.

6.3.2 Microstructure observation

It is generally accepted that in extruded samples, grains are elongated. This was also observed in the present SEM micrographs. Figure 6.8.a shows the Inverse Pole Figure (IPF) map of the extruded AA3105 aluminum alloy. The IPF map shows the orientation of the grain boundaries. The IPF verified that the microstructure was completely recrystallized and the grains were

elongated and had a preferred orientation. Figure 6.8.b shows the grain boundary misorientation distribution in 25 grains. Around 45% of all the grain boundaries were low angle grain boundaries (<15°). Figure 6.8.c and d present TEM micrographs of the extruded AA3105 aluminum alloy. Figure 6.8.d shows same dislocations in the aluminum matrix at a higher resolution. Dislocation forests and pile-ups were not observed. α-Al(Fe,Mn)Si particles were randomly distributed in the matrix, and primary precipitates were observed at grain boundaries.

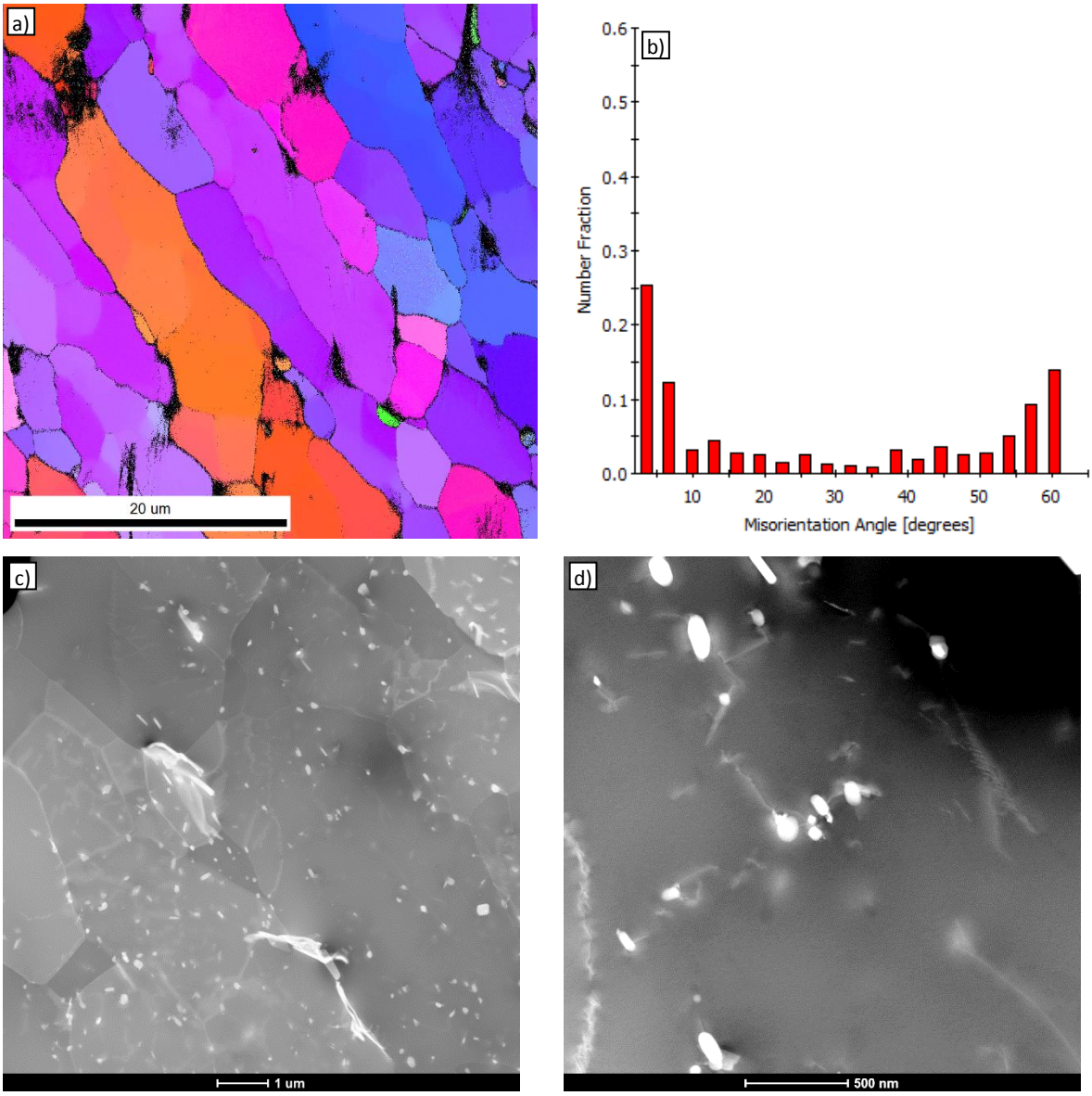

Figure 6.8. (a) The EBSD map, (b) histogram of the misorientation angle from 2-65° and (c-d) TEM dark-field micrograph of the extruded AA3105 aluminum alloy in the initial condition. (SEM performed by S.J. Schröders)

Figure 6.9 shows the TEM dark-field image of the AA3105 aluminum alloys after creep at 175 °C under different stresses and different creep times. The samples were taken from samples which were deformed up to around 80% of fracture strain and were both in the steady state area. Comparing the images reveals that the crept sample under 40 MPa had a lower dislocation density. Arrows show the high dislocation density in the crept sample under 85 MPa stresses. Additionally, a brightness change of the matrix within a grain was observed at higher stress which indicates that a high amount of the geometrically necessary dislocation (GND) were formed in the matrix. The GNDs are responsible for the orientation variation within grains[196]–[198]. Due to the orientation of the grains, an observation of the dislocations was not possible in all of the grains.

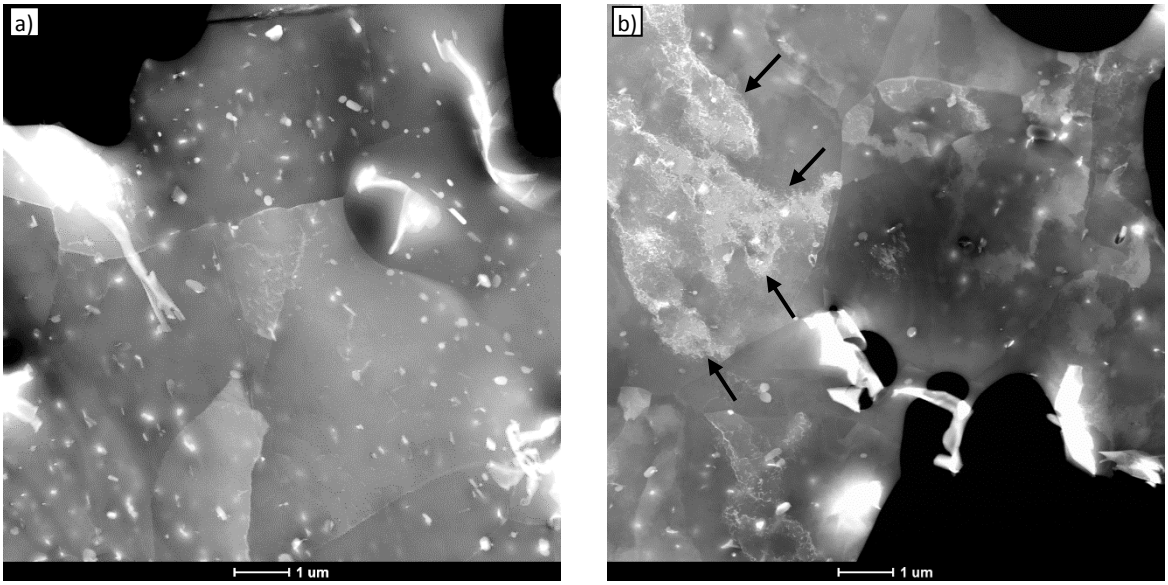

Figure 6.9. TEM dark-field micrographs of the crept AA3105 aluminum alloy (a) under 40 MPa after 14 hours and (b) 85 MPa after 2 hours at 175 °C. The arrows show areas with high dislocation density. (TEM performed by S. Zischke)

Figure 6.10 shows the microstructure evolution of the samples after 1 and 14 hours under 40 MPa. Figure 6.10.b shows a dislocation pile-up and also dislocation dipoles (see arrows). By passing the time, recovery processes were activated and dislocation annihilation has occurred locally. Low angle grain boundaries were formed. Still, comparing the Figure 6.10.a and c shows that the dislocation density has increased over time as a result of creep (see arrows on Figure 6.10.c). Additionally, at high temperature, dislocation cell walls were observed, which indicates the dislocations were rearranged and new subgrains were formed (see arrows on Figure 6.10.c). Figure 6.11 shows the kernel average misorientation maps (KAM) of the same

samples [196], [198]. The KAM maps show that the dislocation density has not increased drastically but the amount of the areas which had low confidence index (black areas) [199]–[201], has also increased, which shows that the dislocation density has increased locally. Additionally, Figure 6.11.c and d show that the fraction of the low angle grain boundaries with misorientation angle less than 8° decreased over time, compared to the low angle grain boundaries with a misorientation angle of more than 8°. This shows that the dislocations were recovered at grain boundaries and high angle grain boundaries were formed.

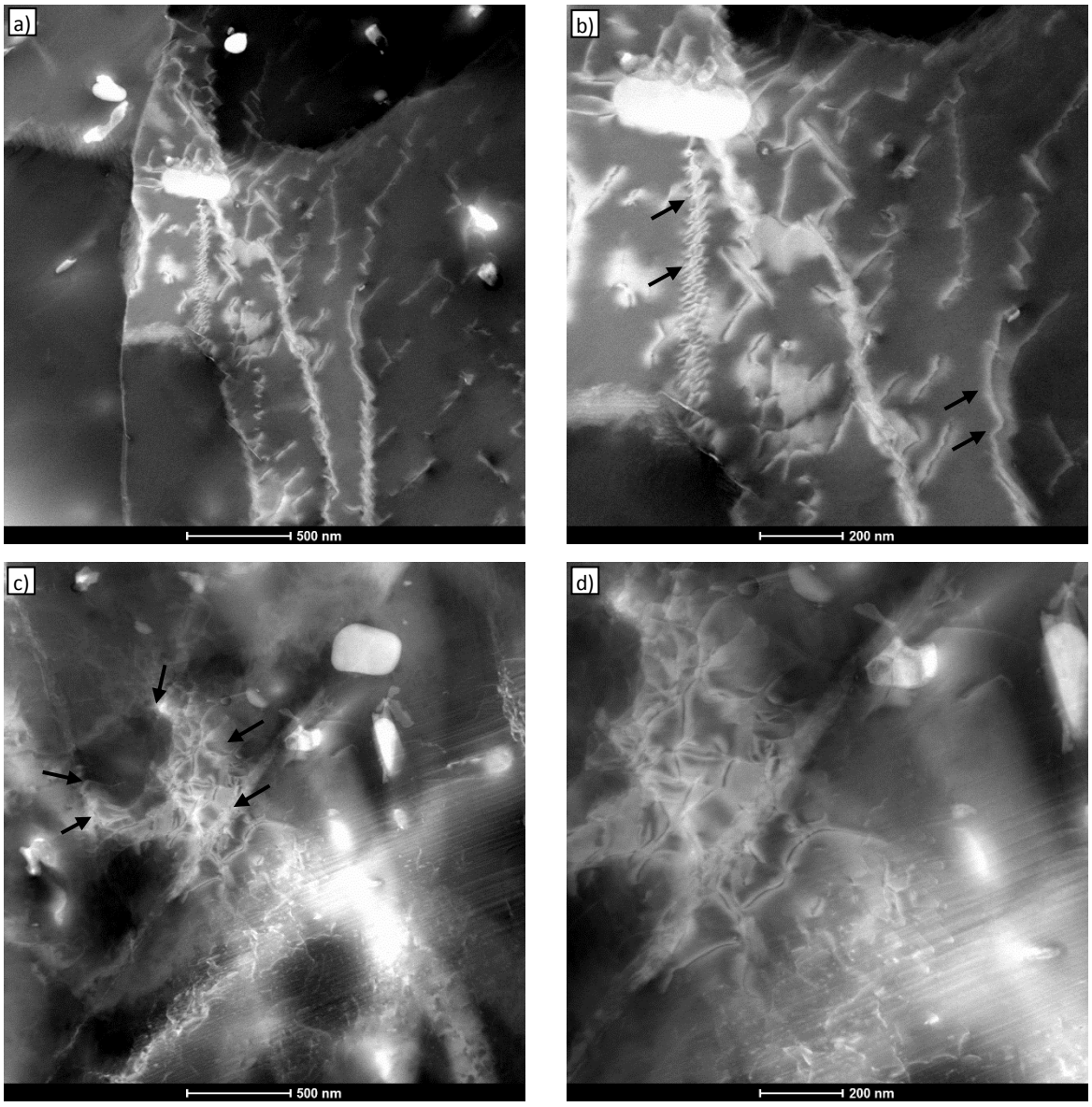

Figure 6.10. TEM dark-field micrograph of the crept AA3105 aluminum alloy under 40 MPa (a-b) after 1 h and (c-d) after 14 h at 175 °C. The arrows show dislocation pile-up and also dislocation dipoles. (Image acquired by S. Zischke)

Figure 6.12 shows the dark field image of the AA3105 aluminum alloy after 25 mins and 2 hours under 85 MPa tensile stress. Figure 6.12.a and b show the dislocations pile-up behind a precipitate (see arrows on Figure 6.12.b). Figure 6.12.c and d show that, compared to the 40 MPa samples, a higher amount of dislocations are produced. They have formed smaller subgrains even though the time periods were shorter compared to the 40 MPa samples. Arrows on Figure 6.12.c show a few low angle tilt subgrain boundaries, which were made of a set of edge dislocations. The dislocation density was low after 25 mins but over time, the amount of dislocations had increased drastically.

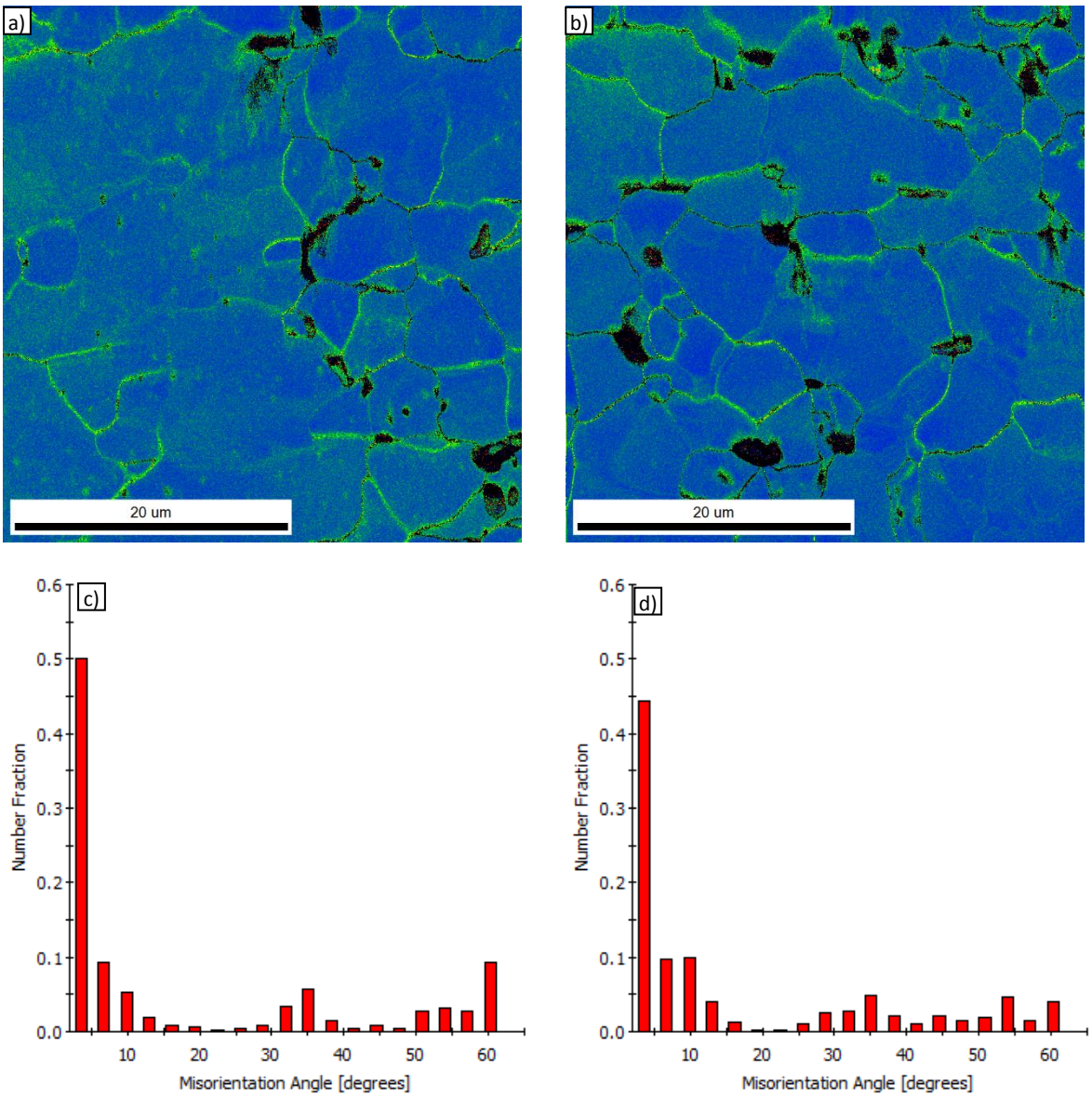

Figure 6.11. (a-b) Kernel average misorientation angle maps and (c-d) histograms of the misorientation angle from 2-65° of the crept AA3105 aluminum alloy at 175 °C under 40 MPa after (a,c) 1 h and (b,d) 14 h. (SEM performed by S.J. Schröders)

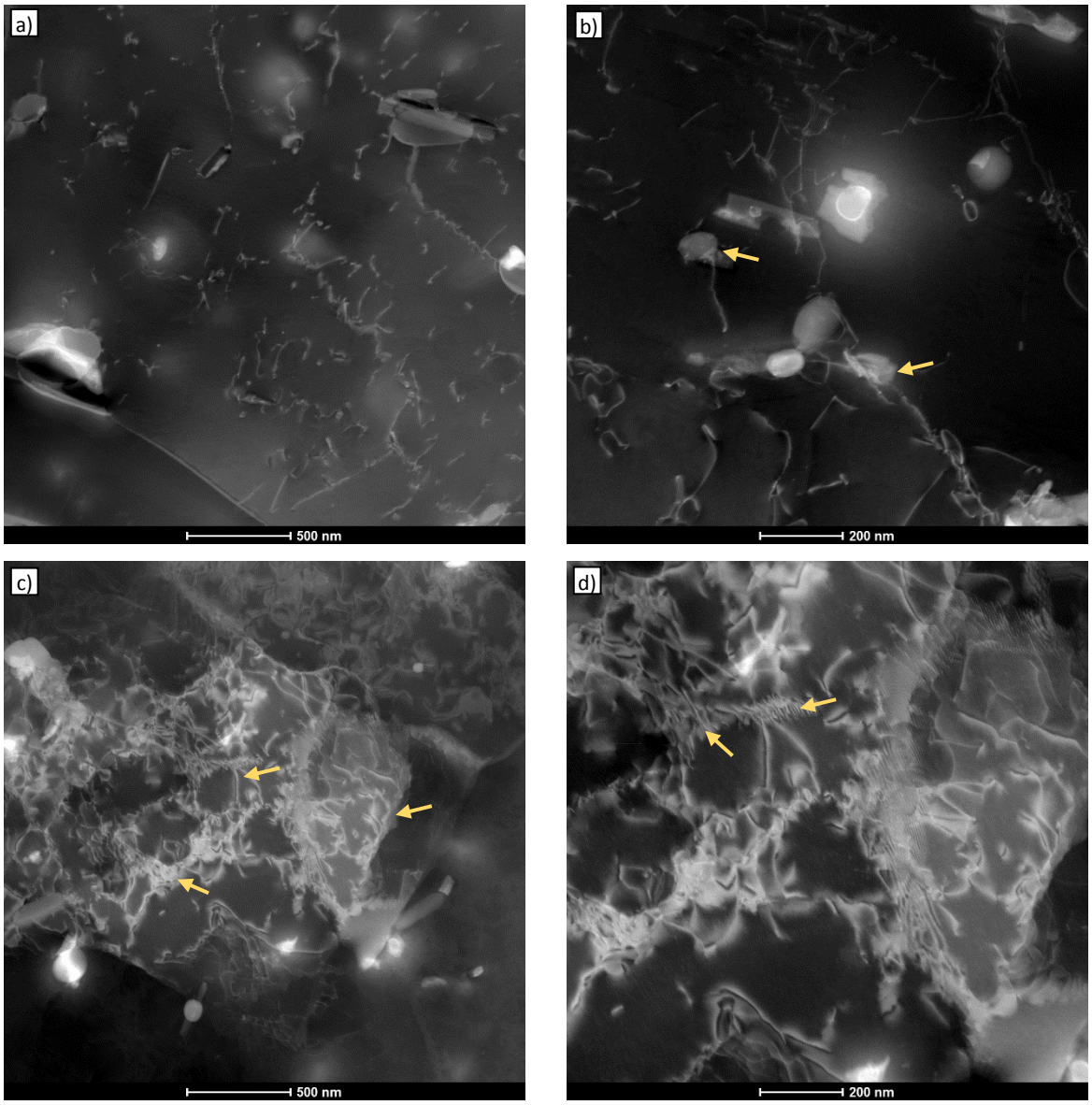

Figure 6.12. TEM dark-field micrographs of the crept AA3105 aluminum alloy at 175 °C under 85 MPa after (a,b) 25 mins and (c,d) 2 h. The arrows show dislocations pile-up behind a precipitate and a subgrain formation. (Image acquired by S. Zischke)

Additionally, in some areas the dislocations had enough time to annihilate, which lead to higher misorientation angles at grain boundaries compared to the samples which were crept under 40 MPa.

Figure 6.13 shows the KAM maps of the AA3105 aluminum alloy tested under 85 MPa after 25 mins and 2 h. The KAM maps show that the dislocation density increased drastically compared to the low stresses (More green areas). Also the amount of the area with a low confidence index increased, which also verified that the dislocation density has increased

locally (More black areas). Additionally, Figure 6.13.c and d show that the fraction of the low angle subgrain boundaries (less than 8°) compared to the initial condition has increased. Additionally, compared to the low angle grain boundaries with a misorientation angle more than 8°, the amount of the low angle grain boundaries increased. It shows that the dislocations were annihilated at grain boundaries and high angle grain boundaries were formed.

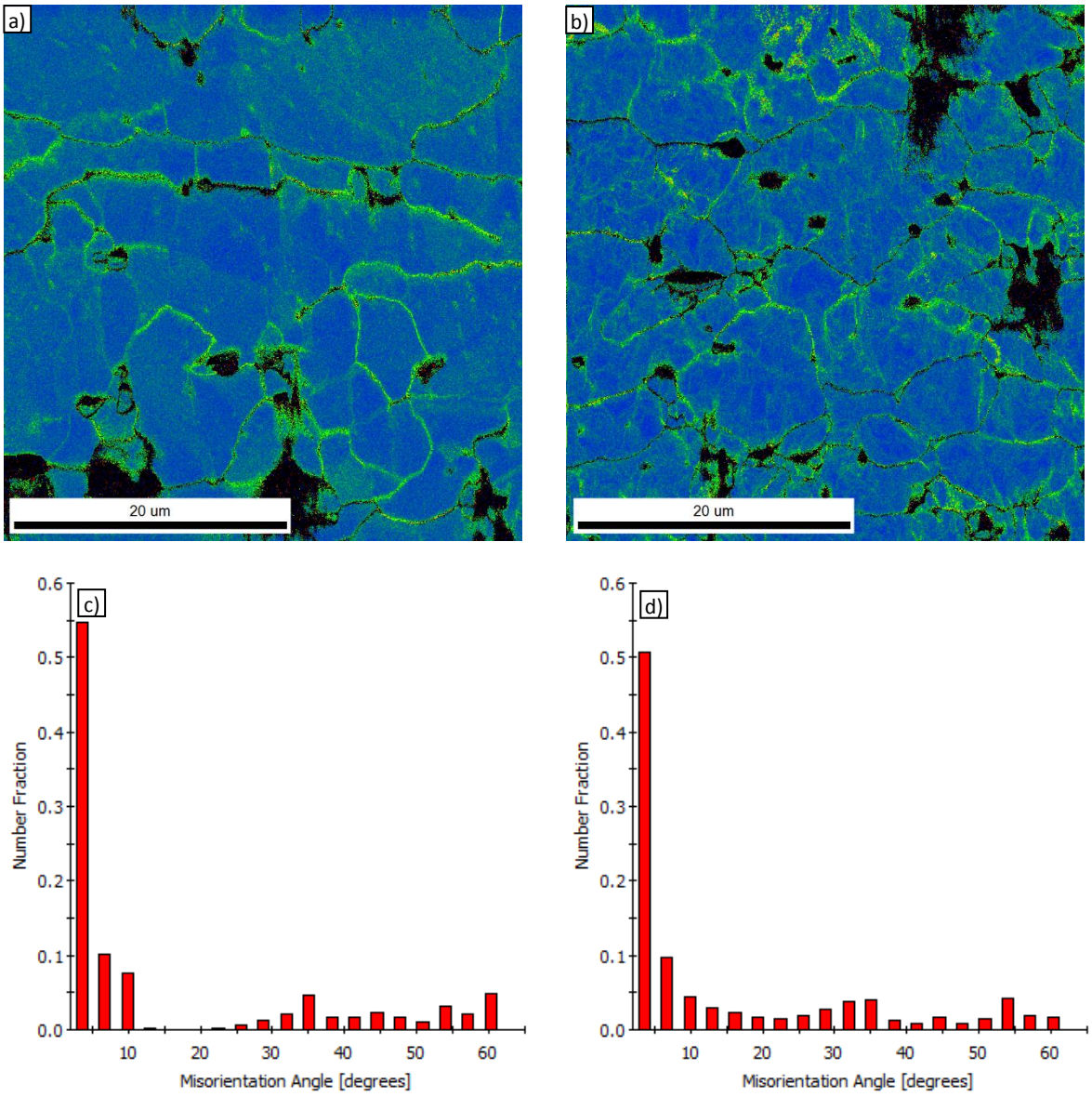

Figure 6.13. (a-b) Kernel average misorientation angle maps and (c-d) histograms of the misorientation angle from 2-65° of the crept AA3105 aluminum alloy under 85 MPa load after (a,c) 25 mins and (b,d) 2 h. (SEM performed by S.J. Schröders)

6.3.3 Discussion of creep mechanisms of the AA3105 alloy

It was mentioned that the AA3105 aluminum alloy contained precipitates and dispersions. Due to the high temperature heat treatment of the initial condition, coarsening occurred and the Mg-Si particles did not make a contribution to the strengthening after the heat treatment. However the α-Al(Fe,Mn)Si particles are the stable precipitates, which cannot grow at 140 °C. The effect of α-Al(Fe,Mn)Si particles on the creep behavior of the AA3105 aluminum alloy was investigated. The investigation shows that the three following creep regimes are active and dominant at different stress and temperature ranges.

1- Low stresses at low temperature region:

   It was found during the evaluation of the strain rate with respect to the normalized stress that the α-Al(Fe,Mn)Si particles have reduced the dislocation motion during the creep tests. The determined stress exponents were in the range of 0.5-1.0 at low stresses. The average activation energy is 15.3 kJ/mole, therefore a non-diffusional mechanism could be responsible for it. A possible non-diffusional process is cross slip. Atomistic simulations showed that cross slip mechanisms have activation energy of 57 via Fleischer mechanism [202] to 2 kJ/mole via Friedel and Escaig mechanism [203], [204] at zero temperature in aluminum [205]. Increasing the temperature and stress decrease the activation energy for cross slip. Thus the most probable creep mechanism is cross slip, which is also reported by Matsunaga et al. [119]. Thus according to [119] the most probable creep mechanism is dislocation annihilation by cross slip at cell walls. This mechanism has not been observed or mentioned for the present alloy in der literature.

2- Low stresses at high temperature region:

   It was observed that at high temperatures and low stresses the average activation energy of the creep mechanism is 89.3 kJ/mole which is close to the diffusion through the dislocation core [206]. Additionally, the stress exponent is close to 5, which indicates that dislocation motion is the dominant creep mechanism. Therefore, the most probable creep mechanism according to the Table 6.2 is pipe-diffusion-controlled dislocation climb. Figure 6.10 also shows that the dislocation density has increased at 40 MPa at 175 °C, and comparing the samples with undeformed samples (Figure 6.8) verifies that the recovery processes are active and subgrain boundaries were formed. At the beginning of the creep, the dislocation motion leads to an increase of the

dislocation density over time. The increase of the misorientation angle at subgrain boundaries verifies that the dislocation density has increased at grain boundaries and also dislocations are partially annihilated, which lead to the increasing misorientation angle at subgrains to up to 15 degree. At some areas the deformation is so high that the indexing of the EBSD patterns is impossible, and over time these unindexed areas were increased.

Table 6.2. n, p and Q values for creep in pure aluminum

Mechanisms	n	p	Q
Nabarro-Herring Creep	1	2	Q_L = 142kJ [120]
Coble creep	1	3	Q_{gb} = 85kJ [120]
Harper-Dorn creep	1	0	Q_L = 142kJ [120]
Grain boundary sliding ($d_g < subgrains$)	2	2	Q_{gb} = 85kJ [108]
Grain boundary sliding ($d_g > subgrains$)	3	1	Q_L = 142 Kj [108]
Dislocation climb	4.5	0	Q_L = 142kJ [136]
Dislocation glide	2-3	1-2	Q_L = 142kJ [132], [137]

3- High stresses at high temperature region:

At high stresses and temperatures, the stress exponent is equal to 6. This indicates that the dislocation motion is the active deformation mechanism. On the other hand, the average activation energy is 174.9 kJ/mole and is higher than the accepted activation energy for self-diffusion through lattice (Q_{sd} = 142 kJ/mole), which is same as noted in precipitation hardened alloys [207]–[209]. This suggests that the dominant creep mechanism is self-diffusion controlled dislocation climb creep with drag stress. Dislocation glide was also observed in Figure 6.13, which shows that the dislocation density has increased drastically. The unindexed areas are more than the unindexed areas in the 40 MPa sample after 14 h. Additionally, over time, the area of the unindexed points increased mainly at grain boundaries. On the other hand, the misorientation angles at grain boundaries increased, not only at subgrains, but also at high angle grain boundaries. The increase of the misorientation angles suggested the activation of the recovery processes, which leads to the rearrangement and

annihilation of the dislocation at grain boundaries, which leads to the increase of the grain boundaries misorientation angle [210]–[212].

The suggested creep mechanisms based on the creep tests for the AA3105 aluminum alloy show a good agreement with the developed features of microstructure on SEM and TEM images.

6.4 Results of Al-Zr-Fe aluminum alloy

6.4.1 Creep tests

The tensile creep tests were carried out at different temperatures ranging from 100 °C to 200 °C (373K – 473K) under different applied stresses. Figure 6.14 shows the creep curves.

Some parts of experimental details, results and conclusions of this part of the thesis are based and taken from the Bachelor thesis of Simon Arnoldi, entitled “Creep behaviour of Al-Fe-Zr alloys”, written under my supervision [213].

As it was explained in section 2.4, the dominant creep mechanism was determined using the minimum creep rates at different temperatures under different stresses. Figure 6.15 shows the minimum creep rates vs. reciprocal of the absolute temperature at different stresses for the Al-Zr-Fe aluminum alloy. According to the activation energies, three different regimes are observed: one low temperature regime and two high temperature regimes. At low temperatures the average activation energy is 25.63 kJ/mole and at high temperatures and low stresses, the average activation energy is 67.7 kJ/mole, and at high stresses is around 137.2 kJ/mole. Unlike in the case of AA3105 (Figure 6.6), a continuous transition from the low stress regime to the high stress regime is observed at high temperature.

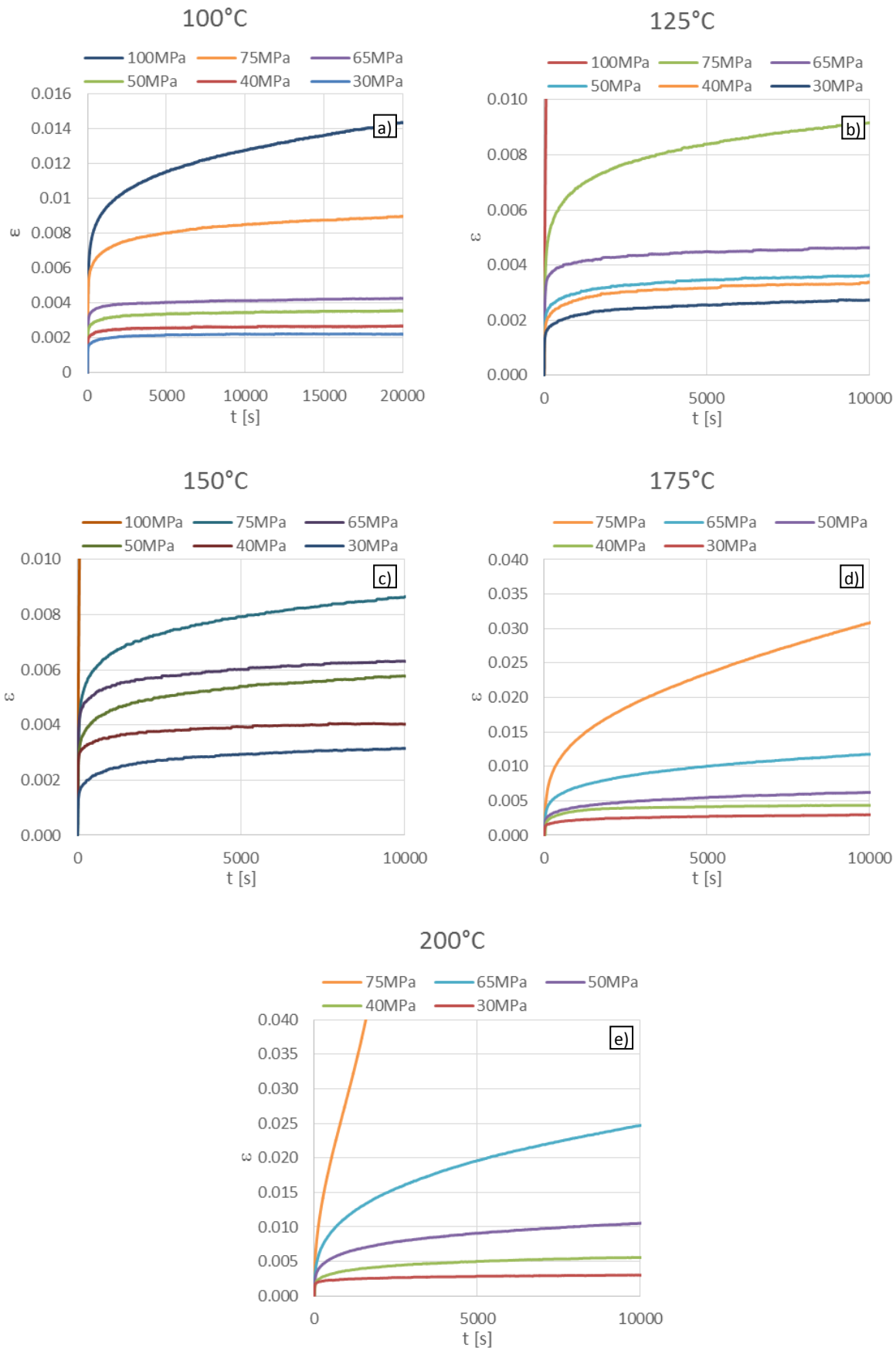

Figure 6.14. The creep strain over time for the Al-Zr-Fe aluminum at different temperatures.

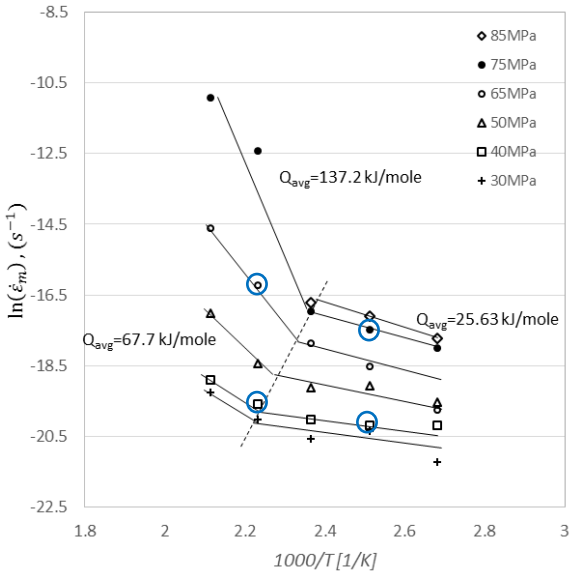

Figure 6.15. The minimum creep rates vs. reciprocal of the absolute temperature at different stresses for Al-Zr-Fe aluminum alloy.

Based on the fitted creep exponents, two distinct regimes are observed at low and high stresses (see Figure 6.16). In the lower stress regime, the stress exponent is in the range of 3-6, which indicates that the dislocations motion is the dominant deformation mechanism. At higher stresses, the stress exponent is 26, which is considered as the power-law breakdown region [186].

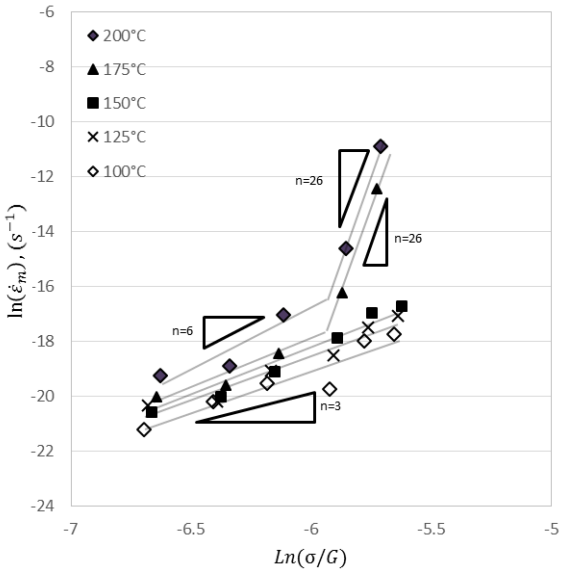

Figure 6.16. The temperature dependence of minimum creep rates at different tensile stresses, to determine Q-values for Al-Zr-Fe aluminum alloy.

6.4.2 Microstructure observation

Figure 6.17 shows the SE image of the extruded Al-Zr-Fe aluminum alloy, which is considered as the initial condition. The SEM micrographs show that there are coarse precipitates present in the matrix. EDS measurements demonstrated that the precipitates are the Al-Fe particles (see Figure 6.2.c). The Zr content stays in the matrix as solute atoms. The grains were elongated in extrusion direction. IPF images show big grains which are elongated along one direction. The mean grain diameter cannot be measured or determined, since the grains were too big and hence too few to reflect enough grains in an IPF.

Figure 6.18 shows the TEM dark-field image of the Al-Zr-Fe after creep samples under 40 MPa and 75 MPa at 125°C in the steady-state region. Comparing the images reveals that the sample under 40 MPa had a lower dislocation density. Under higher stress (75MPa) dislocation density is high, but due to a preparation artifact, they are not clearly visible.

Figure 6.19 (a,b) shows the kernel average misorientation maps (KAM) of the crept Al-Zr-Fe aluminum alloy at 125 °C under 40 MPa and 75MPa in the steady-state region. The KAM maps show that by increasing the stress the dislocation density has increased at subgrain boundaries (green lines in the figure). Additionally, Figure 6.11.c and d show that the fraction of the low angle grain boundaries with misorientation angles below 8° is higher in the sample which was tested under 40MPa. However, at higher stress, the misorientation angle increased and the fraction of low angle grain boundaries with a misorientation angle more than 8° was higher in the sample which was tested under 75 MPa. This shows that the dislocations were consumed at grain boundaries and high angle grain boundaries were formed.

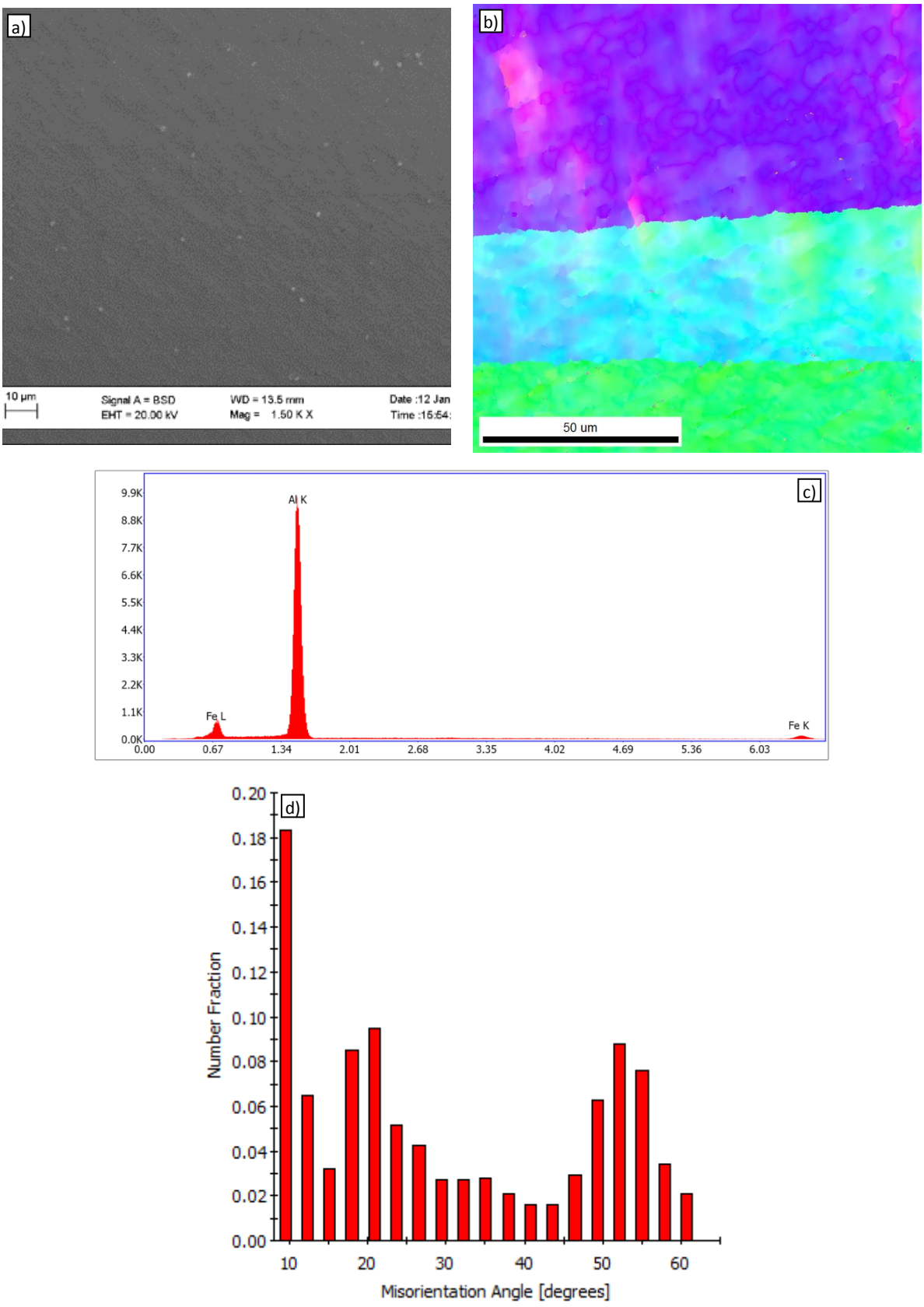

Figure 6.17. (a) SEM image, (b) EBSD map, (c) the EDS analysis and (d) histogram of the misorientation angle from 2-65° of the Al-Zr-Fe aluminum alloy in as-extruded condition.

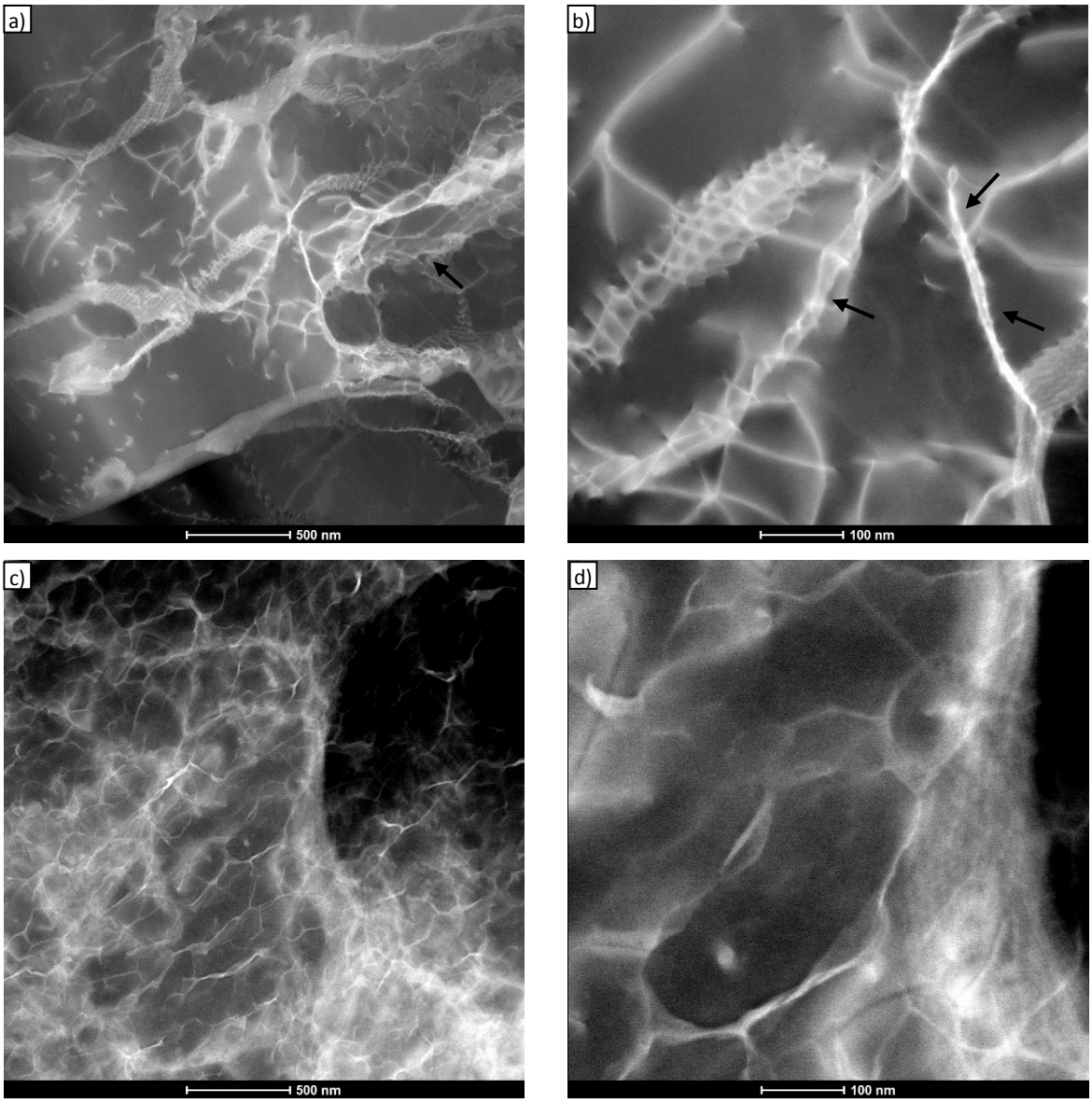

Figure 6.18. TEM dark-field micrographs of the crept Al-Zr-Fe aluminum alloy at 125 °C (a,b) under 40 MPa and (c,d) 75 MPa in the steady-state region. Arrows show subgrain boundaries and dislocation dipoles. (Image acquired by S. Zischke)

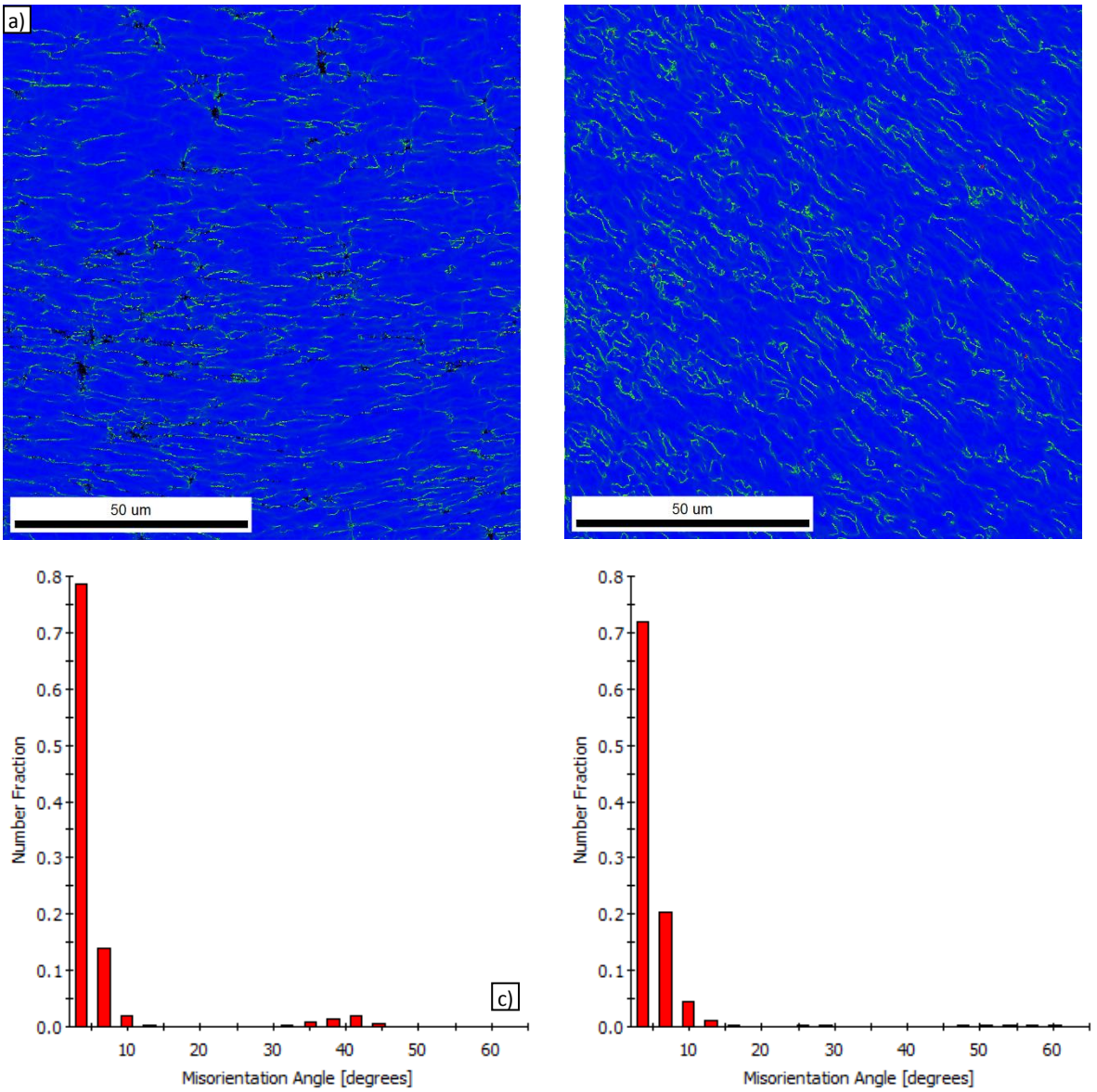

Figure 6.19. (a-b) Kernel average misorientation angle maps and (c-d) histograms of the misorientation angle from 2-65° of the crept Al-Zr-Fe aluminum alloy at 125 °C (a,c) under 40 MPa and (b,d) 75 MPa in the steady-state region. (SEM performed by S.J. Schröders)

Figure 6.20 shows the microstructure evolution of the Al-Zr-Fe aluminum alloy after creep at 175 °C under 40 MPa and 75 MPa in the steady-state region. In Figure 6.20 (a,b) no dislocations were observed. Subgrain boundaries were observed (see arrows on Figure 6.20. a and b). Additionally, the brightness of the matrix within a grain has changed, which may be attributed to the presence of the geometrically necessary dislocation. At lower temperature the contrast change was not observed [196]–[198]. Figure 6.20 (c,d) shows dislocations and low angle grain boundaries and subgrain boundaries. Dislocations were recovered and low angle grain boundaries and subgrains were formed compared to the 125 °C.

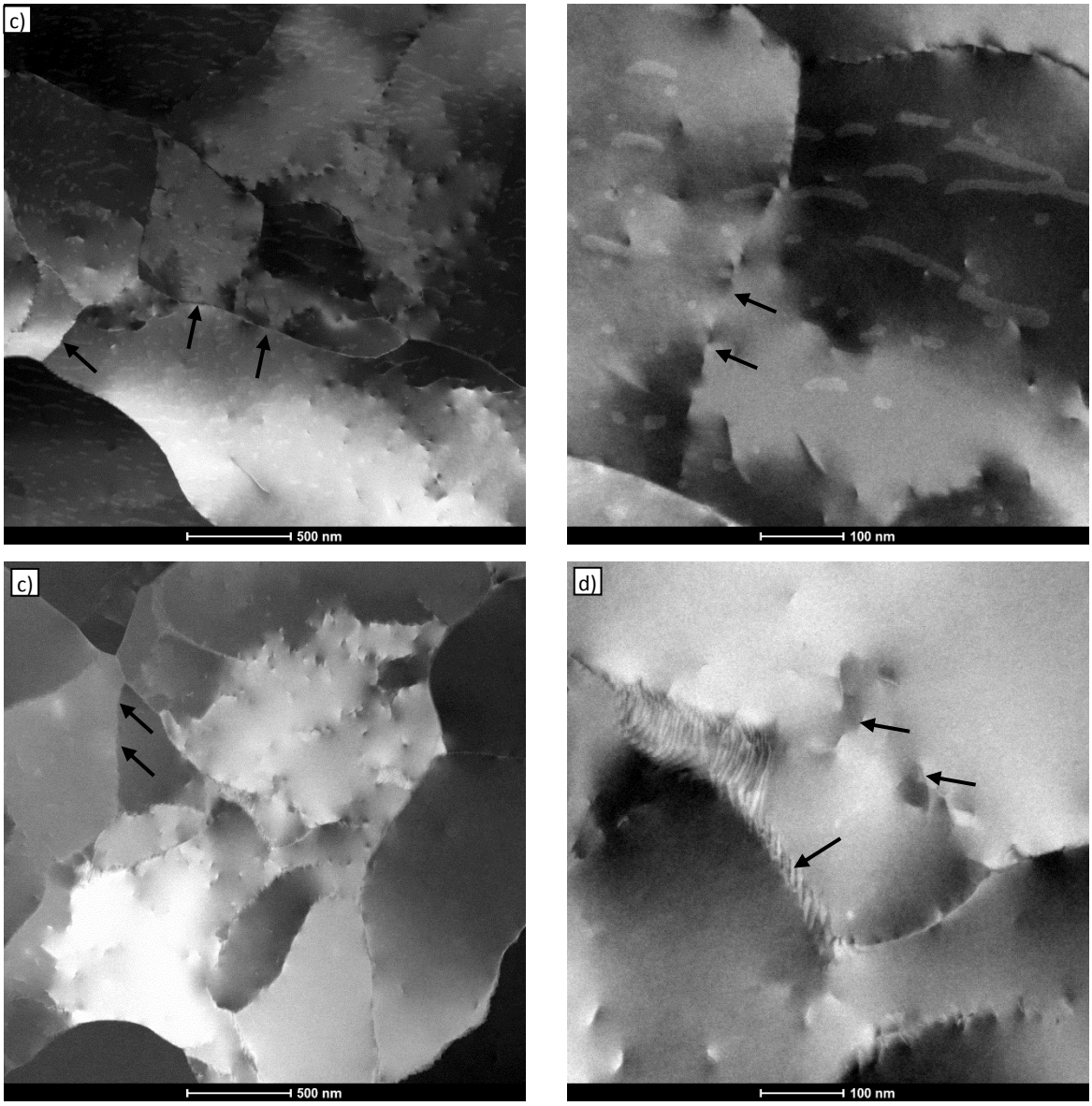

Figure 6.20. TEM dark-field micrographs of the crept Al-Zr-Fe aluminum alloy at 175 °C (a-b) under 40 MPa and (c-d) 75 MPa in the steady-state region. Arrows show subgrain boundaries, dislocations and low angle grain boundaries. (TEM performed by S. Zischke)

Figure 6.21 shows the Kernel average misorientation angle map and histogram of the misorientation angle from 2-65° of the crept Al-Zr-Fe aluminum alloy at 175 °C under 40MPa and 75 MPa tensile creep stress. The dislocation density was higher for the samples after creep at 175 °C under 75MPa. The green line shows the areas which had higher misorientation angle and consequently higher GND density. Figure 6.21.a shows that the GNDs are not dominant in the matrix and the matrix is not deformed drastically. Figure 6.21.c and d show the

distribution of the misorientation angle in the matrix. At lower stress the amount of low angle grain boundaries is much higher than at high stress.

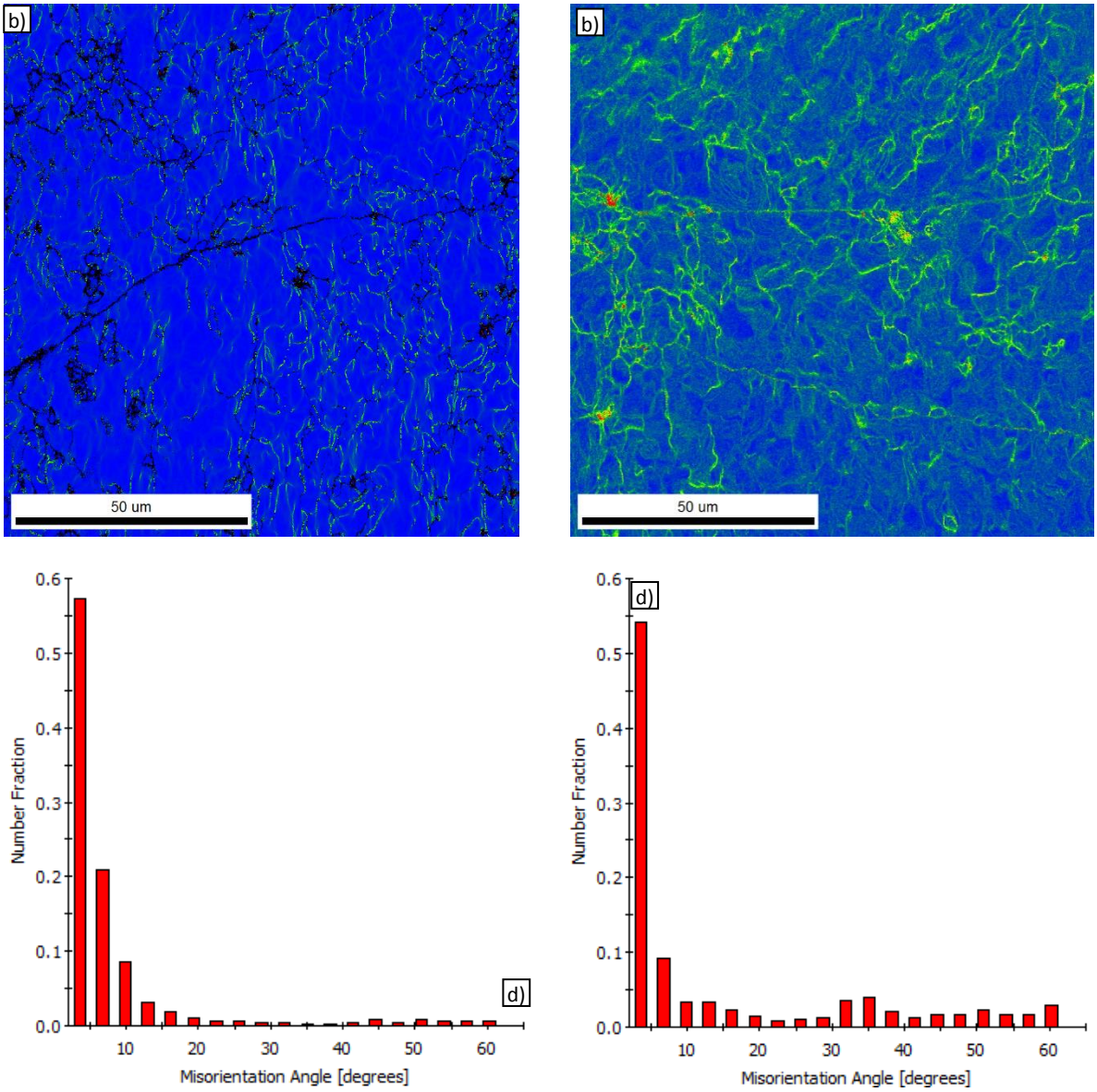

Figure 6.21. Kernel average misorientation angle maps and histograms of the misorientation angle from 2-65° of the crept Al-Zr-Fe aluminum alloy at 175 °C (a,c) under 40 MPa and (b,d) 75 MPa in the steady-state region. (SEM performed by S.J. Schröders)

6.4.3 Discussion of creep mechanisms of the Al-Zr-Fe alloy

Al-Zr-Fe did not contain Al-Zr nano-precipitates, therefore the creep behavior of the Al-Zr-Fe aluminum alloy was not influenced by nano-precipitates and dispersions. On the other hand, the matrix contained the elements Zr and Fe, which reduce the motion of the dislocations. The microstructure investigations show that the initial condition contained large grains with a

preferred orientation. Al-Fe particles were also observed in the matrix, however, the precipitation density is not high enough to contribute toward strengthening the material. The investigation shows that three different creep mechanisms are active at different stress and temperature ranges.

1- Low temperature region:

   It has been suggested that viscous dislocation glide is characterized by a stress exponent of 3 at low temperatures and 5 at high temperatures; the respective activation energies increases continuously from 25.6kJ/mole to around 68 kJ/mole. The stress exponent of the Al-Zr-Fe aluminum alloy at low temperatures and low stress is 3 and the average activation energy was found to be 25.6kJ/mole. Matsunaga et al. [119] suggested dislocation annihilation by cross slip at cell walls as a new creep mechanism at low temperature. As it was explained in section 0, activation energy of cross slip at zero temperature in aluminum via Fleischer mechanism is 57 kJ/mole and [202] via Friedel and Escaig mechanism is 2 kJ/mole [203]–[205]. Thus, the most probable creep mechanism for low temperature creep behavior of the Al-Zr-Fe aluminum alloys is cross slip at cell walls.

2- Low stress at high temperature region:

   It was observed that at high temperatures and low stresses the average activation energy of the creep mechanism is 67.7±17 kJ/mole, which is close to that of pipe diffusion. Therefore, the most probable creep mechanism is pipe-diffusion-controlled dislocation climb. Comparing the samples with undeformed samples verifies that the recovery processes have occurred and subgrain boundaries were formed (see Figure 6.17.d and Figure 6.21.c).). Increasing the misorientation angle at subgrain boundaries verifies that the dislocation density has increased at grain boundaries and also dislocations are partially annihilated, which leads to an increase of the misorientation angle at subgrains up to 15 degree.

3- High stresses at high temperature region:

   At high stresses and temperatures, the activation energy of the creep mechanism increases continuously to 137.77 kJ/mole, which is close to the accepted activation energy for self-diffusion through lattice (Q_{sd} = 142 kJ/mole), but the stress exponent is equal to 26, which is much higher than the defined stress exponents and the

mentioned mechanism are not valid any more (power-law breakdown) [186]. The transition from low stress to high stress creep mechanism occurred continuously.

The developed features of microstructure on SEM and TEM images are consistent with the suggested creep mechanisms based on the creep tests for the AA3105 aluminum alloy.

6.5 Comparison of the two alloys

In order to compare two different alloys, the relative creep rate $\dot{\varepsilon}KT/D_{pd}bG$ was plotted against σ/G on a log-log diagram (see Figure 6.22). It is observed that the Al-Zr-Fe aluminum alloy has a lower creep rate at low stresses, which is attributed to the strengthening of the alloy due to the solid solution hardening. However the lower steady-state creep rate is just valid up to 75 MPa. At higher stresses deformation occurred faster, which is attributed to the low yield stress due to the large grain diameter and low work hardening ability. The steady-state creep rate of AA3105 aluminum alloy is less than the Al-Zr-Fe aluminum alloy in the same ranges of stress (<75 MPa) and temperature (100-150°C). The AA3105 aluminum alloy shows a much better creep resistance at high stresses and temperatures, which could be due to the smaller grain size (Hall-Petch effect)[109], [110], [214] and, more importantly, precipitation hardening.

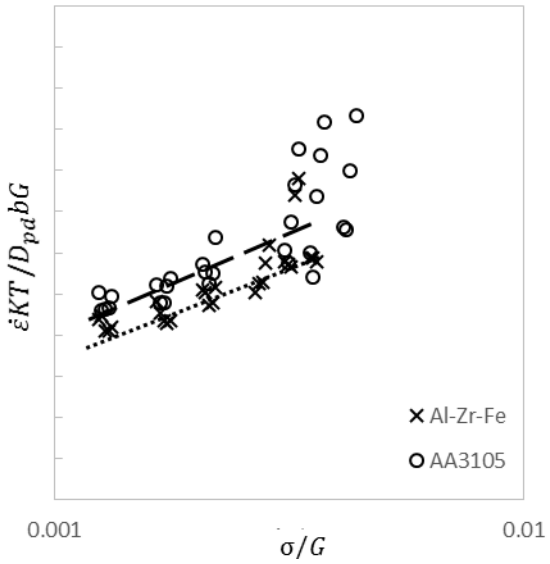

Figure 6.22. The temperature compensated strain rate vs. normalized stress for AA3105 and Al-Zr-Fe aluminum alloys.

6.6 Conclusions

In this chapter, the creep behavior of AA3105 and Al-Zr-Fe aluminum alloys were investigated. The n and Q values were determined and creep regimes were identified for each aluminum alloy.

1- The creep mechanism of the AA3105 aluminum alloy at low stresses and low temperature was determined to be dislocation annihilation by cross slip at cell walls. At low stresses and intermediate temperatures, the most probable creep mechanism is pipe-diffusion-controlled dislocation climb. Under high stresses at high temperature, creep appears to be self-diffusion controlled dislocation climb with drag stress.

2- Three creep regions were observed in the Al-Zr-Fe aluminum alloy. Under low stresses and at low temperature, the creep mechanism was concluded to be dislocation annihilation by cross slip at cell walls. Under low stresses and at high temperatures, the creep mechanism was pipe-diffusion-controlled dislocation climb. The creep mechanism under high stresses and at high temperature was not determined due to the power-law breakdown.

3- Comparison of the creep behavior of AA3105 and Al-Zr-Fe aluminum alloy shows that the Al-Zr-Fe aluminum alloy has a lower creep rate at low stresses, which is attributed to the strengthening of the alloy due to the solid solution hardening, but at stresses higher than 75 MPa, the steady-state creep rate of the AA3105 aluminum alloy is lower than Al-Zr-Fe aluminum alloy.

7 Summary

In this study, the microstructural evolution of a homogenized AA6016, AA6005 and an as-cast AA3105 aluminum alloy was simulated by means of the ClaNG model, and the precipitation sequences of an as-cast AA3105 aluminum alloy with and without Mg addition were investigated. Finally, the creep behavior of AA3105 and Al-Zr-Fe aluminum alloys was evaluated.

7.1 Essential model improvements

In order to simulate precipitation kinetics and DSC curve, the following improvements to the ClaNG model were made.

- A new database were added including metastable phases.
- A new growth law based on a mean field approach was implemented in code.
- A combination of Lagrange and Euler like approaches were used.
- A heat flux model was implemented to calculate DSC curves.
- A Strength model was implemented to derive mechanical properties immediately.
- A new model was used to simulate the incubation time of nucleation.

The improvements make the simulation of nucleation and growth of precipitates of aluminum alloys during isothermal and non-isothermal heat treatments by means of the ClaNG model possible.

7.2 Precipitation simulation and kinetics

The ClaNG model coupled with a thermodynamic database was used to simulate isothermal and non-isothermal heat treatments. The heat flux evolution during DSC of the alloy in continuous heating experiments was simulated as well. The simulations were in a good agreement with experimental data. The evolution of the metastable and stable phases was well reproduced by the computer simulations. Additionally, the results pointed out that the DSC curves are better tools to calibrate the models, and that DSC simulations are extremely useful to interpret the DSC curves. TEM investigations showed that the precipitation sequence of AA3105 from as-cast condition is GPI zones → β'' → β' → α-Al(Mn,Fe)Si → β (Mg_2Si). The precipitation sequence of the AA3105 aluminum alloy without Mg is: *small precipitates with an unknown structure* → *α-Al(Mn,Fe)Si*. The *α-Al(Mn,Fe)Si* phase is semi-coherent, its precipitation is not observed after standard heat treatments and is only detected in the as-

cast condition. It was evinced that Mg addition shifts the precipitation temperature of the α-Al(Mn,Fe)Si to lower temperatures. Based on the new understanding of the precipitation sequence and the kinetics, new heat treatments were proposed and tested in order to improve the strength and the creep resistance. The new improved heat treatment may guide industrial production, the homogenization path in particular, towards improved mechanical properties. For the commercial AA3105 aluminum alloy, the maximum hardness was achieved by the precipitation of the long-term stable α-Al(Mn,Fe)Si particles.

7.3 Creep behavior of the new aluminum alloys

Finally, the creep behavior of AA3105 and Al-Zr-Fe aluminum alloys was investigated and interpreted. Comparing the determined stress exponent and activation energies with literature, the creep regimes were identified for each aluminum alloy.

The creep mechanism of AA3105 aluminum alloy at low stresses and low temperature can be dislocation annihilation by cross slip at cell walls. Under low stresses and higher temperatures, the most probable creep mechanism is pipe-diffusion-controlled dislocation climb. Under high stresses at high temperature, the creep mechanism is probably dislocation glide with a drag stress.

Three creep mechanisms were also determined for an Al-Zr-Fe aluminum alloy. Under low stresses at low temperature, the creep mechanism can be dislocation annihilation by cross slip at the cell walls. Under low stresses at high temperature, the creep mechanism is probably pipe-diffusion-controlled dislocation climb. The creep mechanism under high stresses at high temperature could not be determined.

A comparison of the creep behavior of AA3105 and Al-Zr-Fe aluminum alloy shows that the Al-Zr-Fe aluminum alloy has a lower creep rate at low stresses, which is attributed to the strengthening of the matrix due to the solid solution hardening. But at stresses higher than 75 MPa the steady-state creep rate of the AA3105 aluminum alloy is lower than Al-Zr-Fe aluminum alloy.

Based on the achieved results, a new homogenization path is proposed for AA3105 aluminum alloy to reduce the steady-state creep rate of the AA3105 aluminum alloy. Further research into creep behavior and electrical conductivity of it is suggested to compare the results with the required norms for the power grids.

References

[1] G. Gottstein, *Physical foundations of materials science*, vol. 7, no. 7–8. Aachen Germany: Springer Verlag, 2004.

[2] R. E. Reed-Hill, *Physical Metallurgy Principles, 2nd Ed.*, Fourth. Stamford: Cengage Learning, 1973.

[3] G. K. Quainoo and S. Yannacopoulos, "The effect of prestrain on the natural aging and fracture behaviour of AA6111 aluminum," *J. Mater. Sci.*, vol. 39, no. 15, pp. 4841–4847, Aug. 2004.

[4] J. Kim, E. Kobayashi, and T. Sato, "Effects of Cu Addition on Behavior of Nanoclusters during Multi-Step Aging in Al-Mg-Si Alloys," *Mater. Trans.*, vol. 52, no. 5, pp. 906–913, 2011.

[5] J. Buha, R. N. Lumley, and A. G. Crosky, "Microstructural development and mechanical properties of interrupted aged Al-Mg-Si-Cu alloy," *Metall. Mater. Trans. A Phys. Metall. Mater. Sci.*, vol. 37, no. 10, pp. 3119–3130, 2006.

[6] L. Renhof, C. Krempaszky, E. Werner, and M. Stockinger, "Analysis of Microstructural Properties of IN 718 After High Speed Forging," *Miner. Met. Mater. Soc.*, pp. 261–270, 2005.

[7] A. Serizawa, T. Sato, and M. K. Miller, "Effect of cold rolling on the formation and distribution of nanoclusters during pre-aging in an Al-Mg-Si alloy," *Mater. Sci. Eng. A*, vol. 561, pp. 492–497, 2013.

[8] H. L. Yu, A. K. Tieu, C. Lu, X. H. Liu, A. Godbole, and C. Kong, "Mechanical properties of Al-Mg-Si alloy sheets produced using asymmetric cryorolling and ageing treatment," *Mater. Sci. Eng. A*, vol. 568, pp. 212–218, 2013.

[9] I. J. Polmear, *Light Alloys*. Oxford; Burlington, MA: Elsevier, 2005.

[10] F. Eberl, S. Gardiner, G. Campanile, G. Surdon, M. Venmans, and P. Prangnell, "Ageformable panels for commercial aircraft," *Proc. Inst. Mech. Eng. Part G J. Aerosp. Eng.*, vol. 222, no. 6, pp. 873–886, 2008.

[11] C. K. S. Moy, M. Weiss, J. Xia, G. Sha, S. P. Ringer, and G. Ranzi, "Influence of heat treatment on the microstructure, texture and formability of 2024 aluminium alloy,"

Mater. Sci. Eng. A, vol. 552, pp. 48–60, 2012.

[12] Y. Chen, N. Gao, G. Sha, S. P. Ringer, and M. J. Starink, "Microstructural evolution, strengthening and thermal stability of an ultrafine-grained Al-Cu-Mg alloy," *Acta Mater.*, vol. 109, pp. 202–212, 2016.

[13] R. K. W. Marceau, "Atomic-scale analysis of light alloys using atom probe tomography," *Mater. Sci. Technol.*, vol. 32, no. 3, pp. 209–219, 2016.

[14] G. Sha, R. K. W. Marceau, X. Gao, B. C. Muddle, and S. P. Ringer, "Nanostructure of aluminium alloy 2024: Segregation, clustering and precipitation processes," *Acta Mater.*, vol. 59, no. 4, pp. 1659–1670, 2011.

[15] C. Wagner, "Theorie der Alterung von Niederschlägen durch Umlösen (Ostwald-Reifung)," *Zeitschrift für Elektrochemie, Berichte der Bunsengesellschaft für Phys. Chemie*, vol. 65, no. 7–8, pp. 581–591, 1961.

[16] S. C. Wang and M. J. Starink, "Two types of S phase precipitates in Al-Cu-Mg alloys," *Acta Mater.*, vol. 55, no. 3, pp. 933–941, 2007.

[17] P. S. Chen, A. K. Kuruvilla, T. W. Malone, and W. P. Stanton, "The Effects of Artificial Aging on the Microstructure and Fracture Toughness of Al-Cu-Li Alloy 2195," *J. Mater. Eng. Perform.*, vol. 7, no. 5, pp. 682–690, 1998.

[18] C. Cayron, L. Sagalowicz, L. Sagalowicz, and P. A. Buffat, "Structural phase transition in Al-Cu-Mg-Si alloys by transmission electron microscopy study on an Al-4 wt% Cu-1 wt% Mg-Ag alloy reinforced by SiC particles," *Philos. Mag. A Phys. Condens. Matter, Struct. Defects Mech. Prop.*, vol. 79, no. 11, pp. 2833–2851, 1999.

[19] F. Nový, M. Janeček, and R. Král, "Microstructure changes in a 2618 aluminium alloy during ageing and creep," *J. Alloys Compd.*, vol. 487, no. 1–2, pp. 146–151, 2009.

[20] S. Y. Hu, M. I. Baskes, M. Stan, and L. Q. Chen, "Atomistic calculations of interfacial energies, nucleus shape and size of θ′ precipitates in Al-Cu alloys," *Acta Mater.*, vol. 54, no. 18, pp. 4699–4707, 2006.

[21] T. B. Massalski, *Binary Alloy Phase Diagrams*. Asm International, 1990.

[22] J. Papazian, "A calorimetric study of precipitation in aluminum alloy 2219," *Metall. Trans. A*, vol. 12A, pp. 269–279, 1981.

[23] A. Serizawa, S. Hirosawa, and T. Sato, “Three-Dimensional atom probe characterization of nanoclusters responsible for multistep aging behavior of an Al-Mg-Si alloy,” *Metall. Mater. Trans. A Phys. Metall. Mater. Sci.*, vol. 39, no. 2, pp. 243–251, 2008.

[24] C. H. Shen and B. L. Ou, “Effect of prestraining on the natural ageing and artificial ageing of an Al-Mg-Si alloy AA6022,” *Can. Metall. Q.*, vol. 46, no. 1, pp. 65–74, 2007.

[25] M. Cabibbo, E. Evangelista, and M. Vedani, “Influence of severe plastic deformations on secondary phase precipitation in a 6082 Al-Mg-Si alloy,” *Metall. Mater. Trans. A Phys. Metall. Mater. Sci.*, vol. 36, no. 5, pp. 1353–1364, 2005.

[26] E. Sjölander and S. Seifeddine, “Artificial ageing of Al-Si-Cu-Mg casting alloys,” *Mater. Sci. Eng. A*, vol. 528, no. 24, pp. 7402–7409, 2011.

[27] M. Jin, J. Li, and G. J. Shao, “Study of Cu Addition on Precipitation Behaviors and Mechanical Properties in AA6082 Al-Mg-Si Alloy,” *Mater. Sci. Forum*, vol. 546–549, pp. 825–828, 2007.

[28] W. F. Miao and D. E. Laughlin, “Effects of Cu content and preaging on precipitation characteristics in aluminum alloy 6022,” *Metall. Mater. Trans. A Phys. Metall. Mater. Sci.*, vol. 31, no. 2, pp. 361–371, 2000.

[29] A. Lutts, “Pre-precipitation in AlMgGe and AlMgSi,” *Acta Metall.*, vol. 9, no. 6, pp. 577–586, 1961.

[30] M. H. Jacobs, “The structure of the metastable precipitates formed during ageing of an Al-Mg-Si alloy,” *Philos. Mag.*, vol. 26, no. 1, pp. 1–13, 1972.

[31] R. P. Wahi and M. von Heimendahl, “On the Occurrence of the Metastable Phase β″ in an Al-Si-Mg Alloy,” *Phys. Status Solidi Appl. Res.*, vol. 24, no. 2, pp. 607–612, 1974.

[32] L. Zhen, W. D. Fei, S. B. Kang, and H. W. Kim, “Precipitation behaviour of Al-Mg-Si alloys with high silicon content,” *J. Mater. Sci.*, vol. 32, no. 7, pp. 1895–1902, 1997.

[33] L. C. Doan, Y. Ohmori, and K. Nakai, “Precipitation and dissolution reactions in a 6061 aluminum alloy,” *Materials Transactions Jim*, vol. 41, no. 2. pp. 300–305, 2000.

[34] Y. Ohmori, L. C. Doan, and K. Nakai, “Ageing Processes in Al-Mg-Si Alloys during Continuous Heating,” *Mater. Trans.*, vol. 43, no. 2, pp. 246–255, 2002.

[35] A. K. Gupta, D. J. Lloyd, and S. A. Court, “Precipitation hardening in Al-Mg-Si alloys

with and without excess Si," *Mater. Sci. Eng. A*, vol. 316, no. 1–2, pp. 11–17, 2001.

[36] A. Gaber, M. A. Gaffar, M. S. Mostafa, and A. F. Abo Zeid, "Investigation of developed precipitates in Al–1·1 wt-%Mg_2Si balanced alloy by DSC and SEM techniques," *Mater. Sci. Technol.*, vol. 22, no. 12, pp. 1483–1488, 2006.

[37] D. Zhao *et al.*, "Structure and thermodynamics of the key precipitated phases in the Al-Mg-Si alloys from first-principles calculations," *J. Mater. Sci.*, vol. 46, no. 24, pp. 7839–7849, 2011.

[38] D. J. Lloyd, D. R. Evans, and A. K. Gupta, "Precipitation reactions and the Differential Scanning Calorimetry response of AA6111 alloy," *Can. Metall. Q.*, vol. 39, no. 4, pp. 475–482, 2000.

[39] W. F. Miao and D. E. Laughlin, "Precipitation hardening in aluminum alloy 6022," *Scr. Mater.*, vol. 40, no. 7, pp. 873–878, 1999.

[40] R. S. Yassar, M. Cai, D. P. Field, X. Chen, and J. Asay, "The effect of shock-loading on the aging behavior of an Al-Mg-Si alloy," *J. Mater. Sci.*, vol. 41, no. 6, pp. 1711–1720, 2006.

[41] N. C. W. Kuijpers, W. H. Kool, and S. van der Zwaag, "DSC Study on Mg-Si Phases in As Cast AA6xxx," *Mater. Sci. Forum*, vol. 396–402, pp. 675–680, 2002.

[42] R. Vissers, M. A. van Huis, J. Jansen, H. W. Zandbergen, C. D. Marioara, and S. J. Andersen, "The crystal structure of the β′ phase in Al-Mg-Si alloys," *Acta Mater.*, vol. 55, no. 11, pp. 3815–3823, 2007.

[43] L. K. Berg, D. Schryvers, and L. R. Wallenberg, "GP-Zones in Al – Zn – Mg alloys and their role in Artificial aging," *Acta Mater.*, vol. 4, pp. 3443–3451, 2001.

[44] D. Godard, P. Archambault, E. Aeby-Gautier, and G. Lapasset, "Precipitation sequences during quenching of the AA 7010 alloy," *Acta Mater.*, vol. 50, no. 9, pp. 2319–2329, 2002.

[45] K. Stiller, P. J. Warren, V. Hansen, J. Angenete, and J. Gjønnes, "Investigation of precipitation in an Al-Zn-Mg alloy after two-step ageing treatment at 100° and 150°C," *Mater. Sci. Eng. A*, vol. 270, no. 1, pp. 55–63, 1999.

[46] H. Löffler, I. Kovacs, and J. Lendvai, "Review: Decomposition processes in AI-Zn-Mg alloys," *J. Mater. Sci.*, vol. 18, pp. 2215–2240, 1983.

[47] J. Lendvai, "Precipitation and Strengthening in Aluminium Alloys," *Mater. Sci. Forum*, vol. 217–222, pp. 43–56, 1996.

[48] T. T. Sasaki, T. Ohkubo, and K. Hono, "Microstructure and mechanical properties of bulk nanocrystalline Al-Fe alloy processed by mechanical alloying and spark plasma sintering," *Acta Mater.*, vol. 57, no. 12, pp. 3529–3538, 2009.

[49] J. Courbon, "Mechanical Metallurgy of Aluminium Alloys for the Beverage Can," *Mater. Sci. Forum*, vol. 331–337, pp. 17–30, 2000.

[50] D. T. L. Alexander, R. Hamerton, H. Cama, and a. L. Greer, "Study of Intermetallic Phase Transformations in 3xxx Alloys Using Diffusion Couples," *Mater. Sci. Forum*, vol. 396–402, pp. 681–686, 2002.

[51] K. Liu, H. Ma, and X. G. Chen, "Enhanced elevated-temperature properties via Mo addition in Al-Mn-Mg 3004 alloy," *J. Alloys Compd.*, vol. 694, no. October, pp. 354–365, 2017.

[52] K. LIU, A. M. NABAWY, and X. G. CHEN, "Influence of TiB2 nanoparticles on elevated-temperature properties of Al-Mn-Mg 3004 alloy," *Trans. Nonferrous Met. Soc. China (English Ed.*, vol. 27, no. 4, pp. 771–778, 2017.

[53] Y. J. Li, A. M. F. Muggerud, A. Olsen, and T. Furu, "Precipitation of partially coherent α-Al(Mn,Fe)Si dispersoids and their strengthening effect in AA 3003 alloy," *Acta Mater.*, vol. 60, no. 3, pp. 1004–1014, 2012.

[54] A. M. F. Muggerud, E. A. Mørtsell, Y. Li, and R. Holmestad, "Dispersoid strengthening in AA3xxx alloys with varying Mn and Si content during annealing at low temperatures," *Mater. Sci. Eng. A*, vol. 567, pp. 21–28, 2013.

[55] A. M. F. Muggerud, Y. J. Li, and R. Holmestad, "Orientation Studies of α-Al(Fe,Mn)Si Dispersoids in 3xxx Al Alloys," *Mater. Sci. Forum*, vol. 794–796, pp. 39–44, 2014.

[56] T. Ziar, H. Farh, and R. Guemini, "The microstructure development during isothermal heat treatment study of an Al-Mg-Si aluminium alloy," *Acta Metall. Slovaca*, vol. 22, no. 3, pp. 138–144, 2016.

[57] J. A. Österreicher, M. Kumar, A. Schiffl, S. Schwarz, and G. R. Bourret, "Secondary precipitation during homogenization of Al-Mg-Si alloys: Influence on high temperature flow stress," *Mater. Sci. Eng. A*, vol. 687, no. January, pp. 175–180, 2017.

[58] W. B. Hutchinson, A. Oscarsson, and Å. Karlsson, "Control of microstructure and earing behaviour in aluminium alloy AA 3004 hot bands," *Mater. Sci. Technol.*, vol. 5, no. 11, pp. 1118–1127, 1989.

[59] M. Dehmas, P. Weisbecker, G. Geandier, P. Archambault, and E. Aeby-Gautier, "Experimental study of phase transformations in 3003 aluminium alloys during heating by in situ high energy X-ray synchrotron radiation," *J. Alloys Compd.*, vol. 400, no. 1–2, pp. 116–124, 2005.

[60] A. L. DONS, "ALFESI-Particles in industrially cast-aluminum alloys," *Zeitschrift Fur Met.*, vol. 76, no. 9, pp. 609–612, 1985.

[61] M. Jin, C. F. Xia, and G. J. Shao, "The Study on Precipitation Characteristics in 6082 Aluminum Alloy with Cu Addition," *Adv. Mater. Res.*, vol. 299–300, pp. 122–126, 2011.

[62] X. Wang, S. Esmaeili, and D. J. Lloyd, "The sequence of precipitation in the Al-Mg-Si-Cu alloy AA6111," *Metall. Mater. Trans. A Phys. Metall. Mater. Sci.*, vol. 37, no. 9, pp. 2691–2699, 2006.

[63] G. A. Edwards, K. Stiller, G. L. Dunlop, and M. J. Couper, "The precipitation sequence in Al-Mg-Si alloys," *Acta Mater.*, vol. 46, no. 11, pp. 3893–3904, 1998.

[64] D. A. C. G.G. Liversidge, K.C. Cundy, J.F. Bishop, "United States Patent (19) 54," vol. 96, no. 19, pp. 62–66, 1980.

[65] N. Nakamura and R. Kinoshita, "Differential scanning calorimeter," 21-Jan-2003.

[66] Y. Min *et al.*, "Differential scanning calorimeter," 03-Dec-2002.

[67] S. Pogatscher, H. Antrekowitsch, and P. J. Uggowitzer, "Influence of starting temperature on differential scanning calorimetry measurements of an Al-Mg-Si alloy," *Mater. Lett.*, vol. 100, no. November 2015, pp. 163–165, 2013.

[68] E. Watson, "Differential microcalorimeter," 1962.

[69] M. Vončina, "Determination of precipitation sequence in Al-alloys using DSC method," *Mater. Geoenvironment*, vol. 57, no. 3, pp. 295–304, 2010.

[70] J. Osten, B. Milkereit, C. Schick, and O. Kessler, "Dissolution and precipitation behaviour during continuous heating of Al-Mg-Si alloys in a wide range of heating rates," *Materials (Basel).*, vol. 8, no. 5, pp. 2830–2848, 2015.

[71] E. Kozeschnik, *Modelling Solid-State Precipitation*. Momentum Press (Verlag), 2013.

[72] R. Becker and W. Döring, "Kinetische Behandlung der Keimbildung in übersättigten Dämpfen," *Ann. Phys.*, vol. 416, no. 8, pp. 719–752, 1935.

[73] O. Penrose, "The Becker-Döring equations at large times and their connection with the LSW theory of coarsening," *J. Stat. Phys.*, vol. 89, no. 1–2, pp. 305–320, 1997.

[74] I. M. Lifshitz and V. V. Slyozov, "The kinetics of precipitation from supersaturated solid solutions," *J. Phys. Chem. Solids*, vol. 19, no. 1–2, pp. 35–50, Apr. 1961.

[75] Z. Liu, V. Mohles, O. Engler, and G. Gottstein, "Thermodynamics based modelling of the precipitation kinetics in commercial aluminium alloys," *Comput. Mater. Sci.*, vol. 81, pp. 410–417, 2014.

[76] C. Zener, "Theory of growth of spherical precipitates from solid solution," *J. Appl. Phys.*, vol. 20, no. 10, pp. 950–953, 1949.

[77] M. Perez, "Gibbs-Thomson effects in phase transformations," *Scr. Mater.*, vol. 52, no. 8, pp. 709–712, 2005.

[78] D. A. Porter, K. E. Easterling, and M. Sherif, *Phase Transformations in Metals and Alloys, (Revised Reprint)*. CRC press, 2009.

[79] J. Svoboda, F. D. Fischer, P. Fratzl, and E. Kozeschnik, "Modelling of kinetics in multi-component multi-phase systems with spherical precipitates I: Theory," *Mater. Sci. Eng. A*, vol. 385, no. 1–2, pp. 166–174, 2004.

[80] E. Kozeschnik, J. Svoboda, P. Fratzl, and F. D. Fischer, "Modelling of kinetics in multi-component multi-phase systems with spherical precipitates II: Numerical solution and application," *Mater. Sci. Eng. A*, vol. 385, no. 1–2, pp. 157–165, Nov. 2004.

[81] J. S. Langer and A. J. Schwartz, "Kinetics of nucleation in near-critical fluids," *Phys. Rev. A*, vol. 21, no. 3, pp. 948–958, 1980.

[82] R. Kampmann and R. Wagner, "Kinetics of Precipitation in Metastable Binary Alloys: Theory and Application to Copper--1. 9 at.% Titanium and Nickel--14 at.% Aluminium(Alloys)," in *Decomposition of Alloys: the Early Stages*, 1984, pp. 91–103.

[83] R. W. Cahn, P. Haasen, and E. J. Kramer, "Materials Science and Technology: A Comprehensive Treatment," *Phase Transform. Mater.*, vol. 5, pp. 213–303, 2000.

[84] M. Perez, M. Dumont, and D. Acevedo-Reyes, "Implementation of classical nucleation and growth theories for precipitation," *Acta Mater.*, vol. 56, no. 9, pp. 2119–2132, 2008.

[85] O. R. Myhr and O. Grong, "Modelling of non-isothermal transformations in alloys containing a particle distribution," *Acta Mater.*, vol. 48, no. 7, pp. 1605–1615, 2000.

[86] P. Maugis and M. Gouné, "Kinetics of vanadium carbonitride precipitation in steel: A computer model," *Acta Mater.*, vol. 53, no. 12, pp. 3359–3367, 2005.

[87] O. R. Myhr, O. Grong, H. G. Fjær, and C. D. Marioara, "Modelling of the microstructure and strength evolution in al-mg-si alloys during multistage thermal processing," *Acta Mater.*, vol. 52, no. 17, pp. 4997–5008, 2004.

[88] O. R. Myhr, O. Grong, and S. J. Andersen, "Modelling of the age hardening behaviour of Al-Mg-Si alloys," *Acta Mater.*, vol. 49, no. 1, pp. 65–75, 2001.

[89] I. N. Khan and M. J. Starink, "Microstructure and strength modelling of Al–Cu–Mg alloys during non-isothermal treatments: Part 1 – Controlled heating and cooling," *Mater. Sci. Technol.*, vol. 24, no. 12, pp. 1403–1410, 2008.

[90] I. N. Khan, M. J. Starink, and J. L. Yan, "A model for precipitation kinetics and strengthening in Al-Cu-Mg alloys," *Mater. Sci. Eng. A*, vol. 472, no. 1–2, pp. 66–74, 2008.

[91] A. Falahati, E. Povoden-Karadeniz, P. Lang, P. Warczok, and E. Kozeschnik, "Thermo-kinetic computer simulation of differential scanning calorimetry curves of AlMgSi alloys," *Int. J. Mater. Res.*, vol. 101, no. 9, pp. 1089–1096, 2010.

[92] A. Falahati, J. Wu, P. Lang, M. R. Ahmadi, E. Povoden-Karadeniz, and E. Kozeschnik, "Assessment of parameters for precipitation simulation of heat treatable aluminum alloys using differential scanning calorimetry," *Trans. Nonferrous Met. Soc. China (English Ed.*, vol. 24, no. 7, pp. 2157–2167, 2014.

[93] E. Povoden-Karadeniz, P. Lang, P. Warczok, A. Falahati, W. Jun, and E. Kozeschnik, "CALPHAD modeling of metastable phases in the Al-Mg-Si system," *Calphad Comput. Coupling Phase Diagrams Thermochem.*, vol. 43, pp. 94–104, 2013.

[94] M. J. Starink and S. Wang, "Comments on 'Modelling differential scanning calorimetry curves of precipitation in Al-Cu-Mg,'" *Scr. Mater.*, vol. 62, no. 9, pp. 720–723, 2010.

[95] M. J. Starink and S. Wang, "Comments on 'Modelling differential scanning calorimetry

curves of precipitation in Al-Cu-Mg,’” *Scr. Mater.*, vol. 62, no. 9, pp. 720–723, 2010.

[96] S. Spigarelli, “Creep of Aluminium and Aluminium Alloys,” *Talat*, p. 26, 1999.

[97] M. E. Kassner, “Harper-Dorn Creep,” *Fundam. Creep Met. Alloy. Third Ed.*, vol. 23, pp. 109–128, 2015.

[98] J. Pelleg, “Creep in ceramics,” *Solid Mech. its Appl.*, vol. 241, no. i, pp. 41–61, 2017.

[99] W. Rosenhain and D. Ewen, “The intercrystalline cohesion of metals*(SECOND PAPER).,” *J. Inst. Met.*, vol. 10, p. 149, 1913.

[100] W. Rosenhain and J. C. W. Humfrey, “The Tenacity, Deformation and Fracture of Soft Steel at High Temperatures,” *Iron Steel Inst*, vol. 87, p. 219, 1913.

[101] R. L. Bell and T. G. Langdon, “An investigation of grain-boundary sliding during creep,” *J. Mater. Sci.*, vol. 2, no. 4, pp. 313–323, 1967.

[102] H. F. Moore, B. B. Betty, and C. W. Dollins, “Creep and fracture of lead and lead alloys: a report,” University of Illinois at Urbana Champaign, College of Engineering. Engineering Experiment Station., 1935.

[103] H. F. Moore, B. B. Betty, and C. W. Dollins, “Investigation of creep and fracture of lead and lead alloys for cable sheathing: a report,” University of Illinois at Urbana Champaign, College of Engineering. Engineering Experiment Station., 1938.

[104] R. King, R. W. Cahn, and B. Chalmers, “Mechanical Behaviour of Crystal Boundaries in Metals,” *Nature*, vol. 161, p. 682, May 1948.

[105] F. Weinberg, “Grain boundary shear in aluminum,” *Acta Metall.*, vol. 2, no. 6, pp. 889–890, 1954.

[106] F. Weinberg, “Grain boundary shear in aluminum,” *Trans. Am. Inst. Min. Metall. Eng.*, vol. 212, pp. 808–817, 1958.

[107] W. A. Rachinger, “Relative grain translations in the plastic flow of aluminium,” *J. Inst. Met.*, vol. 81, 1952.

[108] T. G. Langdon, “Grain boundary sliding revisited: Developments in sliding over four decades,” *J. Mater. Sci.*, vol. 41, no. 3, pp. 597–609, 2006.

[109] E. O. Hall, “the Deformation and Ageing of Mild Steel .2. Characteristics of the Luders Deformation,” *Proc. Phys. Soc. London Sect. B*, vol. 64, no. 381, pp. 742-, 1951.

[110] N. J. PETCH, “The Cleavage Strength of Polycrystals,” *J. Iron Steel Inst.*, vol. 174, pp. 25–28, 1953.

[111] A. Ball and M. M. Hutchison, “Superplasticity in the aluminium–zinc eutectoid,” *Met. Sci. J.*, vol. 3, no. 1, pp. 1–7, 1969.

[112] F. A. Mohamed and T. G. Langdon, “Creep behaviour in the superplastic Pb–62% Sn eutectic,” *Philos. Mag.*, vol. 32, no. 4, pp. 697–709, 1975.

[113] F. A. Mohamed and T. G. Langdon, “Creep at low stress levels in the superplastic Zn-22% Al eutectoid,” *Acta Metall.*, vol. 23, no. 1, pp. 117–124, 1975.

[114] T. G. Langdon, “A unified approach to grain boundary sliding in creep and superplasticity,” *Acta Metall. Mater.*, vol. 42, no. 7, pp. 2437–2443, 1994.

[115] C. Herring, “Diffusional viscosity of a polycrystalline solid,” *J. Appl. Phys.*, vol. 21, no. 5, pp. 437–445, 1950.

[116] R. L. Coble, “A Model for Boundary Diffusion Controlled Creep in Polycrystalline Materials,” *J. Appl. Phys.*, vol. 34, no. 6, pp. 1679–1682, 1963.

[117] J. Harper and J. E. Dorn, “Viscous creep of aluminum near its melting temperature,” *Acta Metall.*, vol. 5, no. 11, pp. 654–665, Nov. 1957.

[118] P. Yavari, D. A. Miller, and T. G. Langdon, “An investigation of harper-dorn creep-I. Mechanical and microstructural characteristics,” *Acta Metall.*, vol. 30, no. 4, pp. 871–879, Apr. 1982.

[119] T. Matsunaga and E. Sato, “Creep mechanism in several grades of aluminum at low temperatures,” *J. Japan Inst. Light Met.*, vol. 64, no. 2, pp. 42–48, 2014.

[120] S. Spigarelli, “Creep of Aluminium and Aluminium Alloys,” *Talat*, 1999.

[121] K. E. Knipling, D. C. Dunand, and D. N. Seidman, “Criteria for developing castable, creep-resistant aluminum-based alloys - A review,” *Int. J. Mater. Res.*, vol. 97, no. 3, pp. 246–265, 2006.

[122] E. Arzt, “Creep of Dispersion Strengthened Materials : A Critical Assessment,” *Res Mechanica*, vol. 31. pp. 399–453, 1991.

[123] E. Arzt and J. R??sler, “The kinetics of dislocation climb over hard particles-II. Effects of an attractive particle-dislocation interaction,” *Acta Metall.*, vol. 36, no. 4, pp. 1053–

1060, 1988.

[124] K. E. Knipling, “Development of a Nanoscale Precipitation-Strengthened Creep-Resistant Aluminum Alloy Containing Trialuminide Precipitates,” Northwestern University, 2006.

[125] E. A. Marquis and D. C. Dunand, “Model for creep threshold stress in precipitation-strengthened alloys with coherent particles,” *Scr. Mater.*, vol. 47, no. 8, pp. 503–508, 2002.

[126] M. E. Kassner, *Creep Behavior of Particle-Strengthened Alloys*. Elsevier, 2015.

[127] H. Burt, J. P. Dennison, and B. Wilshire, “Friction stress measurements during creep of Nimonic 105,” *Met. Sci.*, vol. 13, no. 5, pp. 295–300, 1979.

[128] J. D. Parker and B. Wilshire, “The effect of a dispersion of cobalt particles on high-temperature creep of copper,” *Met. Sci.*, vol. 9, no. 1, pp. 248–252, 1975.

[129] K. R. Williams and B. Wilshire, “On the stress-and temperature-dependence of creep of Nimonic 80A,” *Met. Sci. J.*, vol. 7, no. 1, pp. 176–179, 1973.

[130] H. Oikawa and T. G. Langdon, “The creep characteristics of pure metals and metallic solid solution alloys,” *Pineridge Press Ltd., Creep Behav. Cryst. Solids*, pp. 33–82, 1985.

[131] J. Cadek, “Creep in metallic materials,” 1988.

[132] T. G. Langdon, “Identifiying creep mechanisms at low stresses,” *Mater. Sci. Eng. A*, vol. 283, no. 1–2, pp. 266–273, 2000.

[133] S. P. Deshmukh, R. S. Mishra, and K. L. Kendig, “Creep behavior and threshold stress of an extruded Al-6Mg-2Sc-1Zr alloy,” *Mater. Sci. Eng. A*, vol. 381, no. 1–2, pp. 381–385, 2004.

[134] Y. Li, “An investigation of creep and substructure formation in 2124 Al,” *Acta Mater.*, vol. 45, no. 6, pp. 2607–2620, 1997.

[135] F. A. Mohamed and T. G. Langdon, “The transition from dislocation climb to viscous glide in creep of solid solution alloys,” *Acta Metall.*, vol. 22, no. 6, pp. 779–788, 1974.

[136] J. Weertman, “Steady-state creep through dislocation climb,” *J. Appl. Phys.*, vol. 28, no. 10, pp. 362–364, 1957.

[137] J. Weertman, “Steady-state creep of crystals,” *J. Appl. Phys.*, vol. 28, no. 10, pp. 1185–

1189, 1957.

[138] P. M. Kelly, “Progress Report on Recent Advances in Physical Metallurgy: (C) The Quantitative Relationship between Microstructure and Properties in Two-Phase Alloys,” *Int. Metall. Rev.*, vol. 18, no. 1, pp. 31–36, Mar. 1973.

[139] O. D. Sherby, R. H. Klundt, and A. K. Miller, “Flow stress, subgrain size, and subgrain stability at elevated temperature,” *Metall. Trans. A*, vol. 8, no. 6, pp. 843–850, 1977.

[140] A. Simar, Y. Bréchet, B. de Meester, A. Denquin, and T. Pardoen, “Sequential modeling of local precipitation, strength and strain hardening in friction stir welds of an aluminum alloy 6005A-T6,” *Acta Mater.*, vol. 55, no. 18, pp. 6133–6143, 2007.

[141] A. Deschamps and Y. Brechet, “Influence of predeformation and ageing of an Al-Zn-Mg Alloy-II. Modeling of precipitation kinetics and yield stress,” *Acta Mater.*, vol. 47, no. 1, pp. 293–305, 1998.

[142] D. Carron, P. Bastid, Y. Yin, and R. G. Faulkner, “Modelling of precipitation during friction stir welding of an Al-Mg-Si alloy,” *Tech. Mech.*, vol. 30, no. 1–3, pp. 29–44, 2010.

[143] M. Nicolas and A. Deschamps, “Characterisation and modelling of precipitate evolution in an Al-Zn-Mg alloy during non-isothermal heat treatments,” *Acta Mater.*, vol. 51, no. 20, pp. 6077–6094, 2003.

[144] F. Delmas, M. J. Casanove, P. Lours, A. Couret, and A. Coujou, “Quantitative TEM study of the precipitation microstructure in aluminium alloy Al(MgSiCu) 6056 T6,” *Mater. Sci. Eng. A*, vol. 373, no. 1–2, pp. 80–89, 2004.

[145] M. Schneider, G. Gottstein, L. Löchte, and J. Hirsch, “A statistical model for precipitation - applications to commercial Al-Mn-Mg-Fe-Si alloys,” *Mater. Sci. Forum*, vol. 396–402, pp. 637–642, 2002.

[146] B. Sonderegger and E. Kozeschnik, “Generalized nearest-neighbor broken-bond analysis of randomly oriented coherent interfaces in multicomponent Fcc and Bcc structures,” *Metall. Mater. Trans. A Phys. Metall. Mater. Sci.*, vol. 40, no. 3, pp. 499–510, 2009.

[147] G. Eriksson and K. Hack, “ChemApp - A Programmable Thermodynamic Calculation Interface,” in *Werkstoffwoche 96 Symposium 8: Simulation, Modellierung, Informationssysteme*, 1997, p. 47.

[148] S. Petersen and K. Hack, “The thermochemistry library ChemApp and its applications,” *Int. J. Mater. Res.*, vol. 98, no. 10, pp. 935–945, Oct. 2007.

[149] H. Wakeshima, “Time lag in the self-nucleation,” *J. Chem. Phys.*, vol. 22, no. 9, pp. 1614–1615, 1954.

[150] J. D. Robson, “Optimizing the homogenization of zirconium containing commercial aluminium alloys using a novel process model,” *Mater. Sci. Eng. A*, vol. 338, no. 1–2, pp. 219–229, 2002.

[151] Y. Du *et al.*, “Diffusion coefficients of some solutes in fcc and liquid Al: Critical evaluation and correlation,” *Mater. Sci. Eng. A*, vol. 363, no. 1–2, pp. 140–151, 2003.

[152] C. W. Bale *et al.*, “FactSage thermochemical software and databases - recent developments,” *Calphad Comput. Coupling Phase Diagrams Thermochem.*, vol. 33, no. 2, pp. 295–311, Jun. 2009.

[153] L. Zhen, W. D. Fei, S. B. Kang, and H. W. Kim, “Precipitation behaviour of Al-Mg-Si alloys with high silicon content,” *J. Mater. Sci.*, vol. 32, no. 7, pp. 1895–1902, Apr. 1997.

[154] H.-W. Huang, B.-L. Ou, and C.-T. Tsai, “Effect of Homogenization on Recrystallization and Precipitation Behavior of 3003 Aluminum Alloy,” *Mater. Trans.*, vol. 49, no. 2, pp. 250–259, 2008.

[155] E. Nes, “the Effect of a Fine Particle Dispersion on Heterogeneous,” *Acta Metall.*, vol. 24, no. 5, pp. 391–398, 1975.

[156] B. K. Nagahama, “Precipitation during Recrystallization Alloys * in Al-Mn and Al-Cr,” *Trans. Japan Inst. Met.*, vol. 15, no. 3, pp. 185–192, 1974.

[157] H. Hirasawa, “Precipitation process of AlMn and AlCr supersaturated solid solution in presence of age hardening phases,” *Scr. Metall.*, vol. 9, no. 9, pp. 955–958, 1975.

[158] K. Liu and X. G. Chen, “Evolution of Intermetallics, Dispersoids, and Elevated Temperature Properties at Various Fe Contents in Al-Mn-Mg 3004 Alloys,” *Metall. Mater. Trans. B Process Metall. Mater. Process. Sci.*, vol. 47, no. 6, pp. 3291–3300, 2016.

[159] Z. LI, Z. ZHANG, and X. G. CHEN, “Effect of magnesium on dispersoid strengthening of Al—Mn—Mg—Si (3xxx) alloys,” *Trans. Nonferrous Met. Soc. China (English Ed.)*, vol. 26, no. 11, pp. 2793–2799, 2016.

[160] M. S. Remøe, K. Marthinsen, I. Westermann, K. Pedersen, J. Røyset, and C. Marioara, "The effect of alloying elements on the ductility of Al-Mg-Si alloys," *Mater. Sci. Eng. A*, vol. 693, no. January, pp. 60–72, 2017.

[161] S. J. Andersen, H. W. Zandbergen, J. Jansen, C. Træholt, U. Tundal, and O. Reiso, "The crystal structure of the β″ phase in Al-Mg-Si Alloys," *Acta Mater.*, vol. 46, no. 9, pp. 3283–3298, 1998.

[162] Z. W. Du *et al.*, "Microstructural evolution after creep in aluminum alloy 2618," *J. Mater. Sci.*, vol. 47, no. 6, pp. 2541–2547, 2012.

[163] R. N. Corby and P. J. Black, "The structure of [alpha]-(AlFeSi) by anomalous-dispersion methods," *Acta Crystallogr. Sect. B*, vol. 33, no. 11, pp. 3468–3475, 1977.

[164] L. Lodgaard and N. Ryum, "Precipitation of dispersoids containing Mn and/or Cr in Al–Mg–Si alloys," *Mater. Sci. Eng. A283*, vol. 283, pp. 144–152, 2000.

[165] Y. Birol, "Homogenization of en AW 6005A Alloy for Improved Extrudability," *Metall. Mater. Trans. A Phys. Metall. Mater. Sci.*, vol. 44, no. 1, pp. 504–511, 2013.

[166] J. Du, B. Wen, R. Melnik, and Y. Kawazoe, "Cluster characteristics and physical properties of binary Al-Zr intermetallic compounds from first principles studies," *Comput. Mater. Sci.*, vol. 103, pp. 170–178, 2015.

[167] A. Hayoune and N. Titouche, "A DSC Investigation of the Effects of Cold Deformation and Low Temperatures Aging on the Microstructural Stability of a Peak Aged (PA) Al 6061 Alloy," *Appl. Mech. Mater.*, vol. 432, pp. 32–38, 2013.

[168] M. Moustafa, F. Samuel, and H. Doty, "Effect of solution heat treatment and additives on the hardness , tensile properties and fracture behaviour of Al-Si (A413 . 1) automotive alloys," *J. Mater. Sci.*, vol. 8, pp. 4523–4534, 2003.

[169] R. Rettig and R. F. Singer, "Numerical modelling of precipitation of topologically close-packed phases in nickel-base superalloys," *Acta Mater.*, vol. 59, no. 1, pp. 317–327, 2011.

[170] R. Dif *et al.*, "Understanding and Modelling the Mechanical and Corrosion Properties of 6056 for Aerospace Applications," *Mater. Sci. Forum*, vol. 331–337, pp. 1613–1618, 2000.

[171] J. Kongthep and P. Juijerm, "Kinetics of precipitation hardening phase in aluminium

alloy AA 6110," *Mater. Sci. Technol.*, vol. 30, no. 14, pp. 1815–1819, 2014.

[172] S. K. Chaudhury and D. Apelian, "Fluidized bed heat treatment of cast Al-Si-Cu-Mg alloys," *Metall. Mater. Trans. A Phys. Metall. Mater. Sci.*, vol. 37, no. 7, pp. 2295–2311, 2006.

[173] E. Çadırlı, H. Tecer, M. Şahin, E. Yılmaz, T. Kırındı, and M. Gündüz, "Effect of heat treatments on the microhardness and tensile strength of Al–0.25 wt.% Zr alloy," *J. Alloys Compd.*, vol. 632, no. 0, pp. 229–237, 2015.

[174] E. Scheil, "Bemerkungen zur schichtkristallbildung," *Zeitschrift für Met.*, vol. 34, no. 3, pp. 70–72, 1942.

[175] N. Saunders, "Light Metals 1997," *TMS, Warrendale, PA*, vol. 101, 1997.

[176] S. Chen, W. Oldfield, Y. A. Chang, and M. K. Thomas, "Modeling Solidification of Turbine Blades Using Theoretical Phase Relationships," vol. 25, no. July, pp. 1525–1533, 1994.

[177] H. Seyedrezai, D. Grebennikov, P. Mascher, and H. S. Zurob, "Study of the early stages of clustering in Al–Mg–Si alloys using the electrical resistivity measurements," *Mater. Sci. Eng. A*, vol. 525, no. 1–2, pp. 186–191, 2009.

[178] Y. Birol, "The effect of sample preparation on the DSC analysis of 6061 alloy," *J. Mater. Sci.*, vol. 40, no. 24, pp. 6357–6361, 2005.

[179] S. Esmaeili, X. Wang, D. J. Lloyd, and W. J. Poole, "On the precipitation-hardening behavior of the Al-Mg-Si-Cu alloy AA6111," *Metall. Mater. Trans. A Phys. Metall. Mater. Sci.*, vol. 34, no. 13, pp. 751–763, 2003.

[180] "OIM Data Collection software (OIMDC)." Draper, UT, USA.

[181] B. Fultz and J. M. Howe, *Transmission electron microscopy and diffractometry of materials*, Fourth. London: Springer, 2008.

[182] K. Li *et al.*, "Atomistic structure of Cu-containing β″ precipitates in an Al-Mg-Si-Cu alloy," *Scripta Materialia*, vol. 75. pp. 86–89, 2014.

[183] E. Abe, Y. Kawamura, K. Hayashi, and A. Inoue, "Long-period ordered structure in a high-strength nanocrystalline Mg-1 at% Zn-2 at% Y alloy studied by atomic-resolution Z-contrast STEM," *Acta Mater.*, vol. 50, no. 15, pp. 3845–3857, 2002.

[184] J. I. Rojas and D. Crespo, “Modeling of the effect of temperature, frequency, and phase transformations on the viscoelastic properties of AA 7075-T6 and AA 2024-T3 aluminum alloys,” *Metall. Mater. Trans. A*, vol. 43, no. 12, pp. 4633–4646, 2012.

[185] C. I. M. Percival, “Elevated . temperature Elastic Moduli of 2024 Aluminum Obtained by a Laser . pulse Technique,” pp. 245–250.

[186] F. A. Mohamed and T. G. Langdon, “Deformation mechanism maps based on grain size,” *Metall. Trans.*, vol. 5, no. 11, pp. 2339–2345, 1974.

[187] R. A. Karnesky, D. N. Seidman, and D. C. Dunand, “Creep of Al-Sc Microalloys with Rare-Earth Element Additions,” *Mater. Sci. Forum*, vol. 519–521, pp. 1035–1040, 2006.

[188] Y. Li, “An investigation of creep and substructure formation in 2124 Al,” *Acta Mater.*, vol. 45, no. 6, pp. 2607–2620, 1997.

[189] R. S. Mishra, T. K. Nandy, and G. W. Greenwood, “The threshold stress for creep controlled by dislocation-particle interaction,” *Philos. Mag. A Phys. Condens. Matter, Struct. Defects Mech. Prop.*, vol. 69, no. 6, pp. 1097–1109, 1994.

[190] E. Orowan, “Dislocations in metals (ed. M. Cohen). New York: Am,” *Inst. Min. Met. Engs*, 1954.

[191] U. F. Kocks, “A statistical theory of flow stress and work-hardening,” *Philos. Mag.*, vol. 13, no. 123, pp. 541–566, 1966.

[192] E. Arzt and M. F. Ashby, “Threshold stresses in materials containing dispersed particles,” 1982.

[193] R. S. W. Shewfelt and L. M. Brown, “High-temperature strength of dispersion-hardened single crystals II. Theory,” *Philos. Mag.*, vol. 35, no. 4, pp. 945–962, 1977.

[194] E. Arzt and D. S. Wilkinson, “Threshold stresses for dislocation climb over hard particles: the effect of an attractive interaction,” *Acta Metall.*, vol. 34, no. 10, pp. 1893–1898, 1986.

[195] E. Arzt and J. Rösler, “The kinetics of dislocation climb over hard particles-II. Effects of an attractive particle-dislocation interaction,” *Acta Metall.*, vol. 36, no. 4, pp. 1053–1060, Apr. 1988.

[196] A. J. Schwartz, M. Kumar, B. L. Adams, and D. P. Field, *Electron Backscatter*

Diffraction in Materials Science, 2nd ed. Springer, 2000.

[197] C. J. Gardner, B. L. Adams, J. Basinger, and D. T. Fullwood, "EBSD-based continuum dislocation microscopy," *Int. J. Plast.*, vol. 26, no. 8, pp. 1234–1247, Aug. 2010.

[198] M. Calcagnotto, D. Ponge, E. Demir, and D. Raabe, "Orientation gradients and geometrically necessary dislocations in ultrafine grained dual-phase steels studied by 2D and 3D EBSD," *Mater. Sci. Eng. A*, vol. 527, no. 10–11, pp. 2738–2746, Apr. 2010.

[199] M. M. Nowell and S. I. Wright, "Orientation effects on indexing of electron backscatter diffraction patterns," *Ultramicroscopy*, vol. 103, no. 1, pp. 41–58, 2005.

[200] D. P. Field, "Recent advances in the application of orientation imaging," *Ultramicroscopy*, vol. 67, no. 1–4, pp. 1–9, 1997.

[201] S. I. Wright, M. M. Nowell, and D. P. Field, "A review of strain analysis using electron backscatter diffraction," *Microsc. Microanal.*, vol. 17, no. 3, pp. 316–329, 2011.

[202] R. L. Fleischer, "Cross slip of extended dislocations," *Acta Metall.*, vol. 7, no. 2, pp. 134–135, 1959.

[203] J. Friedel, *Dislocations: International Series of Monographs on Solid State Physics*. Oxford, 1971.

[204] B. Escaig, "Dislocation Dynamics, Eds. AR Rosenfield, GT Hahn, AL Bement, Jr., and R. I. Jaffee," *McGraw-Hill, New York*, vol. 655, p. 161, 1968.

[205] C. Jin, Y. Xiang, and G. Lu, "Dislocation cross-slip mechanisms in aluminum," *Philos. Mag.*, vol. 91, no. 32, pp. 4109–4125, 2011.

[206] H. J. Frost and M. F. Ashby, *Deformation mechanism maps: the plasticity and creep of metals and ceramics*. Pergamon press, 1982.

[207] P. K. Chaudhury and F. a. Mohamed, "Creep and ductility in an Al-Cu solid-solution alloy," *Metall. Trans. A*, vol. 18, no. 12, pp. 2105–2114, 1987.

[208] M. S. Soliman and F. A. Mohamed, "Creep transitions in an Al-Zn alloy," *Metall. Trans. A*, vol. 15, no. 10, pp. 1893–1904, 1984.

[209] M. Keyvani, R. Mahmudi, and G. Nayyeri, "Microstructure and impression creep characteristics of cast Mg-5Sn-xBi magnesium alloys," *Metall. Mater. Trans. A Phys. Metall. Mater. Sci.*, vol. 42, no. 7, pp. 1990–2003, 2011.

[210] S. Gourdet and F. Montheillet, “An experimental study of the recrystallization mechanism during hot deformation of aluminium,” *Mater. Sci. Eng. A*, vol. 283, no. 1–2, pp. 274–288, 2000.

[211] S. Gourdet, E. V Konopleva, H. J. McQueen, and F. Montheillet, “Recrystallization during hot deformation of aluminium,” in *Materials Science Forum*, 1996, vol. 217, pp. 441–446.

[212] P. Cizek and B. P. Wynne, “A mechanism of ferrite softening in a d-uplex stainless steel deformed in hot torsion,” *Strain*, vol. 230, no. 1–2, pp. 88–94, 1997.

[213] S. Arnoldi, “Creep behaviour of Al-Fe-Zr alloys,” RWTH-Aachen, 2017.

[214] N. Hansen, “Hall-petch relation and boundary strengthening,” *Scr. Mater.*, vol. 51, no. 8 SPEC. ISS., pp. 801–806, 2004.

Abstract

Due to their high electrical conductivity and relatively high melting temperature compared to other highly conductive metals (1.72×10^{-8} Ω.m), copper alloys have been used widely in power grids. However, in the recent decades, the price of copper alloys has increased substantially. For this reason, the demand for new alloys which can be used instead of copper has increased. The working temperature of the power grids is 140 °C, with short periods of up to 200 °C. Therefore, new developed materials should possess equal or better mechanical properties (creep resistance) at these temperatures, as well as high electrical conductivity, and also a reasonable price compared to copper alloys. For these reasons, aluminum alloys are among the most promising candidates.

In this study, new aluminum alloys have been developed and investigated. Aluminum alloys have a high electrical conductivity, which satisfies this requirement for the power grids. However due to their low melting temperature, creep mechanisms are active in the temperature range of the working condition of power grids. In order to use aluminum alloys in power grids, it is necessary to develop alloys with high strength and creep resistance. Based on the mentioned demands, new aluminum alloys were produced and investigated in this work. The strain hardening mechanism is known to deteriorate the electrical conductivity. Therefore, AA3105 aluminum alloy as a precipitation hardened alloy and Al-Zr-Fe aluminum alloy as a solid solution hardened alloy were produced and investigated.

In order to optimize the mechanical properties of AA3105 aluminum alloys, the precipitation sequence of the alloys were investigated by means of DSC measurements, Transmission Electron Microscopy (TEM) and Scanning Electron Microscopy (SEM) investigations, simulations and creep tests. The precipitation behavior of as-cast AA6016, AA6005 and A3105 aluminum alloys was simulated by means of a classical nucleation and growth model. The model was coupled with a thermodynamic database containing the elements Al, Mg, Si, Fe, Cu and Mn with their corresponding stable and metastable phases. The focus of the investigation was laid on the evolution of β″, β′, β (Mg_2Si) and Si phases. DSC tests were conducted in the temperature range of 100-500 °C. The simulation results were compared to results of the DSC experiments. The simulation results showed a very good agreement with the experimentally measured DSC curves and the average particle size. TEM investigations were conducted on the DSC samples in order to identify the precipitated phases at certain

temperatures and the precipitation sequence was determined for AA3105 aluminum alloy. The evolution of the *α-Al(Mn,Fe)Si* phase was studied with and without the presence of Mg-Si phases. The *α-Al(Mn,Fe)Si* particles can improve the mechanical properties at elevated temperatures, unlike the Mg-Si phases. It was found that Mg addition accelerates the precipitation of the *α-Al(Mn,Fe)Si* particles, and it shifts the precipitation to lower temperatures during DSC measurement. This effect appears to be caused by local enrichment of the matrix, rather than direct phase transformation, since heterogeneous nucleation of *α-Al(Mn,Fe)Si* particles on the u-phase was not observed during the investigations. With high probability, the precipitation sequence of the AA3105 aluminum alloy with Mg was: (*GP zones)* → *β''* → *β'* → *α-Al(Mn,Fe)Si* → *β (Mg₂Si)*. Without Mg, the sequence was described as: *small spherical precipitates with an unknown structure* → *α-Al(Mn,Fe)Si*. Based on the simulations, new heat treatments were proposed and investigated. From their results, a new production process was proposed.

The creep behavior of the as-cast Al-Zr-Fe and AA3105 aluminum alloys was also investigated. The creep mechanism of AA3105 and Al-Zr-Fe aluminum alloys at low stresses and temperatures is dislocation annihilation by cross slip at cell walls. At low stresses and intermediate temperatures, the pipe-diffusion-controlled dislocation climb dominates. For AA3105 aluminum alloys, dislocation glide with a drag stress is dominant at high temperatures and high stresses. However, for Al-Zr-Fe, a power-law break down occurs at high temperatures and high stresses. Comparing the creep behavior of the AA3105 and Al-Zr-Fe aluminum alloys shows that the Al-Zr-Fe aluminum alloy has a better creep resistance at low stresses up to 65 MPa, due to the solid solution hardening, but at high stresses the AA3105 aluminum alloy shows a better creep resistance, which is due to the smaller grain diameter and precipitation hardening.

Based on the conducted study and understanding of the precipitation kinetics of AA3105 aluminum alloy, and also the creep behavior of both alloys, a new production chain is proposed for AA3105 aluminum alloy which is expected to lead to a higher creep resistance compared to the conventionally produced AA3105 aluminum alloy, and which is expected to fulfil the requirements of power grids.

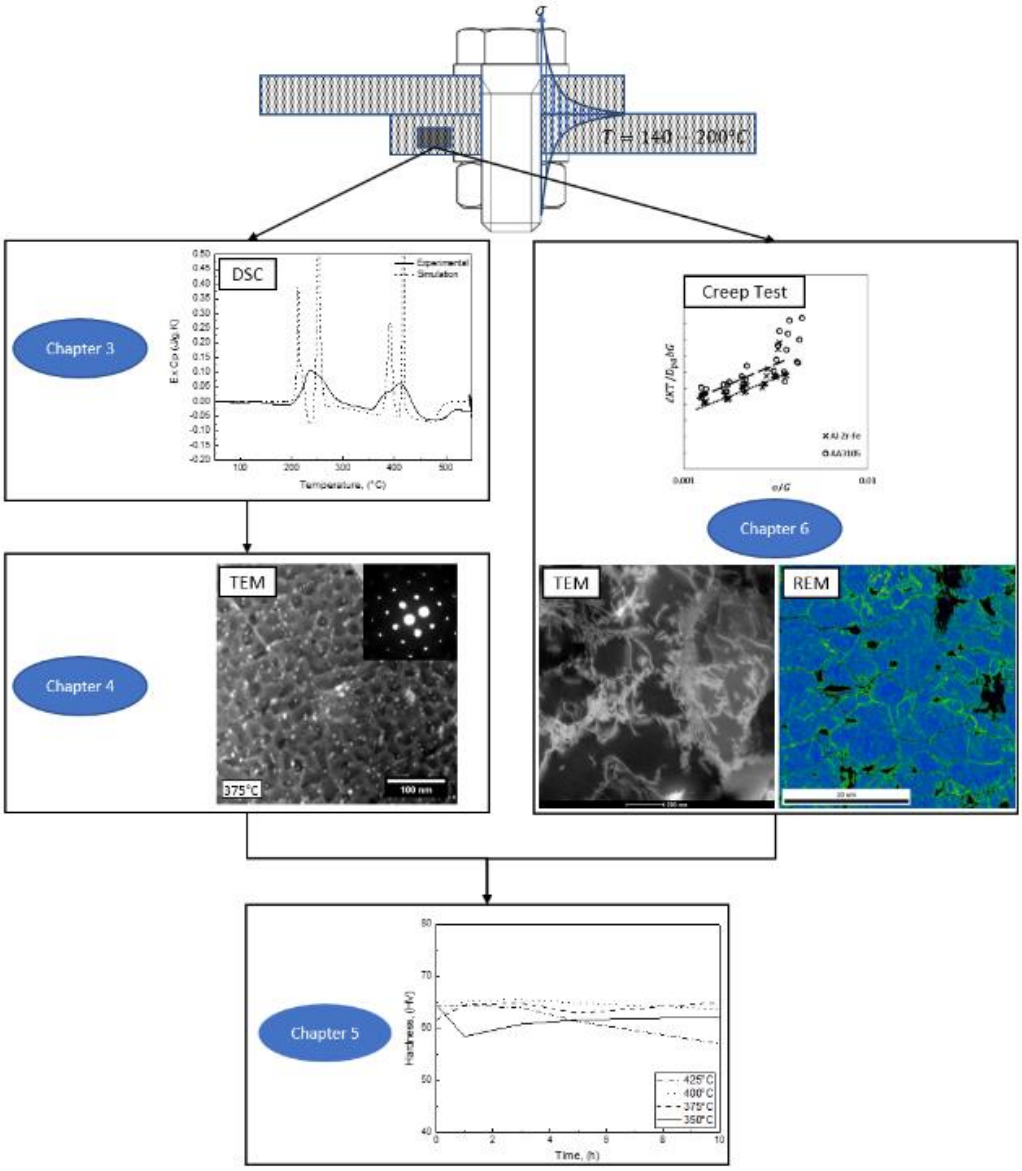
σ
T = (140 - 200°C)
DSC
Experimental
Simulation
Temperature, (°C)
Chapter 3
Creep Test
Chapter 6
Chapter 4
TEM
375°C
100 nm
TEM
REM
Chapter 5
Hardness, (HV)
Time, (h)
425°C
400°C
375°C
350°C

Kurzzusammenfassung

Aufgrund der hohen elektrischen Leitfähigkeit und einer relativ hohen Schmelztemperatur im Vergleich zu anderen hoch elektrisch leitenden Metallen werden Kupferlegierungen in großem Umfang in Stromnetzen eingesetzt. In den letzten Jahrzehnten hat sich der Preis der Kupfer-Legierungen erhöht. Deshalb hat sich die Nachfrage nach neuen Legierungen, die anstelle der Kupferlegierungen verwendet werden kann, erhöht. Die Arbeitstemperatur der Stromnetze liegt bei 140 °C, kurzzeitig auch bis zu 200 °C. Daher müssen neu entwickelte Materialien bei vernünftigem Preis vergleichbar gute mechanische Eigenschaften bei hohen Temperaturen (Kriechfestigkeit) sowie eine vergleichbar hohe elektrische Leitfähigkeit wie kommerzielle Kupferlegierungen besitzen. Aluminium-Legierungen gehören hierbei zu den erfolgversprechenden Kandidaten.

In dieser Studie wurden neue Aluminiumlegierungen entwickelt und untersucht. Aluminium-legierungen haben eine hohe elektrische Leitfähigkeit, die die Anforderungen für Stromnetze erfüllt. Jedoch sind in Aluminium aufgrund der niedrigen Schmelztemperatur relativ zur Einsatztemperatur der Stromnetze Kriechmechanismen aktiv. Um Aluminiumlegierungen in Stromnetzen zu verwenden, ist es notwendig, Legierungen mit einer hohen Kriechfästigkeit zu entwickeln. Auf der Grundlage dieser Anforderungen wurden neue Aluminiumlegierungen hergestellt und im Rahmen dieser Arbeit untersucht. Als vielversprechendste Legierungen sind AA3105 Aluminiumlegierung, eine neue ausscheidungsgehärtete Legierung sowie Al-Zr-Fe Aluminiumlegierung ausgewählt, die eine mischkristallsgehärtete Legierung ist. Um die mechanischen Eigenschaften von AA3105 Aluminiumlegierung zu optimieren, wurde die Ausscheidungssequenz der Legierungen mittels Differenzial-Scanning-Kalorimetrie (DSC), Transmissionselektronenmikroskopie (TEM) und Rasterelektronenmikroskopie (SEM) sowie Computersimulationen und Kriechversuchen untersucht. Das Ausscheidungsverhalten aus dem Gusszustand von AA6016, AA6005 und AA3105 Aluminiumlegierungen wurde mittels einem klassischen Keimbildungs- und Wachstumsmodell simuliert. Das Modell wurde mit einer thermodynamischen Datenbank, die die Elemente Al, Mg, Si, Fe, Cu und Mn mit ihren entsprechenden stabilen und metastabilen Phasen enthält, verknüpft. Der Schwerpunkt der Untersuchungen lag auf der Entwicklung von β“, β‘, β (Mg_2Si) und Si-Phasen. DSC-Tests wurden im Temperaturbereich von 100-500 °C durchgeführt. Die Simulationsergebnisse wurden mit den Ergebnissen der DSC-Experimente verglichen. Die Simulationsergebnisse

zeigten eine sehr gute Übereinstimmung mit den experimentell gemessenen DSC-Kurven und der mittleren Partikelgröße.

TEM-Untersuchungen wurden an den DSC-Proben durchgeführt, um die bei bestimmten Temperaturen ausgeschiedenen Phasen zu bestimmen und die Reihenfolge der Ausscheidung zu identifizieren. Die Entwicklung der α-Al (Mn, Fe) Si-Phase wurde mit und ohne Mg-Gehalt untersucht. Im Gegensatz zu den Mg-Si-Phasen können die α-Al(Mn,Fe)Si Partikel die mechanischen Eigenschaften bei erhöhten Temperaturen verbessern. Es wurde festgestellt, dass Mg die Ausscheidung der α-Al(Mn,Fe)Si Partikel beschleunigt, und es verschiebt die Ausscheidungstemperaturen während der DSC-Messungen zu niedrigen Temperaturen. Dieser Effekt scheint durch lokale Anreicherung der Matrix verursacht zu werden. Mit hoher Wahrscheinlichkeit lautet die Reihenfolge der Ausscheidung für AA3105 Aluminiumlegierung mit Mg: GP-Zonen → β″ → β′→ α-Al(Mn,Fe)Si → β (Mg_2Si). Ohne Mg lautet die Sequenz: kleine kugelförmige Teilchen einer noch unbekannten Struktur → α-Al(Mn,Fe)Si. Auf der Grundlage dieser Ergebnisse wurde ein neues Herstellungsverfahren für AA3105 Aluminiumlegierung vorgeschlagen und untersucht.

Das Kriechverhalten von stranggepresstem Al-Zr-Fe und AA3105 Aluminiumlegierungen wurde untersucht. Deren Kriechmechanismus bei niedrigeren Temperaturen und Spannungen ist die Versetzungsauslöschung durch Quergleiten an Zellwänden, bei hohen Temperaturen und niedrigen Spannungen das durch Diffusion im Kern kontrollierte Versetzungsklettern. Bei hohen Spannungen und Temperaturen liegt in AA3105 Versetzungsgleiten mit einer Reibungskraft vor, aber für Al-Zr-Fe führt die Erhöhung der Spannungen zum Ausfall des Potenzgesetzes. Der Vergleichen des Kriechverhaltens der AA3105 und Al-Zr-Fe-Legierungen zeigt, daß die Al-Zr-Fe infolge der Mischkristallhärtung eine bessere Kriechfestigkeit bei geringen Spannungen von bis zu 65 MPa hat, aber bei hohen Spannungen zeigt AA3105 Aluminiumlegierung eine bessere Kriechbeständigkeit, die auf die kleinere Korngröße und vor das Ausscheidungshärten zurückzuführen ist.

Für die AA3105 Aluminiumlegierung wurde, basierend auf der durchgeführten Studie und dem verbesserten Verständnis der Ausscheidungskinetik, ein Vorschlag zur Verbesserung der Prozesskette erarbeitet. Es wird erwartet, dass die neue vorgeschlagene Produktionskette im Vergleich zu der konventionellen Produktionskette für AA3105 Aluminiumlegierung zu einer höheren Kriechfestigkeit führen und die Anforderung der Stromnetze erfüllen wird.